



ISSN 1028-8546

Volume XXV, Number 3

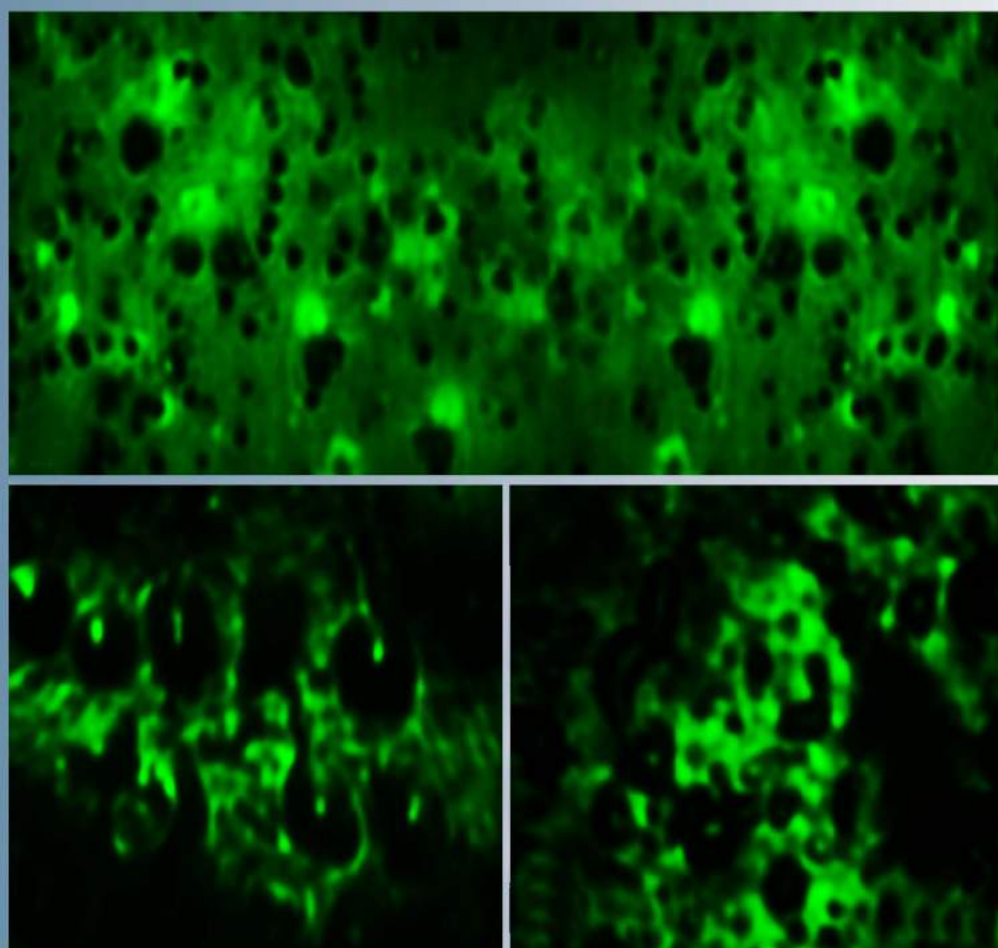
Section: En

October, 2019

# Azerbaijan Journal of Physics

# Fizika

[www.physics.gov.az](http://www.physics.gov.az)



G.M. Abdullayev Institute of Physics  
Azerbaijan National Academy of Sciences  
Department of Physical, Mathematical and Technical Sciences

## *Azerbaijan Journal of Physics*

# *FIZIKA*

*G.M. Abdullayev Institute of Physics  
Azerbaijan National Academy of Sciences  
Department of Physical, Mathematical and Technical Sciences*

### **HONORARY EDITORS**

Arif PASHAYEV

### **EDITORS-IN-CHIEF**

Nazim MAMEDOV

Chingiz QAJAR

### **SENIOR EDITOR**

Talat MEHDIYEV

### **INTERNATIONAL REVIEW BOARD**

Ivan Scherbakov, Russia  
Kerim Allahverdiyev, Azerbaijan  
Mehmet Öndr Yetiş, Turkey  
Gennadii Jablonskii, Belarus  
Rafael Imamov, Russia  
Vladimir Man'ko, Russia  
Eldar Salayev, Azerbaijan  
Dieter Hochheimer, USA  
Victor L'vov, Israel

Vyacheslav Tuzlukov, South Korea  
Majid Ebrahim-Zadeh, Spain  
Anatoly Boreysho, Russia  
Mikhail Khalin, Russia  
Hasan Bidadi, Tebriz, Iran  
Natiq Atakishiyev, Mexico  
Tayar Djafarov, Azerbaijan  
Arif Hashimov, Azerbaijan  
Javad Abidinov, Azerbaijan

Bagadur Tagiyev, Azerbaijan  
Salima Mehdiyeva, Azerbaijan  
Talat Mehdiyev, Azerbaijan  
Ayaz Bayramov, Azerbaijan  
Tofiq Mammadov, Azerbaijan  
Shakir Nagiyev, Azerbaijan  
Rauf Guseynov, Azerbaijan  
Almuk Abbasov, Azerbaijan  
Yusif Asadov, Azerbaijan

### **TECHNICAL EDITORIAL BOARD**

Senior secretary: Elmira Akhundova; Nazli Huseynova, Gulnura Jafarova  
Nigar Akhundova, Elshana Aleskerova, Rena Nayimbayeva

### **PUBLISHING OFFICE**

131, H. Javid ave., AZ-1143, Baku  
ANAS, G.M. Abdullayev Institute of Physics

Tel.: (99412) 539-51-63, 539-32-23  
Fax: (99412) 537-22-92  
E-mail: [jophphysics@gmail.com](mailto:jophphysics@gmail.com)  
Internet: [www.physics.gov.az](http://www.physics.gov.az)  
<https://jophphysics.wixsite.com/ajpphysics>

Published at "AZERİ-DİZAYN"  
196, Nizami str., Baku  
Typographer: Filipp Podosinnikov

Sent for printing on: \_\_.\_\_. 201\_\_  
Printing approved on: \_\_.\_\_. 201\_\_  
Physical binding: \_\_\_\_\_  
Number of copies: \_\_\_\_\_ 200  
Order: \_\_\_\_\_

It is authorized for printing:

## DIELECTRIC RELAXATION IN THE COLLOID FULLERENES - LIQUID CRYSTAL 5CB

G.F. GANIZADE

*G.M. Abdullayev Institute of Physics of Azerbaijan NAS*

*131, H. Javid ave., Baku, AZ 1143*

*tdibragimov@mail.ru*

Influence of fullerenes  $C_{60}$  on dielectric properties of liquid crystal 5CB (4'-Pentyl-4-biphenylcarbonitrile) is investigated. It is shown that at additive of fullerenes the components of the dielectric permittivity decrease, and the longitudinal component decreases by greater extent than its transverse component. The dielectric anisotropy also decreases. The dielectric absorption is shifted to low frequencies. The experimental results are explained by the Maier- Meier theory for anisotropic liquids.

**Keywords:** Liquid crystal; fullerenes; dielectric permittivity; phase transition

**PACS:** 64.70.mj; 64.70.pv; 77.84.Nh; 82.70.Dd.

### 1. INTRODUCTION

The progress of nanotechnology has led to the idea to combine the properties of nanoparticles with peculiarities of optic effects in liquid crystals (LC). Additive of nanoparticles into LC can essentially change its properties as they are distributed between LC molecules at low concentration. Fullerenes have a spherical shape and definitive dimension about 1 nm. The injection of fullerenes into LC leads to the structurization and self-organization of the system [1].

Currently, there is a small number of works devoted to liquid crystalline colloids based on pristine fullerenes. Particularly, influence of bias voltage on the liquid crystalline colloid based on pure fullerenes is investigated in work [2]. Results of influence of laser radiation on electro-optic properties of similar colloids are presented in the work [3]. Determination of phase transition from nematic to isotropic state in fullerenes-doped nematic liquid crystal E7 from temperature dependence of conductivity and dielectric parameters was carried out in work [4].

The aim of present work is the study of influence of fullerenes  $C_{60}$  on dielectric properties of the nematic liquid crystal 4-cyano-4'-pentylbiphenyl.

### 2. EXPERIMENTAL

We used nematic liquid crystal 4-cyano-4'-pentylbiphenyl (5CB) with positive dielectric anisotropy as a matrix. The fullerenes  $C_{60}$  (U.S. Research Nanomaterials, Inc.) were added into the liquid crystal with 0.5 wt.% and were shaken in a vortex mixer for 1 hour at temperature 45°C, followed by sonication with dispergator Ultrasonic Cleaner NATO CD-4800 (China) for 4 hours.

The cell had a sandwich structure and consisted of two plane-parallel glass plates whose inner surfaces were coated with thin transparent and conductive indium-tin-oxide (ITO) layer. Planar orientation of molecules was attained by coating the inner substrate surfaces with rubbed polyimide layers. For obtaining of homeotropic orientation of LC molecules, we used

the surfactant (polysiloxane). The cell thickness was fixed with calibrated 20  $\mu\text{m}$  polymer spacers for measurements. Both the colloid and the pure LC were injected into the empty cell by capillary action at the isotropic state. The stuffed cell was kept in the special heater with temperature regulator GL-100 (China). The copper-constantan thermocouple was used for temperature control. An accuracy of temperature determination was 0.1°C.

Dielectric measurements were carried out by the Precision LCR Meter 1920 (IET Labs. Inc., USA) in the frequency range of 100 Hz – 1 MHz and at temperatures between 22°C–60°C. In this case, applied voltage was 0.2 V for planar LC molecular orientation while we carried out the measurements for homeotropic LC orientation using the applied voltage 1 V.

### 3. RESULTS AND DISCUSSION

According to [5], particles do not disturb the director field of a LC if the anchoring parameter  $\zeta = WR/K$  is much smaller than 1, where  $W$  is the anchoring energy of LC molecules with particle surfaces;  $2R$  is particle size;  $K$  is the LC elastic constant. The values of anchoring energy are within  $10^{-4}$ – $10^{-6}$  J/m<sup>2</sup>, the elastic constant of LC has an order of  $10^{-12}$  N, and the fullerenes have sizes of 1 nm. Elementary calculations show that the anchoring parameter has an order between  $10^{-1}$ – $10^{-3}$ . It is much less than 1. Thus, the overall disturbance of the director field by fullerenes does not appear still less at similar concentration. Hence, the obtained colloids can be considered as a homogeneous media and they should behave as pure LCs but with the modified parameters.

Observation under polarisation microscope has shown that the clearing temperature decreases from 35.2°C to 34.1°C. Spherical particles of fullerenes infiltrate between LC molecules reducing interaction in between. At this case, there is disordering of LC directions. As a result, temperature of transition from isotropic to nematic phase decreases according to expression [6]:

$$T_c = (1-f_o) T_p$$

where  $f_o$  is volume concentration of particles,  $T_p$  and  $T_c$  are clearing temperatures of the pure LC and the colloid, correspondingly.

The frequency dependences of real  $\varepsilon'$  and imaginary  $\varepsilon''$  parts of dielectric permittivity of both the pure LC and the corresponding colloid at homeotropic and planar configurations and temperature 23°C are presented in fig. 1 and fig. 2.

As one can see, both components of dielectric permittivity decreases at the additive of fullerenes. Particularly,  $\varepsilon_{||}'$  changes from 19.54 to 16.99 while  $\varepsilon_{\perp}'$  reduces from 6.48 to 5.10 in the middle frequency region. As a result, dielectric anisotropy changes from 13.06 up to 11.89. A presence of fullerenes also decreases the value  $\varepsilon''$ . In addition, a peak of dielectric absorption is observed (the maximum value of  $\varepsilon''$ ) at homeotropic configuration of the sample. At this case, the additive of fullerenes shifts a maximum of dielectric absorption from 590 kHz to 230 kHz at 23°C.

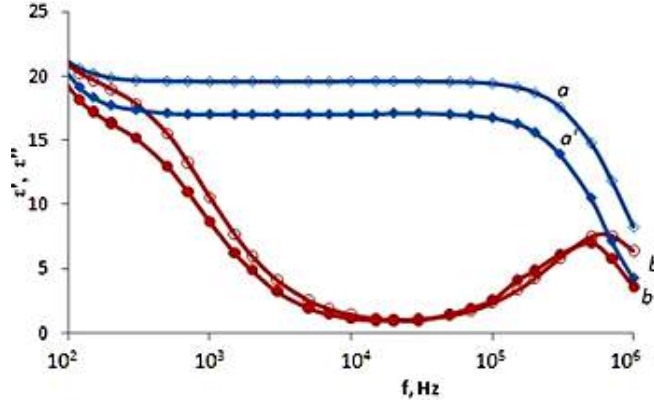


Fig. 1. Frequency dependence of the real  $\varepsilon'$  and imaginary  $\varepsilon''$  parts of the dielectric permittivity at the homeotropic configuration: (a)  $\varepsilon'$  of pure 5 CB, (a')  $\varepsilon'$  of the colloid, (b)  $\varepsilon''$  of the pure 5 CB, (b')  $\varepsilon''$  of the colloid.

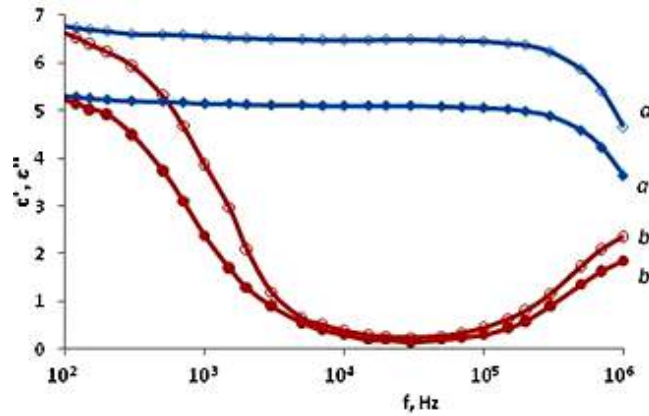


Fig. 2. Frequency dependence of the real  $\varepsilon'$  and imaginary  $\varepsilon''$  parts of the dielectric permittivity at the homeotropic configuration: (a)  $\varepsilon'$  of pure 5 CB, (a')  $\varepsilon'$  of the colloid, (b)  $\varepsilon''$  of the pure 5 CB, (b')  $\varepsilon''$  of the colloid.

The observed experimental facts can be explained by the Maier-Meier theory for anisotropic liquids, according to which the expression for both components of the dielectric permittivity are defined as follows [7]:

$$\varepsilon'_{||} = 1 + \frac{NHF}{\varepsilon_0} \left\{ \gamma_{av} + \frac{2}{3} S \Delta \gamma + F \frac{P_e^2}{3k_B T} \left[ 1 - \frac{1}{2} (1 - 3 \cos^2 \beta) S \right] \right\}$$

$$\varepsilon'_{\perp} = 1 + \frac{NHF}{\varepsilon_0} \left\{ \gamma_{av} - \frac{1}{3} S \Delta \gamma + F \frac{P_e^2}{3k_B T} \left[ 1 + (1 - 3 \cos^2 \beta) S \right] \right\}$$

Dielectric anisotropy is the difference of these quantities:

$$\Delta\epsilon' = \frac{NHF}{\epsilon_0} \left[ \Delta\gamma - F \frac{pe^2}{2k_B T} (1 - 3\cos^2 \beta) \right] S$$

where  $F$  is reaction field factor,  $H$  is the cavity form factor,  $\gamma_{av} = (\gamma_{||} + 2\gamma_{\perp})/3$  is the average value of polarizability of LC molecules,  $\Delta\gamma = \gamma_{||} - \gamma_{\perp}$  is the anisotropy of polarizability,  $N$  is the number of LC molecules per unit volume,  $S$  is the order parameter,  $\beta$  is an angle between the point molecular dipole  $p_e$  and the axis of maximum molecular polarizability,  $\epsilon_0$  is dielectric permittivity of vacuum,  $k_B$  is Boltzmann constant,  $T$  is Kelvin temperature. Since the concentration of the colloid is very small, the number of embedded particles per unit volume is also small. That is, the number of LC molecules per unit volume  $N$  decreases slightly. A different matter the order parameter  $S$  which is defined as follows:

$$S = \frac{1}{2} (3\langle \cos \theta \rangle - 1)$$

The embedded particles increase the instantaneous angle  $\theta$  between the individual molecules and the preferred direction of the molecules (director). In this regard, the order parameter is significantly reduced. The second term in the curly brackets of the expressions for components of dielectric permittivity containing the order parameter has opposite sign. As a result, the longitudinal component decreases more strongly than its transverse component at the presence of fullerenes. Moreover, the anisotropy of the dielectric permittivity  $\Delta\epsilon'$  is directly proportional to the order parameter  $S$  and the number of molecules  $N$  per unit volume. Hereat, it also decreases. It is consistent with our experimental data.

Fig. 3 shows the temperature dependence of the frequency of the dielectric absorption peak for the pure LC and the colloid.

As can be seen, the frequency of the dielectric absorption peak of the colloid is less than for the LC at all temperatures. The frequency of the dielectric absorption peak of the pure LC varies from 590 kHz (23°C) to 750 kHz (30°C) while it increases from 230 kHz (23°C) to 650 kHz (30°C) for the colloid.

As is well known, the relaxation time  $\tau$  of LC molecules is characterized by flip-flop motion of molecules about their short axes. It is determined as follows:

$$\tau = \frac{1}{2\pi \cdot f}$$

where  $f$  is the frequency of the applied electric field.

The addition of fullerenes increases the relaxation time from  $2.7 \cdot 10^{-7}$  to  $7.3 \cdot 10^{-7}$  s at 23°C and from  $2.4 \cdot 10^{-7}$  sec to  $6.9 \cdot 10^{-7}$  sec at 30°C. Obviously, the increase in the relaxation time connects to the originated obstacles to the flip-flop motion of LC molecules. Temperature also affects on the relaxation time: an increase in temperature reduces viscosity. As

a result, the flip-flop motion of LC molecules becomes easier.

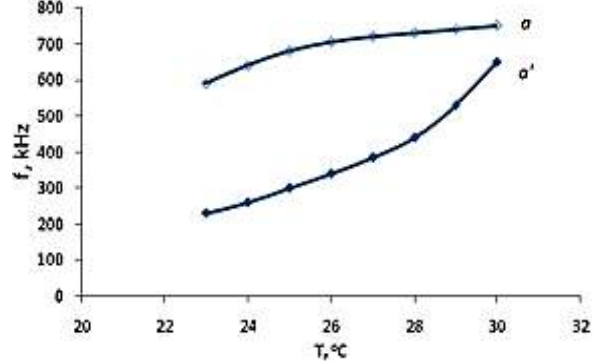


Fig. 3. Temperature dependence of the frequency of a local maximum of  $\epsilon''$ : (a) the pure 5CB, (a') the colloid.

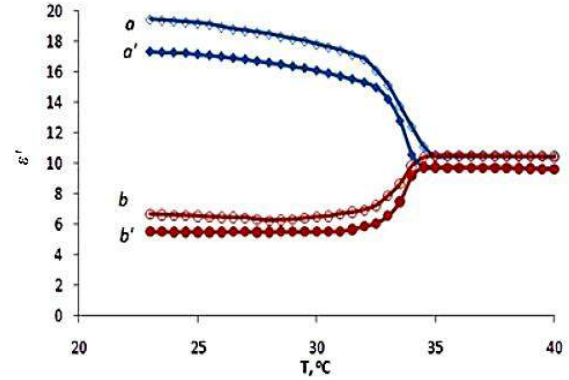


Fig. 4. Temperature dependence of the longitudinal and transverse components of the dielectric permittivity at the frequency of 10 kHz: (a)  $\epsilon_{||}'$  of the pure 5CB, (a')  $\epsilon_{||}'$  of the colloid, (b)  $\epsilon_{\perp}'$  of the pure 5CB, (b')  $\epsilon_{\perp}'$  of the colloid.

The temperature dependence of the parallel and perpendicular components of the dielectric permittivity of both the pure LC and the colloid at frequency of 10 kHz is shown in fig. 4.

As can be seen, the longitudinal component of the dielectric permittivity of the pure LC decreases from 19.48 (23°C) to 13.81 (34°C) while the transverse component changes from 6.68 (23°C) to 10.60 (34°C).

The dielectric permittivity of the colloid is shifted to lower values at all temperatures. In this case, the longitudinal component of the dielectric permittivity of the colloid decreases from 17.35 (23°C) to 10.60 (34°C). The transverse component increases from 5.53 (23°C) to 9.18 (34°C). In the isotropic phase, the dielectric permittivity slightly decreases from 10.53 (36°C) to 10.47 (40°C). In the fourth term, the dependence of the longitudinal and transverse components of the dielectric permittivity in the Maier-Meier equations also includes the temperature of the sample. With increasing temperature, the values of these quantities decrease. It agrees with the experiment.



- 
- [1] *N.V. Kamanina.* Fullerene-dispersed nematic liquid crystal structures: dynamic characteristics and self-organization processes, *Physics- Uspekhi* 48, 419-427, 2005 (in Russian).
  - [2] *S.E.San, M.Okutan, O.Koysal, Y.Yerli.* Carbon Nanoparticles in Nematic Liquid Crystals *Chin. Phys. Lett.* 25, 212-215, 2008.
  - [3] *S.E.San, O.Koysal, M.Okutan.* Laser- induced dielectric anisotropy of a hybrid liquid crystal composite made up of methyl red and fullerene C60, *J. of Non- Crystalline Solids*, 351, 2798-2801, 2005.
  - [4] *M.Okutan,S.E.San,E.Basaran,F.Yakuphanoglu.* Determination of phase transition from nematic to isotropic state in carbon nano-balls' doped nematic liquid crystals by electrical conductivity-dielectric measurements, *Phys. Lett. A*, 339, 461-465, 2005
  - [5] *Yu. Reznikov.* Ferroelectric colloids in liquid crystals, in: Q. Li (Ed.), *Liquid Crystals Beyond Displays: Chemistry, Physics, and Applications*, John Wiley and Sons, Inc., Hoboken, NJ, p.p. 403–426, 2012.
  - [6] *M.V.Gorkunov, M.A.Osipov.* Mean field theory of a nematic liquid crystal doped with anisotropic nanoparticles, *Soft Matter*, 7, 4348–4356, 2011.
  - [7] *W. Maier, G. Meier.* A simple theory of the dielectric are some homogeneous criteria oriented liquid crystal phases of nematic type. *Z. Naturforsch.* 16A, 262–267, 1961.

*Received: 01.07.2019*

## STRUCTURAL FEATURES IN SYSTEMS WATER- POLYETHYLENE GLYCOL -KCl, KBr, KI

B.G. PASHAYEV

*Baku State University, Physics Department,  
23, Z. Khalilov, AZ1073, Baku, Azerbaijan  
E-mail: p.g.bakhtiyar@gmail.com*

In this work, the dynamic viscosity and density of the water-PEG systems, water-PEG-KCl, water-PEG-KBr, and water-PEG-KI were measured in the temperature range 293.15-323.15 K and 0-0.001 mole fraction of PEG. PEG fractions with a molar mass 1000, 1500, 3000, 4000, 6000 and the concentration of salts (KCl, KBr, KI) in the water-PEG-KCl, water-PEG-KBr, water-PEG-KI systems were considered to be 0.01 mole fraction. Using the results of the experiment, the activation parameters of the viscous flow and the partial molar volumes of PEG were calculated, and the dependences of these parameters on the concentration of PEG in this temperature range and concentration of the studied systems were investigated. It was found that PEG has a structural effect on both water and water-KCl, water-KBr and water-KI systems, but the presence of KCl, KBr, KI consistently weakens the structural effect of PEG. This is due to the destructive effects on the structure of KCl, KBr, KI in the corresponding sequence.

**Keywords:** polyethylene glycol, KCl, KBr, KI, aqueous solution, structure of water, activation parameters of viscous flow, partial molar volume.

**PACS:** 61.20.Ne, 66.20.+d, 82.60.Lf, 61.25.Hq.

### 1. INTRODUCTION

It is known that the water is actively involved in all biological, biochemical and biophysical processes occurring in living organisms. Water, as a solvent in these processes, plays an important role in the formation of active conformations of biological functions, all interaction in the body, fermentative reactions, and transportation of chemicals. The functional activity of biological objects is determined by the structure of the water and the physical properties of the aqueous solution depend heavily on the nature of its components. It should be noted that the physical and chemical properties of the aqueous solutions are related to the interaction between water molecules, soluble molecules and water-soluble molecules. Such molecular interaction formates the structure of the solution the expense of hydrogen, ion-dipole and other types of bonds [1]. Water soluble substances change its structure. It affects all the processes that take place. Therefore, the study of water structure, including the study of the effects of various substances to water is actual.

For its practical significance, polyethylene glycol (PEG), KCl, KBr and KI have been the research object of researchers [2-15]. All the molecular mass fractions of polyethylene glycol are well soluble in water [4]. There are hydrophobic (CH<sub>2</sub>) and hydrophilic (OH) groups in the PEG molecule (HO-[CH<sub>2</sub>-CH<sub>2</sub>-O]<sub>n</sub>-H) [1]. The PEG (OH) group and -O- and -H atoms are able to form hydrogen bonds with the water molecule, CH<sub>2</sub> groups produce hydrophobic effect. PEG is widely used in medicine, pharmacology, cosmetology and the food industry because it does not have toxic properties [5]. PEG is able to capsulate solid particles to maintain their sterile stability, maintain surface active substances and reduce friction in different processes [6, 7]. Although PEG has a wide range of applications, the properties of aqueous solutions of its various molecular mass fractions and

the volume properties are less investigated. Also, the analysis of scientific literature shows that it is necessary to investigate structural properties of the water-PEG system and to study the effects of various salts on this system. For this reason, the study of structural properties of water-PEG-KCl, KBr, KI systems is of great importance.

Here the structural features of systems of water-PEG, water-PEG-KCl, water-PEG-KBr and water-PEG-KI at temperature 293.15-323.15 K and 0-0.001 partial molar concentration of PEG were investigated by means of methods viscosimetry and pycnometers. Polyethylene glycol molecules with a molecular weight of 1000, 1500, 3000, 4000 were investigated and the concentration of salts (KCl, KBr, KI) in the systems of water-PEG-KCl, water-PEG-KBr, water-PEG-KI were taken 0,01 molar fraction. The dynamic viscosity and density of aqueous solutions were measured observed temperature and concentration interval and based on experimental results dependence of activation Gibbs energy of viscous flow ( $\Delta G_{\eta}^{\ddagger}$ ),

activation entalpy of viscous flow ( $\Delta H_{\eta}^{\ddagger}$ ), activation entropy of viscous flow ( $\Delta S_{\eta}^{\ddagger}$ ) and the partial molar volume of PEG ( $\bar{V}$ ) in solution of studied systems and the dependencies on concentration of PEG were analyzed.

### 2. EXPERIMENTAL AND THEORETICAL PART

PEG, KCl, KBr and KI were used as our objects of research with molecular weight 1000, 1500, 3000, 4000 and 6000. Used substances are chemical pure. Bidistilled water was used in the preparation of the solutions. The viscosity was measured by capillary viscosimeter and density was measured by pinometer.

Due to activation Gibb's energy of viscous flow ( $\Delta G_{\eta}^{\neq}$ ) according to Frenkel and Eyring theory [1] of liquid viscous flow

$$\Delta G_{\eta}^{\neq} = RT \ln \frac{\eta}{\eta_0} \quad (1)$$

is defined by this expression. Due to Eyring theory [1]  $\eta_0 = \frac{N_A h \rho}{M}$ . Here is  $R$  -universal gas constant,  $N_A$  -is the Avogadro number,  $h$  -is the Planck's constant, and  $M$  -is the molecular weight of solution, determined according to equation  $M = \sum_{i=1}^N x_i M_i$  [1]. Here  $x_i$  and  $M_i$  are the molar fraction and molar weight of the  $i$ -th component, respectively. Dynamic viscosity ( $\eta$ ) and density ( $\rho$ ) of the solution at different temperatures were determined experimentally.

The activation enthalpy of viscous flow ( $\Delta H_{\eta}^{\neq}$ ) was determined by the equation [1]:

$$\Delta H_{\eta}^{\neq} = R \frac{\partial \ln(\eta/\eta_0)}{\partial (1/T)} \quad (2)$$

Thus,  $\Delta G_{\eta}^{\neq}$  and  $\Delta H_{\eta}^{\neq}$  were calculated by (1) and (2). The  $\Delta G_{\eta}^{\neq}$  and  $\Delta H_{\eta}^{\neq}$  values were used for determining the activation entropy of viscous flow ( $\Delta S_{\eta}^{\neq}$ ) by the known thermodynamic equation [1, 16]

$$\Delta G_{\eta}^{\neq} = \Delta H_{\eta}^{\neq} - T \Delta S_{\eta}^{\neq} \quad (3)$$

The partial molar volume ( $\tilde{V}$ ) of the solute in solution was determined by the equation [1, 17]

$$\tilde{V} = V_m + (1-x) \left( \frac{\partial V_m}{\partial x} \right)_{p,T} \quad (4)$$

where  $V_m$  is the molar volume of the solution:

$$V_m = \frac{M}{\rho} = \frac{1}{\rho} \sum_{i=1}^N x_i M_i$$

### 3. RESULTS AND DISCUSSION

The systems of water-PEG, water-PEG-KCl, water-PEG-KBr and water-PEG-KI at the temperature 293,15 K dependence activation Gibb's energy of viscous flow ( $\Delta G_{\eta}^{\neq}$ ), activation enthalpy of viscous flow ( $\Delta H_{\eta}^{\neq}$ ), activation entropy of viscous flow ( $\Delta S_{\eta}^{\neq}$ ) and partial molar volume ( $\tilde{V}$ ) of PEG in solution, the dependence on the PEG concentration ( $x$ ) is shown in figures 1-4.

As can be seen from Table 1-4, for the studied systems the activation parameters of viscous flow ( $\Delta G_{\eta}^{\neq}$ ,  $\Delta H_{\eta}^{\neq}$ ,  $\Delta S_{\eta}^{\neq}$ ) increase with increasing the concentration, while the partial molar volume ( $\tilde{V}$ ) of the PEG decreases. When fluid is calming (not running), the leakage of particles in all directions is

the same. However, the number of particles leaps in the flow direction prevails over other destinations.  $\Delta G_{\eta}^{\neq}$ ,  $\Delta H_{\eta}^{\neq}$  and  $\Delta S_{\eta}^{\neq}$  parameters are equivalent to the difference in the values of the corresponding parameters when activation 1 mole molecule: ( $G_b$ ,  $H_b$ ,  $S_b$ ) to ( $G_a$ ,  $H_a$ ,  $S_a$ ) [1]:  $\Delta G_{\eta}^{\neq} = G_a - G_b$ ,  $\Delta H_{\eta}^{\neq} = H_a - H_b$ ,  $\Delta S_{\eta}^{\neq} = S_a - S_b$ .  $\Delta G_{\eta}^{\neq}$  is the energy used for activation 1 mole molecule,  $\Delta H_{\eta}^{\neq}$  represents the changes in the solution in terms of energy and  $\Delta S_{\eta}^{\neq}$  characterized the changes in solution in terms of structure. Thus, increased  $\Delta G_{\eta}^{\neq}$  with growth of concentration indicates that more energy can be consumed for overcoming potential of molecule, while increase in  $\Delta H_{\eta}^{\neq}$  indicates the system has steadier structure, increase in  $\Delta S_{\eta}^{\neq}$  determines the system is becoming more structured [10-13]. It is known that, the partial molar volume of  $i$ -th component is equivalent to change of volume at addition of 1 mole from this component [1, 10-13].

As can be seen from Table 1-4, the investigated solutions in accordance with every quantity  $\Delta G_{\eta}^{\neq}(x)$ ,  $\Delta H_{\eta}^{\neq}(x)$ ,  $\Delta S_{\eta}^{\neq}(x)$  and  $\tilde{V}(x)$  dependencies are identical.

The  $\Delta S_{\eta}^{\neq}(x)$  and  $\tilde{V}(x)$  dependencies of PEG for fractional molars of  $M_{PEG} = 1500$  molar mass are shown in fig. 1 and 2.

Table 3 and fig. 1 show that, when adding the same concentration ( $x_{KCl} = x_{KBr} = x_{KI} = 0.01$ ) KCl, KBr and KI to the water-PEG system, given temperature and concentration, the value of the  $\Delta S_{\eta}^{\neq}$  parameter decreases in the appropriate sequence. This shows that, when adding KCl, KBr and KI to the water-PEG system, the structure of the PEG solution is weak in sequence. This indicates that KCl, KBr and KI in sequence have a more destructive effect on water-PEG systems. To explain this result, we will based on the hydration process formed by electrostatic interaction between ions and water molecules. In the aqueous solution, the ions change the internal electrostatic field created by polar water molecules. This change is related to the surface current density of the ion. It is natural that small ions with large surface current density relative to large ions with small surface current density, will have a different impact on the water structure. Because of the intensity of the electric field around the ions the surface current density, these ions attract water molecules and create hydrate layer around them. The ion-dipole interaction effect in the ions in the low density of surfaces does not suffice for the formation of the hydrate layer. Note that  $Br^-$  ion compared to  $Cl^-$  ion, since  $I^-$  ion has relatively poor hydration compared to  $Br^-$  ion [18], It seems that, KBr relative to KCl, KI compared to KBr has more destructive effect on water-PEG system in given temperature and concentration.



Table 1.

Dependence activation Gibbs energy viscous flow of water-PEG, water-PEG-KCl, Water-PEG-KBr and water-PEG-KI systems on PEG concentration ( $J/mol$ )  $T = 293.15K$ ,  $x_{KCl} = x_{KBr} = x_{KI} = 0.01$

$x$	$M_{PEG} = 1000$			
	Water-PEG	Water-PEG-KCl	Water-PEG-KBr	Water-PEG-KI
0	9292	9274	9222	9180
0.0001	9373	9353	9299	9258
0.0002	9423	9487	9385	9343
0.0004	9610	9544	9596	9506
0.0006	9735	9749	9776	9583
0.0008	9920	9803	9862	9864
0.001	10064	10051	10009	9975
$x$	$M_{PEG} = 1500$			
	Water-PEG	Water-PEG-KCl	Water-PEG-KBr	Water-PEG-KI
0	9292	9274	9222	9180
0.0001	9463	9444	9395	9352
0.0002	9682	9585	9589	9550
0.0004	10023	10009	9908	9939
0.0006	10405	10297	10362	10437
0.0008	10735	10883	10870	10623
0.001	11149	11146	11117	11096
$x$	$M_{PEG} = 3000$			
	Water-PEG	Water-PEG-KCl	Water-PEG-KBr	Water-PEG-KI
0	9292	9274	9222	9180
0.0001	9561	9543	9495	9455
0.0002	9862	9847	9804	9768
0.0004	10435	10580	10389	10563
0.0006	10937	10999	10818	10946
0.0008	11552	11409	11522	11291
0.001	12062	12061	11876	12015
$x$	$M_{PEG} = 4000$			
	Water-PEG	Water-PEG-KCl	Water-PEG-KBr	Water-PEG-KI
0	9292	9274	9222	9180
0.0001	9711	9592	9649	9611
0.0002	10162	10177	10111	10079
0.0004	10978	10909	10832	11124
0.0006	11749	11502	11835	11502
0.0008	12449	12371	12296	12410
0.001	13081	13015	13063	13047
$x$	$M_{PEG} = 6000$			
	Water-PEG	Water-PEG-KCl	Water-PEG-KBr	Water-PEG-KI
0	9292	9274	9222	9180
0.0001	10525	10504	10485	10459
0.0002	11656	11346	11326	11618
0.0004	13417	13427	13411	12994
0.0006	14938	15248	14635	14527
0.0008	16154	16164	15949	16150
0.001	17261	17572	17256	16899

Table 2.  
Dependence activation enthalpy of viscous flow of water-PEG, water-PEG-KCl, Water-PEG-KBr and water-PEG-KI systems on PEG concentration ( $J/mol$ ) ( $T = 293.15K$ ,  $x_{KCl} = x_{KBr} = x_{KI} = 0.01$ )

$x$	$M_{PEG} = 1000$			
	Water-PEG	Water-PEG-KCl	Water-PEG-KBr	Water-PEG-KI
0	17397	16665	16489	16400
0.0001	17543	17007	16618	16586
0.0002	17643	17156	16936	16734
0.0004	17897	17339	17274	17015
0.0006	18059	17546	17457	17288
0.0008	18333	17599	17698	17549
0.001	18503	18041	17889	17663
$x$	$M_{PEG} = 1500$			
	Water-PEG	Water-PEG-KCl	Water-PEG-KBr	Water-PEG-KI
0	17397	16665	16489	16400
0.0001	17633	17110	16923	16712
0.0002	17908	17340	17221	17010
0.0004	18407	17814	17578	17709
0.0006	18870	18331	18294	18216
0.0008	19390	18932	18984	18590
0.001	19869	19489	19267	19212
$x$	$M_{PEG} = 3000$			
	Water-PEG	Water-PEG-KCl	Water-PEG-KBr	Water-PEG-KI
0	17397	16665	16489	16400
0.0001	17747	17230	17033	16489
0.0002	18158	17660	17516	17314
0.0004	18858	18568	18284	18286
0.0006	19654	19113	18867	18974
0.0008	20271	19767	19803	19414
0.001	21006	20657	20406	20272
$x$	$M_{PEG} = 4000$			
	Water-PEG	Water-PEG-KCl	Water-PEG-KBr	Water-PEG-KI
0	17397	16665	16489	16400
0.0001	17926	17180	17180	17026
0.0002	18508	17948	17827	17707
0.0004	19465	19106	18826	18969
0.0006	20452	19818	20094	19632
0.0008	21315	20893	20697	20715
0.001	22158	21817	21756	21585
$x$	$M_{PEG} = 6000$			
	Water-PEG	Water-PEG-KCl	Water-PEG-KBr	Water-PEG-KI
0	17397	16665	16489	16400
0.0001	18818	18214	18068	18050
0.0002	20093	19266	19165	19326
0.0004	22091	21784	21584	21089
0.0006	23880	23736	23180	22926
0.0008	25262	24981	24688	24896
0.001	26685	26712	26328	25721

Table 3.

Dependence activation entropy of viscous flow of water-PEG, water-PEG-KCl, Water-PEG-KBr and water -PEG-KI systems on PEG concentration ( $J/mol$ ) ( $T = 293.15K$ ,  $x_{KCl} = x_{KBr} = x_{KI} = 0.01$ )

$x$	$M_{PEG} = 1000$			
	Water-PEG	Water-PEG-KCl	Water-PEG-KBr	Water-PEG-KI
0	27,65	25,21	24,79	24,63
0.0001	27,87	26,11	24,97	25,00
0.0002	28,04	26,16	25,76	25,21
0.0004	28,27	26,59	26,19	25,61
0.0006	28,39	26,60	26,20	26,29
0.0008	28,70	26,59	26,73	26,21
0.001	28,79	27,25	26,88	26,23
$x$	$M_{PEG} = 1500$			
	Water-PEG	Water-PEG-KCl	Water-PEG-KBr	Water-PEG-KI
0	27,65	25,21	24,79	24,63
0.0001	27,87	26,15	25,68	25,11
0.0002	28,06	26,46	26,04	25,45
0.0004	28,60	26,63	26,17	26,51
0.0006	28,87	27,41	27,06	26,54
0.0008	29,52	27,46	27,68	27,18
0.001	29,75	28,46	27,80	27,68
$x$	$M_{PEG} = 3000$			
	Water-PEG	Water-PEG-KCl	Water-PEG-KBr	Water-PEG-KI
0	27,65	25,21	24,79	24,63
0.0001	27,93	26,22	25,72	25,22
0.0002	28,30	26,65	26,31	25,74
0.0004	28,73	27,25	26,93	26,35
0.0006	29,74	27,68	27,46	27,38
0.0008	29,74	28,51	28,25	27,71
0.001	30,51	29,32	29,10	28,17
$x$	$M_{PEG} = 4000$			
	Water-PEG	Water-PEG-KCl	Water-PEG-KBr	Water-PEG-KI
0	27,65	25,21	24,79	24,63
0.0001	28,02	25,88	25,69	25,29
0.0002	28,47	26,51	26,32	26,02
0.0004	28,95	27,96	27,27	26,76
0.0006	29,69	28,37	28,17	27,73
0.0008	30,24	29,07	28,66	28,33
0.001	30,96	30,03	29,65	29,13
$x$	$M_{PEG} = 6000$			
	Water-PEG	Water-PEG-KCl	Water-PEG-KBr	Water-PEG-KI
0	27,65	25,21	24,79	24,63
0.0001	28,29	26,30	25,87	28,89
0.0002	28,78	27,02	26,74	26,29
0.0004	29,59	28,51	27,88	27,61
0.0006	30,50	28,95	29,15	28,65
0.0008	31,07	30,08	29,81	29,84
0.001	32,15	31,18	30,94	30,09

Table 4.  
Dependence of partial molar volume of PEG in water-PEG, water-PEG-KCl, Water-PEG-KBr systems and water-PEG-KI systems on PEG concentration ( $J/mol$ ) ( $T = 293.15K$ ,  $x_{KCl} = x_{KBr} = x_{KI} = 0.01$ )

$x$	$M_{PEG} = 1000$			
	Water-PEG	Water-PEG-KCl	Water-PEG-KBr	Water-PEG-KI
0	865	848	827	804
0.0001	857	837	816	795
0.0002	849	827	807	787
0.0004	835	811	790	772
0.0006	823	797	778	760
0.0008	813	788	770	750
0.001	804	781	765	743
$x$	$M_{PEG} = 1500$			
	Water-PEG	Water-PEG-KCl	Water-PEG-KBr	Water-PEG-KI
0	1343	1310	1275	1247
0.0001	1319	1284	1251	1224
0.0002	1297	1261	1230	1203
0.0004	1257	1221	1192	1164
0.0006	1225	1189	1161	1131
0.0008	1199	1167	1137	1104
0.001	1180	1153	1120	1082
$x$	$M_{PEG} = 3000$			
	Water-PEG	Water-PEG-KCl	Water-PEG-KBr	Water-PEG-KI
0	2829	2670	2611	2558
0.0001	2782	2632	2572	2514
0.0002	2738	2597	2536	2474
0.0004	2663	2534	2472	2407
0.0006	2602	2480	2420	2357
0.0008	2557	2436	2380	2325
0.001	2527	2403	2351	2311
$x$	$M_{PEG} = 4000$			
	Water-PEG	Water-PEG-KCl	Water-PEG-KBr	Water-PEG-KI
0	3785	3602	3512	3444
0.0001	3710	3535	3449	3376
0.0002	3639	3471	3388	3312
0.0004	3513	3356	3278	3198
0.0006	3405	3258	3182	3102
0.0008	3316	3175	3100	3023
0.001	3246	3108	3032	2962
$x$	$M_{PEG} = 6000$			
	Water-PEG	Water-PEG-KCl	Water-PEG-KBr	Water-PEG-KI
0	5085	5017	4903	4799
0.0001	5050	4983	4864	4752
0.0002	5016	4950	4828	4711
0.0004	4955	4889	4765	4642
0.0006	4903	4833	4714	4592
0.0008	4859	4782	4676	4562
0.001	4824	4736	4649	4551

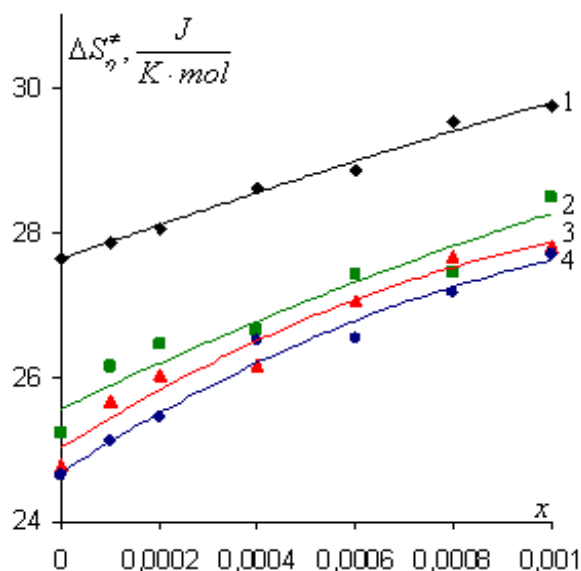


Fig.1. Dependence activation entropy of viscous flow of Water-PEG (1), water-PEG-KCl (2), water-PEG-KBr (3) and water-PEG-KI (4) systems on PEG concentration.

$$(M_{PEG} = 1500, T = 293.15K, x_{KCl} = x_{KBr} = x_{KI} = 0.01)$$

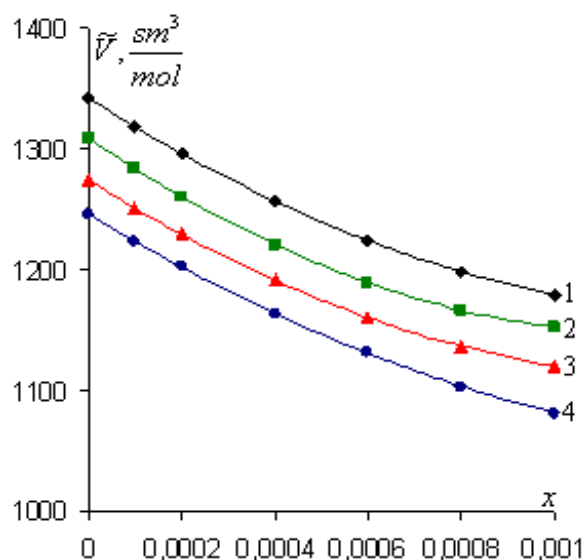


Fig.2. Dependence of partial molar volume of PEG in water PEG, water-PEG-KCl, water-PEG-KBr and water-KI systems on PEG concentration.

As can be seen in table 4 and fig. 2, for the studied systems, the partial molar volume ( $\bar{V}$ ) of the PEG in the solution decreases with the increase in PEG concentration. We can say that when large-scale associates are divided into a volume fraction and volume fraction of its individual parts smaller than their sum. According to model of the two-structured water [19], water consists of clusters of the different size and clusters of molecules of free liquid which are attached to hydrogen binding. Due to dependence of partial molar volume on concentration, it is possible to assume that the molecules of PEG are connected first of all by hydrogen binding with free molecules of water. This, with the increase in concentration in the

solution causes a decrease in the partial molar volume of the PEG. This indicates that the solution has become more structured due to increase in PEG concentration.

#### 4. CONCLUSION

Depending on the concentration of both the entropy of the activated flow and the partial molar volume of PEG in solution, we can say that the PEG has a structural impact on both water and KCl, water-KBr and water-KI systems, but the presence of KCl, KBr, KI weakens the structural impact of the PEG in sequence.

- [1] E.A. Masimov, H.Sh. Hasanov, B.G. Pashayev. Liquid viscosity. Baku, "Publishing House Laman", p. 285, 2016.
- [2] C. Goncalves, N. Trevisan, A. Meirelles. Kinematic Viscosity of Systems Containing Polyethylene Glycol+Salt+Water at 298.2 K. J. Chem. Eng.50, p.177-181, 2005.
- [3] I.V. Shulyak, E.I. Grushova, A.M. Semchenko. Russian Journal of Phys. Chem., vol. 85, № 3, p. 419-422, 2011
- [4] F.F.Bailey, J.V.Koleske. Poly(Ethylene Oxide). Academic press: NY, p.173, 1976.
- [5] K.P. Lange. Surfactants, synthesis, properties, analysis, application. "Professiya", p.240,2005.
- [6] D.H. Napper. J.Colloid and Interface Sci., v.58, №2, p. 390-407, 1977.
- [7] Th.F. Tadroq, B. Vincent. J.Colloid and Interface Sci., v. 66, №1, p. 77-84, 1978.
- [8] I.V. Shulyak, E.I. Grushova. Russian Journal of Phys. Chem.,vol. 87, № 3, p. 453-456, 2013.
- [9] C. Bhanot, S. Trivedi, A. Gupta, S. Pandey. Dynamic viscosity versus probe-reported microviscosity of aqueous mixtures of poly(ethylene glycol). J. Chem. Thermodyn., 45, p.137-144, 2012.
- [10] E.A. Masimov, B.G. Pashayev, H.Sh. Hasanov, S.I. Musayeva. Russian Journal of Physical Chemistry, vol. 87, № 12, p. 2105-2107, 2013.
- [11] E.A. Masimov, B.G. Pashayev, H.Sh. Hasanov, N.H.Hasanov. Russian Journal of Phys. Chem., vol. 89, №7, p. 1244-1247, 2015.
- [12] E.A. Masimov, B.G. Pashayev, H.Sh. Hasanov. Russian Journal of Physical Chemistry, vol. 93, № 5, p. 988-990, 2019.
- [13] E.A. Masimov, B.G. Pashayev. Azerbaijan Journal of Phys., vol. XXIV, №4,p.19-22,2018.

- [14] *E.A. Masimov, B.G. Pashayev, H.Sh. Hasanov.* Russian Journal of Physical Chemistry, vol. 93, № 6, p. 1054-1058, 2019.
- [15] *Sh.N. Hajiyeva.* Russian Journal of Phys. Chem., vol. 93, № 6, p. 1054-1058, 2019.
- [16] *M.A. Sibileva, E.V. Tarasova.* Russian Journal of Phys. Chem., vol. 78, №7, p.1240-1244, 2004.
- [17] *A.A. Tager.* Physico-chemistry of polymers. M.: Scientific world, p. 576, 2007.
- [18] *P. Atkins. De Paula J.* Phys. Chem. Oxford University Press., p. 1067, 2006.
- [19] *O.Y. Samoylov.* The structure of aqueous solutions of electrolytes and ion hydration. M., AN SSSR, 1957, p.76-182.
- [20] *G. Nemethy.* The structure of water and the thermodynamic properties of aqueous solutions. Istituto superiore di sanita-V.le Regina Elena, 299-Roma. vol. VI, fascicolo speciale 1, p. 492-592, 1970.

*Received: 04.07.2019*



## INVESTIGATION OF SILICON PHOTOMULTIPLIER AT LOW TEMPERATURE

F.I. AHMADOV

*Azerbaijan National Academy of Sciences  
Institute of Radiation Problems,  
9, B.Vahabzade, Baku, AZ1143*

The physical properties of silicon-based MSFD-3NK photomultiplier was developed under the MAPD Collaboration were investigated at low temperatures. The value of temperature coefficient of breakdown voltage is typically  $58 \pm 3 \text{ mV}/^\circ\text{C}$  for MSFD-3NK photodiodes. The dark count of a single electron decreased by 169 times when the temperature difference was  $-81^\circ\text{C}$ . It was obtained that afterpulsing played a significant role in the generation of dark count in low temperature. Amplitude resolution of single photoelectron reduced and it reached 32% when temperature difference was  $-93^\circ\text{C}$ . Thus, the possibility of applying these photodiodes to low temperature detectors has been confirmed.

**Keywords:** Micro pixel avalanche photodiode; MAPD; liquid nitrogen; dark matter; inert gases.

**PACS:** 07.77-n; 07.77.-Ka; 29.40Wk; 85.30De; 85.60Dw

### 1. INTRODUCTION

One of the main problems of modern astrophysics and particle physics is the registration of light particles forming dark matter. Although, despite the fact that dark matter particles make up 27% of the total weight of the Universe, the probability of their registration is very low [1]. The interaction of these particles with the environment is based on a weak interaction mechanism. In this case, the probability of their registration is sharply reduced. Inert gases of high pressure as well as xenon and argon gases are used to detect these particles. The detectors used in these experiments operate at low temperatures. The particles transfer a small part of their energy to the xenon and argon atoms in an elastic interaction condition. In this case, atoms that receive very little energy from particles generate a very small amount of scintillation photons [2, 3-5]. The accurate registration of these scintillation photons is very important for correctly determining the parameters of dark matter particles incident on the detector. Currently, for register scintillation photons produced in xenon and argon detectors, using photomultiplier tubes [1]. However, the main disadvantage of these detectors is that they have photon detection efficiency of less than 20%, high operation voltage, sensitivity to a magnetic field and are radiation contaminated [6, 7]. These shortcomings cast doubt on the reliability of the results of the events mentioned in most experiments. For this reason, when preparing such detectors, the use of low-temperature and radioactively uncontaminated photo detectors is highly relevant. One of the possible candidates as photo detectors is also silicon micro pixel avalanche photodiodes (MAPD). Photodiodes of the MAPD-3NK type, prepared by the MAPD collaboration in 2014, have 40% photon detection efficiency, low operating voltage, and do not have radioactive contamination and are used as photo detectors in various experiments [8]. However, the fact that photodiodes of the MAPD-3NK type have not been studied at low temperatures does not allow

their use in low-temperature detectors. Therefore, it is important to investigate the parameters of MAPD-3NK photodiodes at low temperatures. The work was devoted to the study of changes in the parameters of photodiodes MAPD-3NK in the temperature range from  $-108^\circ\text{C}$  to  $-20^\circ\text{C}$ .

### 2. EXPERIMENTAL SETUP AND RESULTS

In the work were applied MAPD-3NK photodiodes, developed in frame of MAPD collaboration. The experiments were conducted at the Joint Institute for Nuclear Research in Russia. The selected samples had the following parameters: a pixel density of 10,000 pixels /  $\text{mm}^2$ , a working voltage of 90 V, a capacity of 180 pF, a photon detection efficiency of 40%, and size  $3.7 * 3.7 \text{ mm}^2$ . To ensure a low temperature, liquid nitrogen was used and the temperature was varied by adjusting the depth of the sample location. During the measurements, the temperature change was 1%. The prepared experimental circuit is shown in fig. 1. The experimental setup included amplifiers (G1 and G2), a light diode (LED), a Keithley-6487 voltage source, CAEN-5720-analog-digital converter, pulse generator, and a resistor which measured the temperature. The amplifier (G1) located in nitrogen and has a gain of 50, the gain of second amplifier (G2) outside the cryostat was 38. When studying the properties of the MAPD-3NK photodiode, a 1 mm fiber optic cable was used to transmit light to the photodiode. Thus, the influence of the LED on the temperature changes of the photodiode was excluded. Silica gel was also used to prevent the formation of liquid vapors on the surface of the photodiode at low temperatures. Further, the received signal was processed by an analog- digital converter CAEN-5720 and stored on a computer. In signal processing, algorithms written in the C++ programming language were applied.

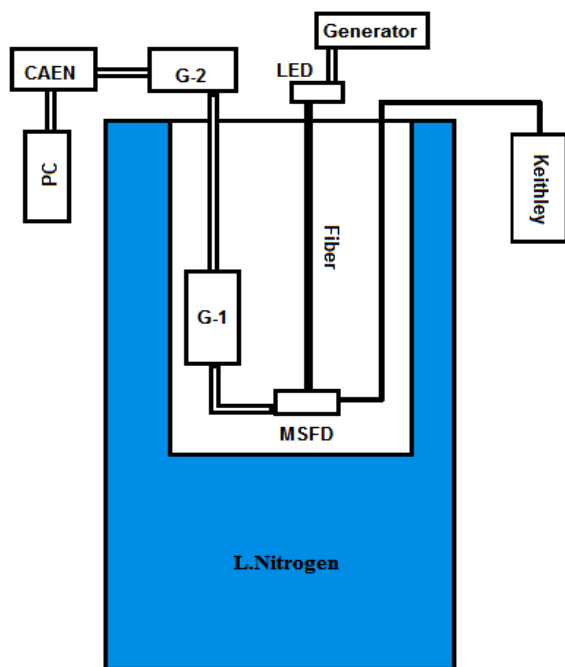


Fig. 1. Experimental setup

The following parameters of the MAPD-3NK photodiodes were investigated: the breakdown voltage, the dependence of the dark count (DC), and the amplitude resolution corresponding to the first photopeak of the amplitude on temperature. Pulse generator, CAEN-5720 ADC and amplifiers were used during the measurement of the breakdown voltage and the registration of a low photon flux. The total signal gain ( $G1 \cdot G2$ ) was 1900. When recruiting the spectrum, CAEN connected to a synchronized generator output, and minimal integration limits were chosen. First of all, the temperature dependence of the parameters of the amplifier (G1) used at low temperatures was investigated. It was found that the gain of the applied amplifier varies according to the law depending on the temperature:  $G = 483.2 + 0.1212 \times T - 0.0109 \times T^2$ . At the temperature  $-100^\circ\text{C}$ , the gain reduction was below 23%. These changes were taken into account during the measurement. In determining the dependence of the photodiode gain on the temperature, a short negative pulse with a frequency of 1 kHz, duration of 30 ns and amplitude of 3.34V was applied from the pulse generator to the LED (a wavelength of 450 nm). Fig. 2a shows the dependence of the charge corresponding to the first photopeak on the voltage at  $-20^\circ\text{C}$  of the sample MAPD-3NK.

Additionally, a voltage of 2V was applied to the operating voltage of the photodiode at each temperature. As the point of breakdown voltage, the point corresponding to the intersection line of the dependence (Q-V) is selected when  $Q=0$  with the voltage line. As can be seen from fig. 2, the breakdown voltage of the MAPD-3 NK photodiode at  $-20^\circ\text{C}$  was 85.7 V. In the range of applied voltage, the gain of the MAPD-3NK photodiodes varied from 3.3 to  $7.4 \times 10^4$ .

In fig. 2b. shows the dependence of the breakdown voltage MAPD-3NK on temperature. It is revealed that the breakdown voltage of MAPD-3NK varies linearly with temperature:  $U_{br} = 86.64 + 0.058 \times T$ . Here,  $T$  is the ambient temperature, expressed in Celsius. The data obtained show that the temperature coefficient influence to breakdown voltage of MAPD-3NK was  $58 \pm 3 \text{ mV}/^\circ\text{C}$ . In other words, under constant overvoltage conditions, as the temperature increases, the gain decreases and vice versa. In such high field, as the temperature decreases, the gain of the photodiode increases due to an increase in the average length of tracking of charge carriers before the emission of optical phonons. In this case, the charge carriers get more energy between two collisions and therefore the ionization energy (3.6 eV) is reached faster. This allows to reduce the breakdown voltage in the area of low voltages. However, increasing the temperature leads to a decrease in the gain and increase the breakdown voltage, because of an increased likelihood of energy transfer charge carriers into the optical phonons. To increase the gain, it is necessary to increase the electric field in the avalanche region, which is possible with increasing voltage. For this reason, the breakdown voltage of MAPD increases with increasing temperature. However, another quantitative characteristic of ionization is the width of the forbidden band, which varies with temperature. Despite the fact that the temperature range was  $-90^\circ\text{C}$ , the change in the width of the forbidden zone was about 2%.

To determine the pixel capacity of MAPD-3NK, the difference  $dQ/dU$  was calculated and the capacitance  $C_{pix} \sim 4.8 \times 10^{-15} \text{ F} = 4.8 \text{ fF}$  was obtained.

In determining the dark current MAPD-3NK no LEDs were applied. Similarly, the CAEN analog - digital converter was used with two amplifiers. In removing the signal, a trigger from the signal itself was used. It is known that the dark count formed by two components: thermal charge carriers in the avalanche region and afterpulses. The concentration of heat carriers depends on the number of generating centers and temperature. However, when the overvoltage applied to the MAPD photodiodes increases, the charge carriers from the generation center to the conduction band increases due to the field, which, in turn, causes the DC change. Therefore, the measurements were carried out at different temperatures and different gains. Fig. 3a shows the distribution of the amplitude corresponding to dark electrons. The measurement temperature was  $-27^\circ\text{C}$ . The reason for this is that the distribution of the amplitude of a single electron cannot be observed due to the high level of the DC as a result of high temperatures. Amplitudes corresponding to dark electrons were within a few millivolts. Then, the change in the dark count corresponding to the threshold level value of 5 mV was investigated, depending on temperature with the same gain. The choice of the same gain, made it possible to study the effect of temperature on the change of DC. As can be

seen from fig. 3b, the DC varies exponentially with temperature, and the DC drops by about 169 times, when the temperature difference is  $-81^{\circ}\text{C}$ .

In addition, the dependence of the dark count corresponding to the first dark electron on the gain was also considered (fig. 4). In this case, the effect of the gain on the DC was studied. The increase in DC was close to 28%, with an increase in the gain by 36% and a temperature of  $-27^{\circ}\text{C}$ . This is due to the increase in dark electrons and the high probability of an avalanche beginning by charge carriers. However, when the temperature was  $-108^{\circ}\text{C}$  and the gain increased by 36%, the decrease in DC was about 75%. These changes began to be observed only at temperatures below  $-70^{\circ}\text{C}$ . It can be explained only with an increased probability of the occurrence of afterpulses. It is known, that charge carriers, at higher temperatures, have a small probability of being captured by capture centers, which, after releasing them, over a short period of time. However, the time of release of charge carriers from centers at low temperatures varies according to the law  $\tau_i = \tau_0 \times \exp(E_i/kT)$  [4]. Where  $\tau_0$  depends on the type of carriers and the band structure,  $E_i$  of the activation energy of the capture center,  $k$  is the Boltzmann constant and  $T$  is the temperature.

At low temperatures, the probability of carrier delays by capture centers in avalanche process increases dramatically. In these centers, carriers can remain for a long time and be released at different

times. However, at low temperatures, various capture centers release carriers for a certain period of time and trigger the avalanche process in many pixels. As a result, the released carriers shift the amplitude of the signal to the upper energy region. As the gain increases, the amplitude and number of these events increase dramatically. The results show that afterpulses play a key role in the formation of DC at low temperatures, which leads to increase the amplitude. It was also found that the corresponding amplitude increases linearly with increasing gain. Increasing the gain causes an increase in registration efficiency. Therefore, it is very important to choose the same gain in order to investigate the amplitude variation as a function of temperature. In this case, the ratio of the peak corresponding to the first dark electron to the amplitude is established from the spectrum (fig. 5).

With the same gains, the peak corresponding to the first dark electron has an amplitude resolution of 64.7% at  $-30^{\circ}\text{C}$ , 64% at  $-40^{\circ}\text{C}$ , 52% at  $-86^{\circ}\text{C}$ , at  $-123^{\circ}\text{C}$ , 43.5%, respectively. In other words, the amplitude decreases with decreasing temperatures, and with a difference of  $-93^{\circ}\text{C}$ , the reduction of resolution is 32%. Amplitude resolution corresponding to single photoelectron depending on temperature was described by a linear dependence ( $R=72.5+0.2357 \cdot T$ ). The obtained results showed once again that MAPD-3 NK photodiodes can be successfully used for low-temperature detectors.

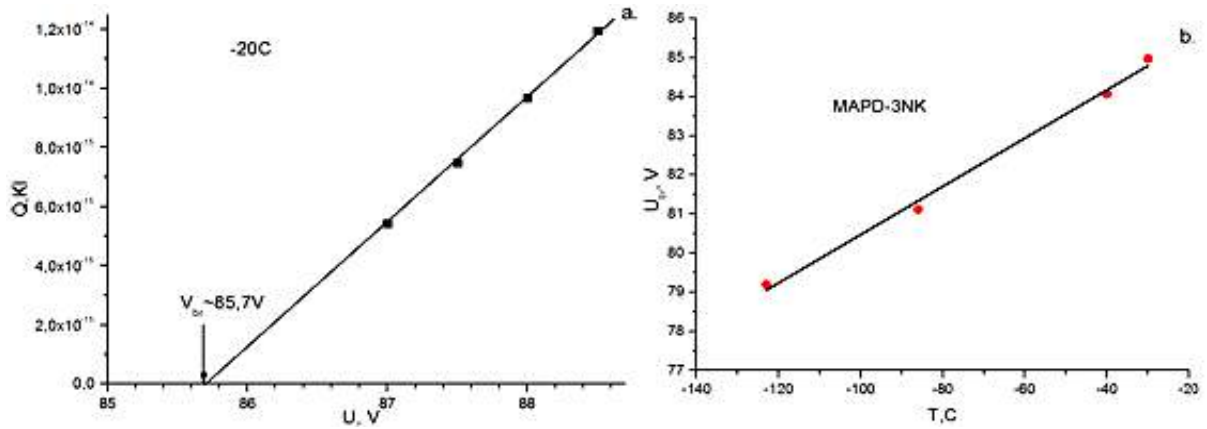


Fig. 2. Dependence of the charge corresponding to a single-electron peak on voltage (a.) and breakdown voltage on temperature (b.) for a MAPD-3NK photodiode

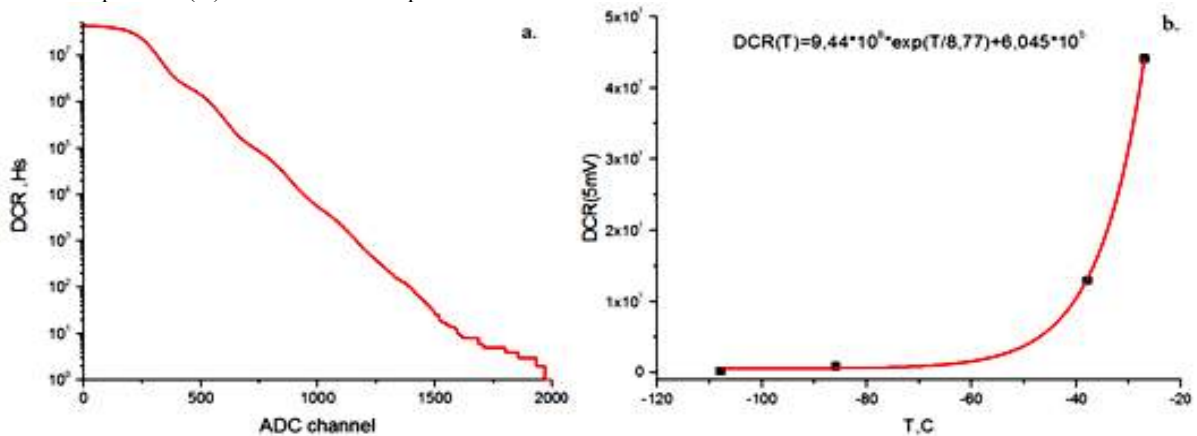


Fig. 3. Dependence of the dark count of MAPD-3NK (a) and the dark count in the threshold level by 5mV (b) on temperature.

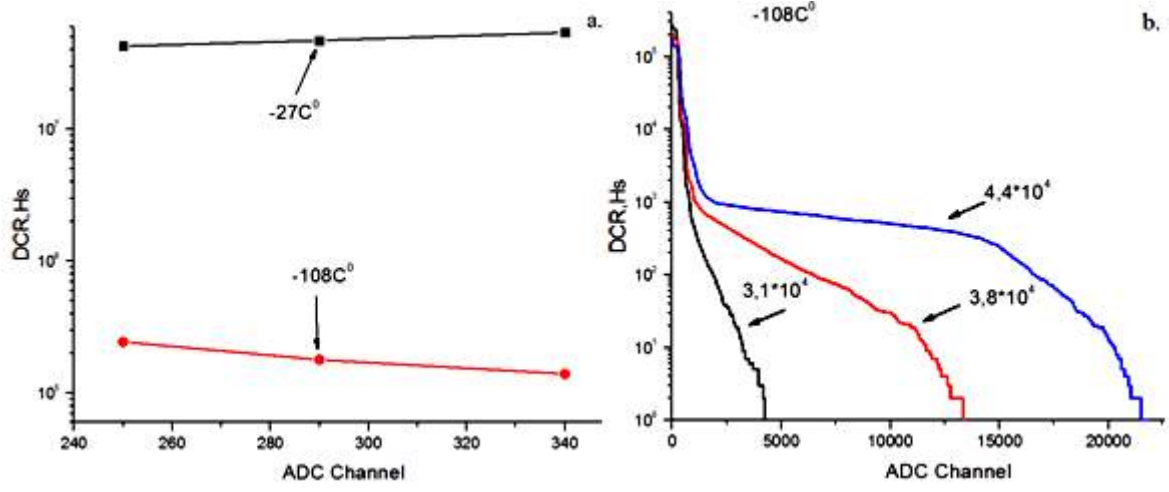


Fig. 4. The dependence of the dark count of MAPD-3NK on the gain.

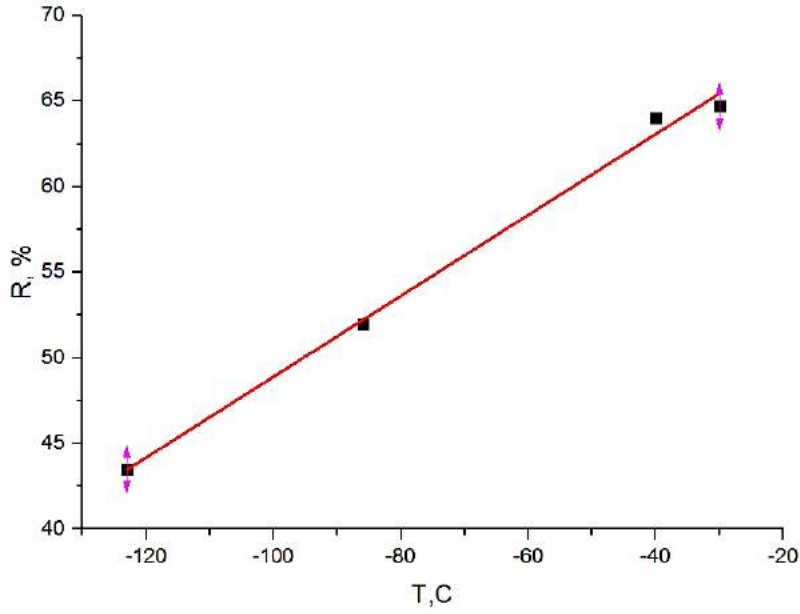


Fig. 5. The dependence of the amplitude resolution on temperature.

### 3. RESULTS

It was experimentally determined that the breakdown voltage of photodiodes MAPD-3NK has a dependence of  $58 \pm 3 \text{ mV}/^\circ\text{C}$  and decreases linearly with decreasing temperature. DC in photodiodes with a temperature difference of  $-81^\circ\text{C}$ , improves 169 times. At low temperatures ( $-70^\circ\text{C}$  and below), the appearance of dark count is mainly due to the effect of

afterpulses. It was also shown that the difference between the amplitude resolution corresponding to single photoelectron improves to 32%, with a temperature difference of  $-93^\circ\text{C}$ . In other words, the results show that MAPD-3NK photodiodes can be successfully used in low-temperature experiments.

- [1] P.Ade et al. Planck 2013 results. XVI. Cosmological parameters. arXiv:1303.5076.
- [2] Laura Baudis. WIMP dark matter direct-detection searches in noble gases, Physics of the Dark Universe, vol. 4, p. 50-59, 2014.
- [3] L. Baudis, G. Kessler, P. Klos, R. Lang, J.Menendez, et al. Signatures of dark matter scattering inelastically off nuclei, Phys.Rev.

- D88(2013)115014.arXiv:1309.0825, <http://dx.doi.org/10.1103/PhysRevD.88.115014>
- [4] A. de Bellefon, I. Berkes et al. Dark matter search with a low temperature sapphire bolometer, Astroparticle Phys., vol. 6, p.35-43, 1996.
- [5] N.J.C. Spooner. Tests on low temperature calorimetric detectors for dark matter

- experiments, Phys. Lett., B, vol.245, No.2, 1990, p. 265-270.
- [6] Z.Sadygov, O.Olshevski, I.Chirikov et al. Three advanced designs of micropixel avalanche photodiodes: Their present status, maximum possibilities and limitations, Nucl. Instrum. Meth. A, v. 567, p. 70-73, 2006.
- [7] A.Ivashkin, F.Akhmadov, R.Asfandiyarov, A.Bravar, A.Blondel, W.Dominik, Z.Fodor, M.Gazdzicki, M.Golubeva, F.Guber, A.Hasler, A.Korzenev, S.Kuleshov, A.Kurepin. Hadron calorimeter with MAPD readout in the NA61/SHINE experiment, arXiv preprint arXiv:1205.4864.
- [8] F.Ahmadov, G.Ahmadov, E.Guliyev, R.Madatov, A.Sadigov, Z.Sadygov, S.Suleymanov. New gamma detector modules based on micropixel avalanche photodiode, Journal of Instrumentation, V12, N01, p. C01003, 2017.

*Received: 05.07.2019*

# BOUNDARY EFFECTS IN POLYMER COMPOSITES - POWERED CERAMICS

Z.A. DADASHOV

G.M. Abdullayev Institute of Physics of Azerbaijan NAS  
131, H. Javid ave., Baku, Azerbaijan, AZ1143

The paper presents the results of studies of the piezoelectric properties of composites based on multicomponent piezoceramics and fluorine-containing polar polymers. In this regard, the role of interfacial charges in the formation of the piezoelectric effect is considered.

**Keywords:** polymer composites, injection, multicomponent ceramic, boundary effects

**PACS:**83.85.Hf, 82.35.Np, 83.80.Tc.

## 1. INTRODUCTION

Analysis of numerous works on piezoelectric and pyroelectric materials shows that the polymer matrix of these disperse systems is the active phase and determines the magnitude of the macroscopic parameters of the marked composites. The piezo-, pyroelectric properties of these heterogeneous systems are due to the combined action of the boundary, interfacial, injection, and electret properties of individual phases, in particular, the polymer [1-4].

The aim of the work is to study the interphase phenomena and boundary polarization effects under the conditions of simultaneous exposure to a strong electric field ( $E_p$ ) and temperature ( $T_n$ ) in polymer composites.

## 2. EXPERIMENTAL TECHNIQUE

As a research method, we used spectra of thermally activated spectroscopy (TSD).

Multicomponent ceramics of the lead zirconate titanate (PZT-19) family were used as the piezoelectric phase. Composite samples were obtained by hot pressing in the melting range of the polymer matrix [1]. The dielectric parameters of the composites are measured using an E7-20 voltmeter.

## 3. EXPERIMENTAL RESULTS AND DISCUSSION

The energy diagram of the polymer – piezoceramics boundary before (fig. 1a) and after contacting (fig. 1b) of the phases is shown in fig. 1. After contact between the polymer and piezoceramics is established, the Fermi levels  $E_f$  are equalized due to the movement of electrons from polymer. The formation of layers of space charges near the interface is accompanied by the bending of zones and is the initial stage of the formation of the Schottky barrier.

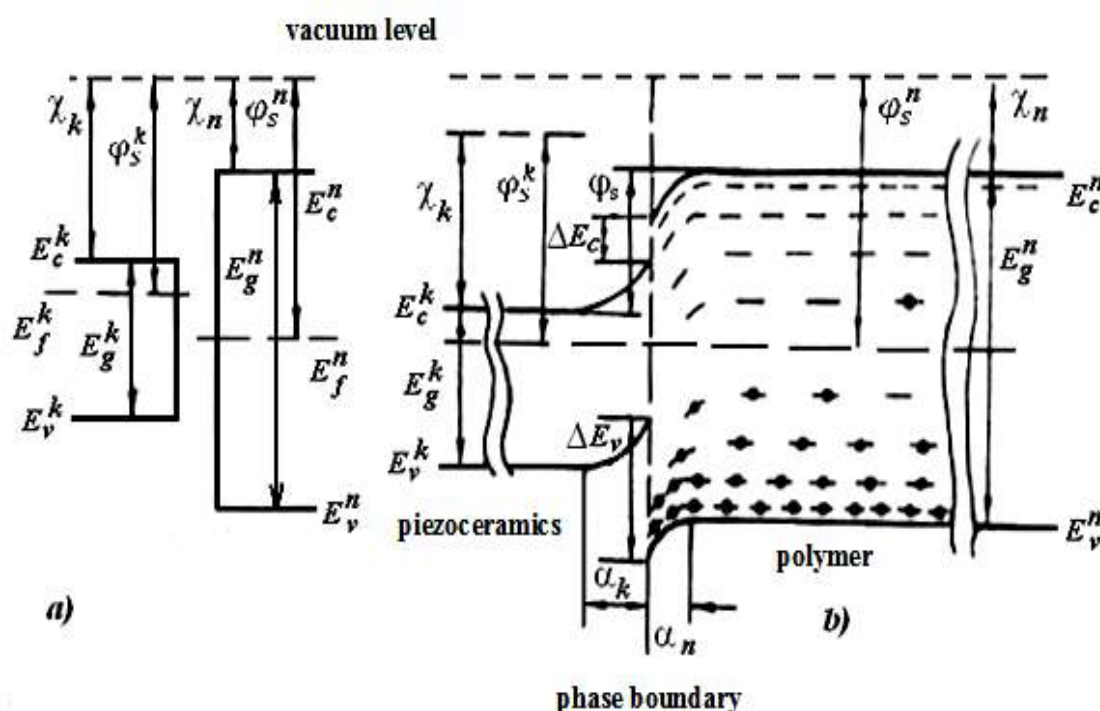


Fig.1. Energy diagram of the polymer - piezoceramics boundary before (a) and after contacting (b) phases



With the ratio of the work function of the electrons indicated in fig. 1, in the case of contact of a polymer - piezoelectric ceramics the interface passes from piezoceramics to a polymer, resulting in an excess charge on the surface of the polymer phase and, therefore, a potential barrier height

$$\varphi = \frac{e^2 n_D \alpha^2}{2 \varepsilon_{nc}}$$

and the Fermi level by the formula

$$E_F = kT \ln \frac{n_D}{N_S}$$

where  $N_S$  is the density of the filled boundary states;  $\varepsilon_{ps}$  is the dielectric constant of the transition layer;  $n_D$  is the density of donors.

It can be concluded that for  $d_{33}$  in composites it is not the electrode that is responsible  $\varphi$ , but  $\varphi$ , which is formed at the interface [4] (fig.2).

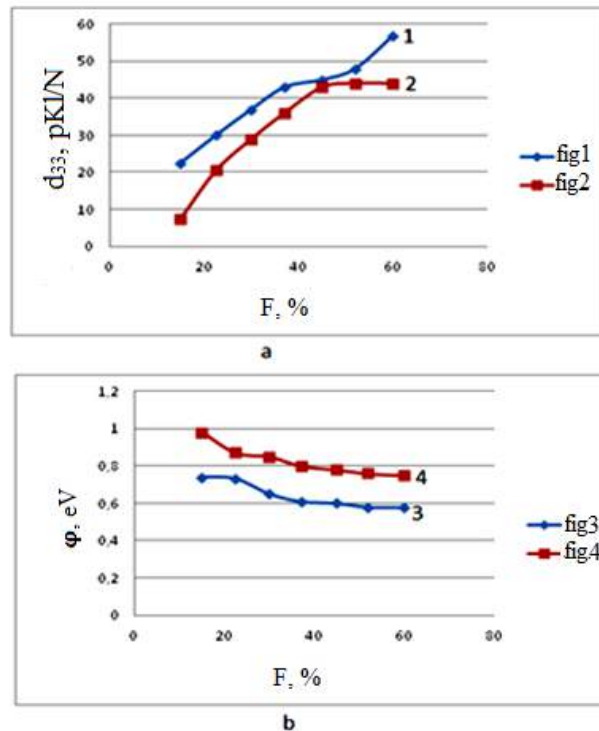


Fig.2. Dependencies of the piezomodule  $d_{33}$  (1, 2) and the potential barrier  $\varphi$  (3, 4) at the interface between the phases and the volume content ( $F$ ) of the piezophase. 1 is  $d_{33}$  for PVDF – Pb (TiZr)  $O_3$  composite; 2 is  $d_{33}$  for PVDF – Pb (TiZr)  $O_3$  composite; 3 is  $\varphi$  for composite PVDF – Pb (TiZr)  $O_3$ ; 4 is  $\varphi$  for PVDF – Pb (TiZr)  $O_3$  composite. The size of piezoparticles is 60 microns;  $E_n = 4.5$  MV / m;  $T_n = 393$  K;  $t_n = 0.5$  hour

#### 4. CONCLUSION

Dispersion of the polymer matrix by multicomponent ferroelectric particles leads to a noticeable increase in the piezomodule depending on

the volume content of the piezophase in the composite.

- 
- [1] M.A.Kurbanov. Electret, piezo, pyroelectric, varistor and posistor effects in polymer composite dielectrics: Dis. Dr. f.- M.Sciences. Baku, p. 477, 1985.
- [2] M.A.Kurbanov, Sh.M.Ahadzade, I.S.Ramazanov, Z.A.Dadashov, I.A.Farajzade. Varistor effect in highly heterogeneous polymer–ZnO systems. Semiconductor Physics and Engineering, vol. 51, no.7, p. 992-997, 2017.
- [3] E.P. Blythe, D. Bloor. Electrical properties of polymers. Per. from English- M.: Fizmatlit., p. 376, 2008.
- [4] M.K.Kerimov, M.A. Kurbanov, A.A. Bayramov, A.I.Mamedov. Matrix Active Micro and Nanocomposites Based on the Polymer, Semiconductive and Ferropiezoceramic Materials. Nanocomposites and Polymers with Analytical Methods /Book 3. edited by: John Cuppoletti, INTECH Open Access Publisher. pp. 375-404, 2011.

Received: 12.07.2019

# MAJORANA FERMIONS IN ONE- AND QUASI- ONE DIMENSIONAL INSULATOR WITH CHARGE-DENSITY WAVE

S.O. MAMMADOVA

*G.M. Abdullayev Institute of Physics of Azerbaijan NAS*

*131, H. Javid ave., Baku, AZ 1143*

*e-mail: seide.memmedova@physics.science.az*

Majorana fermions can be created in strongly anisotropic crystals with wave-charge density (Peierls instability) in the presence of external magnetic field. Many quasi-one dimensional crystals display Peierls phase transition due to doubling of the crystal unit cell, when a metallic phase of the crystal transforms to an insulator. In this case time reversal symmetry and the particle-hole symmetry are preserved. The formation of the topological phase of crystal is realized in the presence of the strong spin-orbit interaction and external magnetic field in the structure. The interplay between the magnetic field, spin-orbit interaction constants, and the charge density wave gap seems to support Majorana bound states under appropriate values of the external parameters.

**Keywords:** Majorana fermions, charge density wave, spin-orbit interaction, magnetic field

**PACS:** 75.70.Tj, 71.70.Ej, 72.15.Nj, 85.75.-d

## 1. INTRODUCTION

Although the high-speed computers operating on the base of quantum principles were very attractive up to last thirty years but inaccessible due to the low-level technology, nowadays theoretical and experimental knowledge supports a reality of realization of the quantum computer, and this scientific branch is an extremely perspective one of the modern sciences. According to the law proposed by one of the founders of Intel, Gordon E. Moore, the number of the transistors in the integral circuit of the modern computers increases twice every year and at present, this process seems to be going to saturation [1,2]. According to this law, which indicates the future of the computer technology, in a recent 10-15 years, there should be started the period that will be based on the quantum computing. Quantum computers are based on principles of the quantum physics that allows to increase the speed of the computations. Due to that, the energy of the carriers of the information in the quantum transistors –quasi-particles, is less than 1 eV, even any small local excitations can break the information through the transition of quasi-particles to another state. Therefore, researchers try to decode quantum information non-locally that leads to the study of topologically protected qubits.

The recently, charge density waves, observed experimentally [3,4,5] in atomic wires Au, In, Ge, have been obtained self-assembly of Si (553), Si (557), Ge (001) on vicinal surfaces. The latest development of the technology makes it possible to obtain wires nesting of single metallic atoms [2] on the dielectric substrate with an atomic width using a scanning tunneling microscope. In these quasi- one-dimensional structures distances between vicinal wires are 1.5-2 nanometers. The angle-resolved photoemission spectroscopy measurements of the

electron dispersion show that these structures are one-dimensional with weak coupling between the wires. Modeling the quasi-one-dimensional structure according to the strong coupling approximation and utilizing characteristics of the Fermi contour getting in the experiment, it was obtained the value  $t_{||}/t_{\perp} \sim 60$  for [6] ratio of the longitudinal and transverse overlap integrals. This fact allows to neglect the coupling between the wires in structures of Au /Si (557), Au /Si (553) and Au /Ge (001). In all of these structures, Peierls instability and formation of charge density wave are observed at higher temperatures,  $30K < T < 270K$ .

Thus, in this paper I suggest that the formation of qubit can be obtained in a strong spin-orbit interaction material with the charge density wave of dielectric phase. The Majorana fermions are emerged only at the edges of a single wire by changing the external magnetic field in the quasi-one dimensional structure with a strong spin-orbit interaction.

## 2. DENSITY-WAVE ORDERING IN THE PRESENCE OF RASHBA AND DRESSELHAUS SPIN-ORBIT INTERACTIONS

The model considered here is essentially a 1D Hubbard model in the presence of both Rashba and Dresselhaus spin-orbit interactions and a Zeeman magnetic field. Hamiltonian of the system is given by the following form:

$$\hat{H} = \hat{H}_0 + \hat{H}_{int} \quad (1)$$

where  $\hat{H}_0$  and  $\hat{H}_{int}$  are the noninteracting part of the Hamiltonian and the part expressing the correlation between electrons, correspondingly.  $\hat{H}_0$  reads in momentum space as:

$$\hat{H}_0 = \sum_{0 < k < \frac{G}{2}} \sum_{\sigma, \sigma'} \left\{ \xi_k c_{k, \sigma}^+ c_{k, \sigma'} \delta_{\sigma, \sigma'} + \omega_z c_{k, \sigma}^+ (\sigma_x)_{\sigma, \sigma'} c_{k, \sigma'} + \alpha \sin(kd) c_{k, \sigma}^+ (\sigma_z)_{\sigma, \sigma'} c_{k, \sigma'} + \beta \sin(kd) c_{k, \sigma}^+ (\sigma_y)_{\sigma, \sigma'} c_{k, \sigma'} + (k \leftrightarrow k - \frac{G}{2}) \right\} \quad (2)$$

where  $\alpha$  and  $\beta$  are constants of the Rashba and Dresselhaus spin-orbit interactions,  $\omega_z = \frac{g\hbar\mu_B B}{2}$  is Zeeman energy of a magnetic field  $B$ ,  $\xi_k = -2t \cos k - \mu$  with  $\epsilon_k = -2t \cos(kd)$ , and  $\mu$  is

the Fermi energy.  $G = \frac{2\pi}{d}$  is the reciprocal lattice vector with  $d$  being the unit cell size. The interaction term  $\hat{H}_{int}$  in the Hamiltonian is written as:

$$\hat{H}_{int} = \frac{1}{2N} \sum_{0 < q < G} \sum_{\sigma} \{ \sum_{k,k'} U(k, k', q) c_{k+q,\sigma}^+ c_{k,\sigma} c_{k'-q,-\sigma}^+ c_{k',-\sigma} + \sum_{n,n'} U(n, n', q) c_{n,\sigma}^+ c_{n+q-G,\sigma} c_{n',-\sigma}^+ c_{n'-q+G,-\sigma} \} \quad (3)$$

where  $k \in (-\frac{G}{2}, \frac{G}{2} - q)$ ,  $k' \in (q - \frac{G}{2}, \frac{G}{2})$  and  $n \in (\frac{G}{2} - q, \frac{G}{2})$ ,  $n' \in (-\frac{G}{2}, q - \frac{G}{2})$ .  $U$  is a strength of the Hubbard interaction and  $N$  is the number of lattice sites.

The pole of the single particle Green's function determines the energy spectrum of quasi-particle excitations:

$$G^{-1}(E, k) = E - \hat{\mathcal{H}} \quad (4)$$

For charge density wave state, this energy is found as solution to the following matrix:

$$\begin{vmatrix} E - \xi_k - \alpha \sin k & -\Delta & -\omega_z - \beta \sin k & 0 \\ \Delta^* & E - \xi_{k-G/2} - \alpha \sin(k - G/2) & 0 & -\omega_z - \beta \sin(k - G/2) \\ -\omega_z + \beta \sin k & 0 & E - \xi_k + \alpha \sin k & -\Delta \\ 0 & -\omega_z + \beta \sin(k - G/2) & -\Delta^* & E - \xi_{k-G/2} + \alpha \sin(k - G/2) \end{vmatrix} = 0. \quad (5)$$

Expressions for the energy spectrum can be written as

$$E_{YSD}^2 = \xi_k^2 + \gamma^2 \sin^2 k + |\Delta|^2 + \omega_z^2 \pm 2\sqrt{\xi_k^2 \gamma^2 \sin^2 k + \omega_z^2 |\Delta|^2 + \xi_k^2 \omega_z^2} \quad (6)$$

where  $\gamma = \sqrt{\alpha^2 + \beta^2}$  is constant of spin-orbit coupling.

The energy spectrum at the center of the Brillouin zone for the topological charge density wave with gapped “bulk” states and zero energy end states can be written as

$$E(0) = \left| \omega_z - \sqrt{\mu_t^2 + |\Delta|^2} \right| \quad (7)$$

where  $\mu_t = -2t - \mu$ .

The gap at  $k = 0$  vanishes under this condition, with emerging Majorana fermion states at the ends of the wire, which is plotted in Fig. for the dimensionless parameters (a)  $\gamma=0.8$ ,  $\Delta=0.7$ ,  $\mu = -0.1$ ,  $\omega = \sqrt{1.7}$ ; (b)  $\gamma=0.8$ ,  $\Delta=0.7$ ,  $\mu = -0.3$ ,  $\omega = \sqrt{2.18}$ .

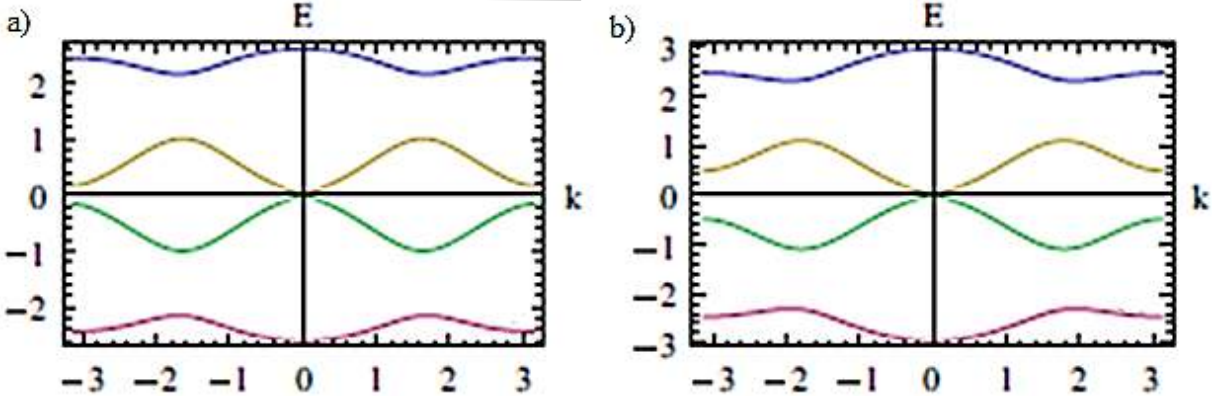


Fig.: The energy spectrum is plotted according to Eq. (6) for fixed values of  $t = 0.5$  and for the following values of the dimensionless parameters: (a)  $\gamma=0.8$ ,  $\Delta=0.7$ ,  $\mu = -0.1$ ,  $\omega = \sqrt{1.7}$ ; (b)  $\gamma=0.8$ ,  $\Delta=0.7$ ,  $\mu = -0.3$ ,  $\omega = \sqrt{2.18}$ .

### 3. CONCLUSION

This paper demonstrates that a one-dimensional lattice in a CDW phase with strong spin-orbit interactions and a Zeeman magnetic field can support Majorana modes. The basic principle here is that the quantum topological order is realized in a 1D-wire with charge-density wave in the presence of spin-orbit interactions by tuning the external Zeeman energy. I

show that for the Zeeman coupling below a critical value ( $\omega_z^2 > \mu_t^2 + |\Delta|^2$ ), the system is a nontopological charge density wave semiconductor. However, above the critical value of the Zeeman field ( $\omega_z^2 < \mu_t^2 + |\Delta|^2$ ), the lowest energy excited state is a zero-energy Majorana fermion state for topological CDW crystals.

- [1] *G.E. Moore.* “Progress in Digital Integrated Electronics”, International Electron Devices Meeting, IEEE, 1975, p.p. 11-13.
- [2] *T.C. Bartee.* “Digital computer Fundamentals”, McGraw -Hill Education Pvt Limited, 1985.
- [3] *C.Blumenstein, J.Schafer, S.Mietke, S.Meyer, A.Dollinger, M.Lochner, X.Y.Cui, L.Patthey, R.Matzdorf and R.Claessen.* Nat. Phys. 7, 776, 2011.
- [4] *I.K. Robinson, P.A. Bennett and F.J. Himpsel.* 2002, Phys. Rev. Lett. 88, 096104.
- [5] *J.N. Crain, M.D. Stiles, J.A. Stroscio and D.T.Pierce.* 2006, Phys. Rev. Lett. 96, 156801.
- [6] *P.C. Snijders and H.H. Weitering.* Rev. Mod. Phys. 82, 207, 2010.

*Received: 18.07.2019*

## THERMODYNAMIC PROPERTIES OF ERBIUM MONOTELLURIDE

I.F. MEKHDIYEVA

*Institute of Catalysis and Inorganic Chemistry of Azerbaijan NAS  
AZ-1143, H. Javid ave., 113, Baku, Azerbaijan*

The results of thermodynamic investigation of ErTe investigation by the method of electromotive force (EMF) are presented in the work. The relative partial molar functions of erbium in  $\text{ErTe}+\text{Er}_2\text{Te}_3$  two-phase region are calculated from data obtained by the method of rapid fixing of EMF. Gibb's standard free formation energy and formation enthalpy and also the standard entropy of ErTe compound are calculated based on obtained data and integral thermodynamic functions of  $\text{Er}_2\text{Te}_3$ .

**Keywords:** erbium telluride, ErTe,  $\text{Er}_2\text{Te}_3$ , EMF method, thermodynamic functions.

**PACS:** 71.20. Be, 75.10.Nr, 75.20.-g

## INTRODUCTION

Rare earth chalcogenides are among the promising materials for electronic equipment. They have a wide range of physical properties: high heat resistance, stability to sudden changes in environmental conditions, unique magnetic, optical and thermoelectric properties [1-10].

For the development of modern preparative methods and controlled synthesis of novel complex phases and materials based on them, the experimental phase diagrams and reliable thermodynamic data are required [11-14].

The Er-Te system [1, 15] is characterized by the formation of tellurides with ErTe,  $\text{Er}_2\text{Te}_3$ , and  $\text{ErTe}_3$  compositions. ErTe and  $\text{Er}_2\text{Te}_3$  compounds melt congruently at 1773 and 1486K, while  $\text{ErTe}_3$  melts with decomposition according to the peritectic reaction at 957 K. ErTe and  $\text{Er}_2\text{Te}_3$  have a cubic,  $\text{ErTe}_3$  – rhombic structure.

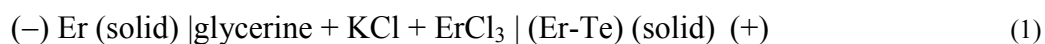
The thermodynamic properties of erbium telluride are not well understood. In modern reference books [16, 17] no thermodynamic data available on

these compounds. In [18], the standard thermodynamic functions of the formation of  $\text{Er}_2\text{Te}_3$  were determined by direct synthesis from components in a calorimetric bomb. In a later work [19], the authors calculated the standard thermodynamic functions of  $\text{Er}_2\text{Te}_3$  formation by the EMF method and showed their good agreement with the data [18]. The reference book [20] provides estimated data on the standard enthalpy of formation and entropy of ErTe and  $\text{Er}_2\text{Te}_3$ .

This work presents the results of the study of the thermodynamic properties of monotelluride erbium by the method of electromotive forces (EMF) with glycerol electrolyte. This modification of EMF method was successfully used for the thermodynamic investigations of a number binary and ternary chalcogenide system [21-25].

## EXPERIMENT AND THEIR RESULTS

For the investigations of the thermodynamic properties of ErTe compound, the concentration cells of follow type were constructed:



The alloys of Er-Te system with compositions 52 and 57 at Te% (two-phase region  $\text{ErTe}+\text{Er}_2\text{Te}_3$ ) were synthesized by ceramic method from elementary high purity erbium and tellurium and used as right electrodes (anode) in cells (1).

The synthesis is carried out in evacuated ( $10^{-2}$ Pa) silica tubes ampoules at 1000K. Later the melts are powdered, carefully mixed and pressed in tabs which are annealed at the same temperature during ~800h. The phase compositions are controlled by the XRD method.

The left electrodes (cathod) were prepared by the fixing of metallic erbium on molybdenum wire while the anodes were prepared by pressing of powdered intermediate alloys on the wire in the form of cylinder tabs of mass ~0,5g under pressure of ~0.1 GPa.

As an electrolyte, the KCl glycerin solution with the addition of  $\text{ErCl}_3$  was used. Because the presence of either moisture or oxygen in the electrolyte was inadmissible, glycerol was thoroughly dewatered and

degassed by evacuation at ~450 K over anhydrous chemically pure salts.

During EMF measurements, it was shown the non- equilibrium of cells (1). EMF values strongly decrease in measurement beginning during several hours in comparison with high initial ones (by order ~1000 mV) up to 200÷300 mV. Though later these values are reproducible ones, they aren't accepted as equilibrium ones because according to previous thermodynamic calculations they are less than predictable values in 2÷3 times. Thus and so we use the simplified variant of EMF instantaneous fixing [26], i.e. the rapid fixing of EMF values which is earlier applied by us at the thermodynamic investigation of some REE tellurides [27-29]. The essence of this method is in the fact that left electrode is in another vessel with the same electrolyte at the same temperature that the right electrodes are up to the moment of EMF measurements.

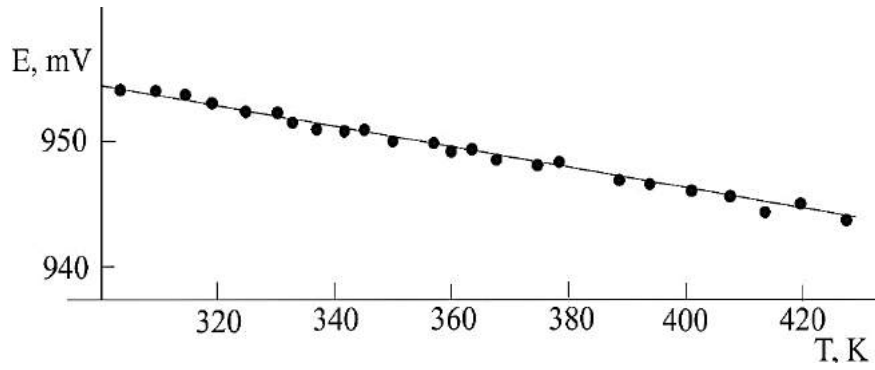


Fig. Temperature dependence of EMF measurements of cell (1) alloys of the ErTe-Er<sub>2</sub>Te<sub>3</sub> subsystem

EMF measurement is carried out in the moment of left electrode introduction into the electrochemical system with the right electrode and the maximum value of EMF is fixed. EMF was measured using the high-impedance digital voltmeter B7-34A. Most measurements were performed when heating and cooling the cell in steps up to 10°. Chromel- alumel thermocouple couples and mercury thermometers with an accuracy of about ±0.5° were used to measure the temperature of the electrochemical cell. The chromel- alumel thermocouples were preliminarily calibrated in the temperature interval 300-510 K using elemental Ga, S, In, and Sn as reference materials.

The measurement results are given in Figure and in Table. As can be seen, the temperature dependence of the EMF is almost linear. The obtained experimental data were processed using the

"Microsoft Office Excel 2003" computer program using the least-squares method. The steps of the calculations are given in the Table. A linear equation is obtained, presented in the form recommended in [30, 31]

$$E = a + bT \pm t \left[ \frac{S_E^2}{n} + \frac{S_b^2(T - \bar{T})^2}{\sum (T_i - \bar{T})^2} \right]^{\frac{1}{2}}$$

Here,  $n$  - is the number of pairs of  $E$  and  $T$  values;  $S_E$  and  $S_b$  - are the dispersions of separate measurements of EMF and coefficient  $b$ , respectively;  $\bar{T}$  - average absolute temperature,  $t$  - is Student's test. At the confidence level of 95% and  $n \geq 20$ , the Student's coefficient is  $k \leq 2$ .

From the obtained relation

$$E, \text{mV} = 979.73 - 0.0838T \pm 2 \left[ \frac{0.26}{24} + 8.2 \cdot 10^{-6} (T - 362.84)^2 \right]^{1/2} \quad (2)$$

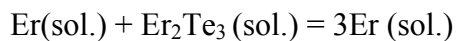
the relative partial thermodynamic functions of Er in ErTe are calculated by known thermodynamic expressions:

$$\Delta \bar{G}_{\text{Er}} = -276.36 \pm 0.12 \text{ kJ} \cdot \text{mol}^{-1} \quad (3)$$

$$\Delta \bar{H}_{\text{Er}} = -283.59 \pm 0.60 \text{ kJ} \cdot \text{mol}^{-1} \quad (4)$$

$$\Delta \bar{S}_{\text{Er}} = -24.25 \pm 0.66 \text{ J} \cdot \text{mol}^{-1} \cdot \text{K}^{-1} \quad (5)$$

These partial molar data are thermodynamic functions of potential forming reaction:



According to this relation the standard thermodynamic formation functions of ErTe were calculated using the relation

$$\Delta_f Z^0(\text{ErTe}) = \frac{1}{3} [\Delta \bar{Z}_{\text{Er}} + \Delta_f Z^0(\text{Er}_2\text{Te}_3)] \quad (6)$$

( $Z \equiv G, H$ ) and standard entropy using relations

$$S^0(\text{ErTe}) = \frac{1}{3} [\Delta \bar{S}_{\text{Er}} + S^0(\text{Er}) + S^0(\text{Er}_2\text{Te}_3)] \quad (7)$$

According to these equations, the calculations require information on the standard thermodynamic functions of the formation and standard entropy of Er<sub>2</sub>Te<sub>3</sub>, as well as the standard entropy of elementary erbium.

We use the data of [19] on the standard heat of formation of Er<sub>2</sub>Te<sub>3</sub>, as well as the values of the standard entropies of erbium ( $73.14 \pm 0.63 \text{ kJ} \cdot \text{mol}^{-1}$ ) and tellurium ( $49.50 \pm 0.21 \text{ kJ} \cdot \text{mol}^{-1}$ ) [17] the standard Gibbs free energy of the formation of Er<sub>2</sub>Te<sub>3</sub> was calculated and a mutually consistent set of thermodynamic data was obtained for this compound:

$$\Delta_f G^0(298\text{K}) = -797.4 \pm 1.1 \text{ kJ} \cdot \text{mol}^{-1}$$

$$\Delta_f H^0(298\text{K}) = -822.2 \pm 16.7 \text{ kJ} \cdot \text{mol}^{-1}$$

$$S^0(298\text{K}) = -83.7 \pm 27.2 \text{ J} \cdot \text{mol}^{-1} \cdot \text{K}^{-1}$$



# **THERMODYNAMIC PROPERTIES OF ERBIUM MONOTELLURIDE**

These data were used for calculations by relations (6) and (7).

As a result of the calculations, the following values of the standard integral thermodynamic functions of ErTe were obtained:

$$\Delta_f G^0(298K) = -357.0 \pm 0.5 \text{ kJ}\cdot\text{mol}^{-1}$$

$$\Delta_f H^0(298K) = -379.6 \pm 6.0 \text{ kJ}\cdot\text{mol}^{-1}$$

$$S^0(298K) = 86.7 \pm 9.3 \text{ J}\cdot\text{mol}^{-1}\cdot\text{K}^{-1}$$

In all cases, the estimated standard deviations were calculated by the accumulation of errors.

Table.

Experimentally obtained data for temperature and EMF as well as data associated with the calculation steps for the samples with compositions 52 and 57 at.% of Er-Te system

$T_i, K$	$E_i, mV$	$T_i - \bar{T}$	$E_i(T_i - \bar{T})$	$(T_i - \bar{T})^2$	$\bar{E}$	$E_i - \bar{E}$	$(E_i - \bar{E})^2$
303,5	954,3	-59,34	-56629,75	3521,43	954,30	0,00	0,00
310,8	953,7	-52,04	-49632,14	2708,34	953,69	0,01	0,00
316,5	953,3	-46,34	-44177,51	2147,55	953,21	0,09	0,01
320,2	953,1	-42,64	-40641,77	1818,31	952,90	0,20	0,04
326,2	952,8	-36,64	-34912,18	1342,61	952,40	0,40	0,16
333,4	952,1	-29,44	-28031,41	866,81	951,80	0,30	0,09
334,3	951,8	-28,54	-27165,96	814,63	951,72	0,08	0,01
338,5	951,3	-24,34	-23156,23	592,52	951,37	-0,07	0,00
343,2	951,7	-19,64	-18692,97	385,80	950,97	0,73	0,53
347,6	950,6	-15,24	-14488,73	232,31	950,61	-0,01	0,00
353,3	950,8	-9,54	-9072,22	91,04	950,13	0,67	0,45
358,5	949,4	-4,34	-4121,98	18,85	949,69	-0,29	0,09
362,7	948,1	-0,14	-134,31	0,02	949,34	-1,24	1,54
365,2	948,6	2,36	2237,11	5,56	949,13	-0,53	0,28
369,4	948,2	6,56	6218,61	43,01	948,78	-0,58	0,34
376,5	947,3	13,66	12938,54	186,55	948,18	-0,88	0,78
381,1	947,5	18,26	17299,77	333,37	947,80	-0,30	0,09
390,6	946,7	27,76	26278,81	770,53	947,00	-0,30	0,09
395,3	946,8	32,46	30731,55	1053,54	946,61	0,19	0,04
401,8	946,1	38,96	36858,48	1517,75	946,07	0,03	0,00
408,3	946	45,46	43003,58	2066,46	945,52	0,48	0,23
417,2	945,8	54,36	51412,11	2954,83	944,77	1,03	1,05
424,6	943,7	61,76	58281,34	3814,09	944,15	-0,45	0,21
429,5	944,2	66,66	62938,80	4443,33	943,74	0,46	0,21
$\bar{T}$ =362,84	$\bar{E}$ =949,3292		$\sum E(T_i - \bar{T})$ =-2658,45	$\sum (T_i - \bar{T})^2$ =31729,24			$\sum (E_i - \bar{E})^2$ =6,23

## **CONCLUSION**

The fast fixation method was used to study the Er-Te system in the two-phase region ErTe Er<sub>2</sub>Te<sub>3</sub> in the temperature range 300-430 K. Relative partial

molar functions of erbium in alloys were calculated, based on which a mutually consistent complex of standard thermodynamic formation functions and standard entropy of the ErTe compound was obtained for the first time.

- |   |   |
|---|---|
| <p>[1] E.I. Yarembash, A.A. Eliseyev The chalcogenides of rare-earth elements, M.: Nauka, 1975.</p> <p>[2] O.V. Andreev, V.G. Bamburov, L.N. Monina, Razumkova, A.V. Ruseykina, O.Yu. Mitroshin, V.O. Andreev. Phase equilibria in sulfide systems of 3d-, 4f-elementov. Ekaterinburg: RIO URO RAN, 2015, 312s.</p> <p>[3] A.R. Jha. Rare Earth Materials: Properties and Applications, CRC Press, United States, 2014.</p> | <p>[4] S. Bangarigadu-Sanasy, C.R. Sankar, P. Schlender, H. Kleinke. Thermoelectric properties of Tl<sub>10-x</sub>Ln<sub>x</sub>Te<sub>6</sub>, with Ln =Ce, Pr, Nd, Sm, Gd, Tb, Dy, Ho and Er, and 0.25&lt;x&lt;1.32. J. Alloys Compd., 2013, v. 549, pp.126–134.</p> <p>[5] S.Bangarigadu-Sanasy, C.R.Sankar, P.A.Dube. Magnetic properties of Tl<sub>9</sub>LnTe<sub>6</sub>, Ln =Ce, Pr, Tb and Sm. J.Alloys.Comp. 2014, v.589, p.389–392.</p> |
|---|---|

- [6] A.S. Verma Electronic and Optical Properties of Rare-earth Chalcogenides and Pnictides African Phys.Rev., 2009, vol. 3, pp. 11-20 (in Russian).
- [7] A.A.Sinchenko, P.D.Grigoriev, P.Monceau, P. Lejay, V.N. Zverev. Slow Oscillations of In-plane Magnetoresistance in Strongly Anisotropic Quasi-Two-Dimensional Rare-Earth Tritellurides. J Low Temp Phys, 2016, v. 185, p. 657.
- [8] D. Cheikh, B.E. Hogan, T. Vo, P von Allmen, K. Lee, D.M. Sniadak, A. Zevalkink, B.S. Dunn, J.-P. Fleurial, S.K. Bux. Praseodymium Telluride: A High Temperature, High ZT Thermoelectric Material. Joule, 2018, vol. 2, pp.698–709.
- [9] I.P. Muthuselvam, R. Nehru, K.R. Babu, K. Saranya, S.N. Kaul, S-M. Chen, W-T. Chen, Y. Liu, G-Y Guo, F.Xiu, R. Sankar. Gd<sub>2</sub>Te<sub>3</sub>: an antiferromagnetic semimetal. J. Physics: Condensed Matter, 2019, v.31, no.28, p. 285802.
- [10] X.Z. Zhou., K.H.L. Zhng, J. Xiong, J.H. Park, J.H. Dicenson, W.D. He Size- and dimensionality dependent optical, magnetic and magneto-optical properties of binary europium-based nanocrystals: EuX (X=O, S, Se, Te). Nanotechnology, 2016, v. 27, no.19, p. 192001.
- [11] M.B. Babanly, E.V. Chulkov, Z.S. Aliev, A.V. Shevel'kov, and I.R. Amiraslanov. Phase diagrams in materials science of topological insulators based on metal chalcogenides. Russ. J. Inorg. Chem., 2017, vol. 62, no. 13, p. 1703–1729.
- [12] V. N. Tomashyk. Multinary Alloys Based on III-V Semiconductors. 2016. RC Press.
- [13] S.Z. Imamaliyeva, D.M. Babanly, D.B. Tagiev, and M.B. Babanly. Physicochemical Aspects of Development of Multicomponent Chalcogenide Phases Having the Tl<sub>5</sub>Te<sub>3</sub> Structure: A Review. Russ. J. Inorg. Chem., 2018, vol. 63, no. 13, p.1703–1727.
- [14] S.Z. Imamaliyeva. Phase diagrams in the development of thallium-REE tellurides with Tl<sub>5</sub>Te<sub>3</sub> structure and multicomponent phases based on them. Condensed matter and interphases, 2018, vol.20, no.3, pp. 332-347.
- [15] T.B. Massalski. Binary alloys phase diagrams, second edition. ASM International, Materials park, Ohio, 1990, v.2, p.1163-1166.
- [16] O. Kubaschewski, C.B. Alcock. P. J. Spenser Materials Thermochemistry. Pergamon Press, 1993, p. 350.
- [17] V.S. Yunqman. The database of substance technical constants. Electron version edited by 2006, <http://www.chem.msu.su/cgi-bin/tkv> (in Russian).
- [18] K.A. Sharifov, Z.Sh. Karaev, T.Kh. Azizov. Standard Enthalpy of Formation of Er<sub>2</sub>Te<sub>3</sub>, La<sub>2</sub>Te<sub>3</sub>, In<sub>2</sub>Te<sub>3</sub>, and LaInTe<sub>3</sub>, Izv Akad. Nauk SSSR, Neorg. Mater., 1967, vol. 3, no.4, p.719–720.
- [19] V.P. Vasiliev, V.I. Goryacheva, Y.I. Gerasimov, T.S. Lazareva. Investigation of the phase equilibrium and thermodynamic properties of solid alloys of erbium with tellurium. Bulletin of Moscow. University. 1980. Ser. 2. Chim., v.21, No.4, pp. 339-345.
- [20] Gmelin handbook of inorganic chemistry, 8<sup>th</sup> edition, Sc, Y, La-Lu Rare Earth Elements. Part C10: Compounds with Te, Po. (Chief Ed. Bergmann H.) Springer-Verlag, Berlin, Heidelberg, New York, Tokyo, 1987, p. 362.
- [21] D.M.Babanly, L.F. Mashadiyeva, M.B. Babanly. The Tl–I Phase Diagram Revisited and the Thermodynamic Properties of Thallium Iodides. Inorg.Mater., 2017, vol. 53, no.5, p.519–524.
- [22] D.M. Babanly, G.M. Velieva, S.Z. Imamaliyeva, M.B. Babanly. Thermodynamic Functions of Arsenic Selenides. Russ.J.Phys. Chem. A, 2017, V. 91, No. 7, pp. 1170–1173.
- [23] Z.S. Aliev, S.S. Musayeva, F.Y. Jafarli, I.R.Amiraslanov, A.V.Shevelkov, M.B. Babanly. The phase equilibria in the Bi–S–I ternary system and thermodynamic properties of the BiSI and Bi<sub>19</sub>S<sub>27</sub>I<sub>3</sub> ternary compounds. J.Alloys. Compd., 2014, v.610, pp.522-528.
- [24] D.M. Babanly, I.M. Babanly, S.Z. Imamaliyeva, V.A. Gasimov, A.V. Shevelkov. Phase equilibria in the Tl–TlI–Te system and thermodynamic properties of the Tl<sub>5</sub>Te<sub>3</sub>–xI<sub>x</sub> solid solution. J.Alloys. Compd., 2014, v.590, pp. 68–74.
- [25] D.M. Babanly, M.B. Babanly. Phase Equilibria in the Tl–TlBr–Te System and Thermodynamic Properties of the Compound Tl<sub>5</sub>Te<sub>2</sub>Br. Russ J. Inorg. Chem., 2010, v. 55, no.10, p. 1620–1629.
- [26] M.B.Babanly, Yu.A. Ysibov. Electrochemical methods in thermodynamics of inorganic substances, Baku. ELM. 2011, p. 306. (in Russian)
- [27] M.B. Babanly, S.Z. Imamaliyeva, G.I. Ibadova. Vestnik BSU, series of physicomath. sciences, 2009, no. 4, pp. 5-9.
- [28] S.Z.Imamaliyeva, Z.S. Aliev, M.A. Maxmudova, M.B. Babanli, A.S. Abbasov. Thermodynamic properties of ytterbium telluride. Chemical Problems, 2010, no.3, pp. 453-456.
- [29] S.Z. Imamaliyeva, T.M. Gasanly, M.A. Mahmudova, F.M. Sadygov. Thermodynamic properties of GdTe compound. Physics, 2017, vol. XXIII, no. 4, pp.19-21.
- [30] A.N. Kornilov, L.B. Stepina, B.A. Sokolov. Journ. fiz. ximii, 1972, t. 46, № 11, s. 2974-2979. (in Russian).
- [31] A.G.Morachevskiy, G.F.Voronin, V.A.Geyderix, Kuchenok. Electrochemical methods of investigation in thermodynamics of metallic systems ICK. «Akademknika», 2003, p. 334 (in Russian).

Received:02.09.2019

# THERMODYNAMIC STUDY OF $\text{Cu}_2\text{SnSe}_3$ BY EMF METHOD WITH SOLID ELECTROLYTE $\text{Cu}_4\text{RbCl}_3\text{I}_2$

I.J. ALVERDIYEV

*Ganja State University,*

*187, H. Aliyev ave., Az-1148, Ganja, Azerbaijan*

By measuring the EMF of the concentration cells with solid  $\text{Cu}^+$  conductive electrolyte  $\text{Cu}_4\text{RbCl}_3\text{I}_2$ , the thermodynamic properties of the  $\text{Cu}_2\text{SnSe}_3$  compound, which is of great interest as a potential environmentally friendly thermoelectric, were studied. The partial molar functions of copper in the alloys, as well as the standard thermodynamic formation functions and the standard entropy of this compound, are calculated from the EMF measurements.

**Keywords:** EMF method, solid electrolyte,  $\text{Cu}_2\text{SnSe}_3$ , thermodynamic functions.

**PACS:** 71.20.Be, 75.10.Nr, 75.20.-g

## 1. INTRODUCTION

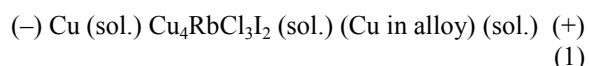
Copper containing complex chalcogenides refer to high-value functional materials. Many of them exhibit thermoelectric, photoelectric, optical, magnetic, etc. properties [1–5]. Furthermore, some of them exhibit ionic conduction with respect to  $\text{Cu}^+$  cations and can be used as electrochemical sensors, materials of electrodes, solid-state fuel cells, supercapacitors, electrochromic visualizers, etc. [6–10].

In recent years, the  $\text{Cu}_2\text{SnSe}_3$  compound, as well as phases and composites based on it, have been intensively studied as potential environmentally friendly thermoelectric and photoelectric materials [11–17]. The thermodynamic properties of this compound have hardly been studied. The work [18] presents the results obtained by measuring the EMF of concentration relative to tin chains with liquid electrolyte.

This paper presents the results of a study of the thermodynamic properties of this compound by EMF with solid  $\text{Cu}^+$  conductive electrolyte  $\text{Cu}_4\text{RbCl}_3\text{I}_2$ . This modification of the EMF method is successfully used for the thermodynamic study of complex copper-based chalcogenides [19–26]. It was shown [23, 24] that cation-conducting electrolytes can be successfully used in thermodynamic investigating copper-containing ternary systems by the EMF method even when they contain elements less noble than copper.

## 2. EXPERIMENTAL PART

For experiments, we composed concentration cells of the type



The right electrodes were equilibrium alloys from the phase region  $\text{Cu}_2\text{SnSe}_3$ - $\text{SnSe}_2$ -Se. The synthesis was carried out by fusing the elementary components with a purity of at least 99.999 % in stoichiometric ratios in quartz tubes evacuated to  $\sim 10^{-2}$  Pa and sealed. Then based on phase diagram data [5], they were subjected to stepwise homogenizing annealing at 800 K (500 h) and 450 K (300 h) followed by slow cooling to room temperature in order to reach the equilibrium state.

The right electrodes were prepared by pressing the powdered annealed alloys into pellets with a diameter of  $\sim 0.8$  cm and a thickness of 0.5 cm. A high-purity copper plate with a diameter of  $\sim 1$  cm and a thickness of 0.1 cm was used as the left electrode.

The  $\text{Cu}_4\text{RbCl}_3\text{I}_2$  solid electrolyte was synthesized by the procedure described in [19] by fusing stoichiometric amounts of chemically pure anhydrous  $\text{CuCl}$ ,  $\text{CuI}$  and  $\text{RbCl}$  in an evacuated ( $\sim 10^{-2}$  Pa) quartz tube at 900 K followed by cooling to 450 K and homogenizing annealing at this temperature for 100 h. Pellets with a thickness of  $\sim 0.4$  cm were cut from the obtained cylindrical ingot with a diameter of  $\sim 0.8$  cm, which were used as a solid electrolyte in cells (1).

The design of the electrochemical cell and the method of its assembly were described in [18, 19]. The EMF was measured with a high-resistance B7-34A digital voltmeter in the temperature range 300–450 K. In this temperature range, the alloys under study were in a solid-state, and the compositions of the equilibrium phases were almost independent of temperature [5]. The first equilibrium EMF values were obtained after the electrochemical cell was kept at  $\sim 400$  K for 40 h, and subsequent values were obtained every 3 or 4 h after a certain temperature was reached. In repeated measurements at a given temperature, the EMF values differed from each other by no more than 0.5 mV irrespective of the direction of temperature variation. During the measurements, all the necessary measures were taken [18, 27] to ensure reversibility of cells (1).

## 3. RESULTS AND DISCUSSION

An analysis of the temperature dependences of EMF (fig.) showed that they were almost linear for all the samples under study. Therefore, the results of the EMF measurements were processed by using Microsoft Excel computer program in an approximation of their linear temperature dependence by the least-squares method, and linear equation of the following type was obtained [27]:

$$E = a + bT \pm t \left[ \frac{S_E^2}{n} + S_b^2(T - \bar{T})^2 \right]^{\frac{1}{2}} \quad (2)$$

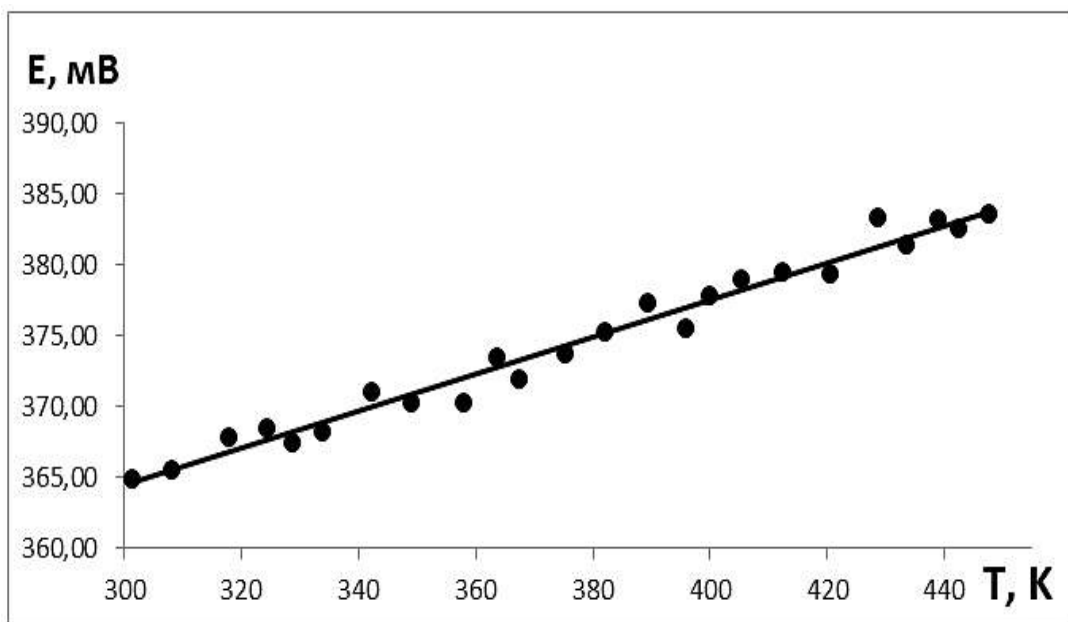


Fig. Temperature dependences of EMF for the alloys from three-phase area  $\text{Cu}_2\text{SnSe}_3\text{-SnSe}_2\text{-Se}$  at 300-450 K.

where  $n$  is the number of pairs of the  $E$  and  $T$  values;  $S_E$  and  $S_b$  - are the dispersions of the individual measurements of EMF and  $b$  coefficient, respectively;  $\bar{t}$  is the average absolute temperature, and  $t$  is the Student criterion. At a confidence level of 95% and the number of experimental points  $n \geq 20$ , the Student criterion is  $t \leq 2$ .

The experimental data of  $T_i$  and  $E_i$  and steps of calculation are presented in table 1. Follow equation is received

$$E, \text{ mV} = 325,34 + 0,1305T \pm 20,8624 + 1,81 \cdot 10^{-5}(T-377,7)212 \quad (3)$$

The relative partial thermodynamic functions of copper at 298 K in  $\text{Cu}_2\text{SnSe}_3\text{-SnSe}_2\text{-Se}$  phase area were calculated from the obtained equation (3) of the temperature dependences of EMF by the equations

$$\Delta \bar{G}_{\text{Cu}} = -zFE \quad (4)$$

$$\Delta \bar{H}_{\text{Cu}} = -zF \left[ E + T \left( \frac{\partial E}{\partial T} \right)_p \right] = -zFa \quad (5)$$

$$\Delta \bar{S}_{\text{Cu}} = zF \left( \frac{\partial E}{\partial T} \right)_p = zFb \quad (6)$$

where  $z$  is the charge on the current-forming  $\text{Cu}^+$  cation,  $F$  is the Faraday number, and  $a$  and  $b$  are the constants in the equation  $E = a + bT$ .

And the following values are received

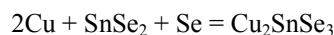
$$\Delta \bar{G}_{\text{Cu}} = -35,15 \pm 0,07 \text{ kJ} \cdot \text{mol}^{-1}$$

$$\Delta \bar{H}_{\text{Cu}} = -31,39 \pm 0,31 \text{ kJ} \cdot \text{mol}^{-1}$$

$$\Delta \bar{S}_{\text{Cu}} = 12,59 \pm 0,82 \text{ J} \cdot \text{mol}^{-1} \cdot \text{K}^{-1}$$

According to the diagram of solid-phase equilibria, these partial molar functions of copper are

thermodynamic functions of the following potential-forming reaction:



From this equation it follows that the Gibbs integral free energy of the formation of the compound  $\text{Cu}_2\text{SnSe}_3$  can be calculated by the relation:

$$\Delta_f G^\circ(\text{Cu}_2\text{SnSe}_3) = 2\Delta \bar{G}_{\text{Cu}} + \Delta_f G^\circ(\text{SnSe}_2) \quad (7)$$

The enthalpy of formation was calculated in a similar way. The standard entropy can be calculated by the equation:

$$S^\circ(\text{Cu}_2\text{SnSe}_3) = 2\Delta \bar{S}_{\text{Cu}} + 2S^\circ(\text{Cu}) + S^\circ(\text{SnSe}_2) + S^\circ(\text{Se}) \quad (8)$$

In calculations (7) and (8), we used the standard entropies for copper and selenium  $S^\circ(\text{Cu}) = 33.15 \pm 0.08 \text{ J} \cdot \text{mol}^{-1} \cdot \text{K}^{-1}$ ,  $S^\circ(\text{Se}) = 42.13 \pm 0.21 \text{ J} \cdot \text{mol}^{-1} \cdot \text{K}^{-1}$  [28] and also the standard thermodynamic functions of  $\text{SnSe}_2$  found by the EMF method [29]:

$$\Delta_f G^\circ = -119.2 \pm 2.5 \text{ kJ} \cdot \text{mol}^{-1}$$

$$\Delta_f H^\circ = -124.7 \pm 4.2 \text{ kJ} \cdot \text{mol}^{-1}$$

$$S^\circ = 118.0 \pm 3.0 \text{ J} \cdot \text{mol}^{-1} \cdot \text{K}^{-1}$$

The enthalpies of formation of  $\text{SnSe}_2$  compound obtained [29] well agree with the calorimetric data [28, 30]. Moreover, the values of free Gibbs energy of the formation calculated from the values of enthalpy of formation and standard entropy recommended in these reference books virtually coincide with the results of [29]. This demonstrates the reliability of thermodynamic data for  $\text{SnSe}_2$  used in our calculations.

Our results and the literature data are given in Table 2.

Table 1

Results of computer processing of EMF measurements of concentration chains (1)

$T_i, \text{K}$	$E_i, \text{mV}$	$T_i - \bar{T}$	$E_i(T_i - \bar{T})$	$(T_i - \bar{T})^2$	$\bar{E}$	$E_i - \bar{E}$	$(E_i - \bar{E})^2$
301,3	364,9	-76,45	-27895,08	5843,97	364,66	0,24	0,06
308,1	365,6	-69,65	-25462,52	4850,54	365,54	0,06	0,00
317,9	367,9	-59,85	-22017,28	3581,52	366,82	1,08	1,16
324,2	368,5	-53,55	-19731,64	2867,16	367,65	0,85	0,73
328,6	367,5	-49,15	-18061,09	2415,31	368,22	-0,72	0,52
333,9	368,3	-43,85	-16148,42	1922,46	368,91	-0,61	0,37
342,2	371,1	-35,55	-13191,06	1263,51	369,99	1,11	1,22
349,1	370,3	-28,65	-10607,55	820,58	370,90	-0,60	0,35
358	370,3	-19,75	-7311,88	389,90	372,06	-1,76	3,09
363,7	373,5	-14,05	-5246,12	197,29	372,80	0,70	0,49
367,5	371,9	-10,25	-3810,43	104,98	373,30	-1,40	1,95
375,3	373,7	-2,45	-914,01	5,98	374,31	-0,61	0,38
382,1	375,3	4,35	1634,12	18,96	375,20	0,10	0,01
389,4	377,3	11,65	4397,12	135,82	376,15	1,15	1,31
395,7	375,5	17,95	6741,79	322,35	376,98	-1,48	2,18
400	377,8	22,25	8407,62	495,25	377,54	0,26	0,07
405,2	379	27,45	10405,13	753,73	378,22	0,78	0,61
412,3	379,5	34,55	13113,31	1193,99	379,14	0,36	0,13
420,6	379,3	42,85	16254,59	1836,48	380,23	-0,93	0,86
428,5	383,3	50,75	19454,07	2575,99	381,26	2,04	4,18
433,4	381,4	55,65	21226,50	3097,39	381,90	-0,50	0,25
438,8	383,2	61,05	23395,96	3727,61	382,60	0,60	0,36
442,5	382,5	64,75	24768,47	4193,10	383,08	-0,58	0,34
447,6	383,6	69,85	26796,06	4879,60	383,75	-0,15	0,02
$\bar{T} = 377,7$	$\bar{E} = 374,6$						

Table 2

Standard integral thermodynamic functions of the  $\text{Cu}_2\text{SnSe}_3$ 

$-\Delta_f G^\circ$	$-\Delta_f H^\circ$	$S^0$	Notes
$\text{kJ} \cdot \text{mol}^{-1}$		$\text{J} \cdot \text{mol}^{-1} \cdot \text{K}^{-1}$	
189.5±2.6	187.5±4.8	251.6±5.0	The present work. EMF method with solid electrolyte
198.4±0.6	198.5±2.9	237±5	[18], EMF method with liquid electrolyte
-	180.5	-	[31], calorimetry method

From table 2, it follows that the data obtained by us on the standard Gibbs energy of formation and enthalpy of formation are somewhat (5 %) lower than the data obtained by the EMF method with liquid electrolyte, where metal tin served as the left electrode [18].

It should also be noted that our data on the standard enthalpy of formation of the  $\text{Cu}_2\text{SnSe}_3$  compound are in better agreement (4% discrepancy) with calorimetric data [31] than the results of [18] (9% discrepancy).

#### 4. CONCLUSION

Using the EMF technique with solid electrolyte  $\text{Cu}_4\text{RbCl}_3\text{I}_2$ , new complexes of mutually-agreed thermodynamic data ( $\Delta_f G^\circ$ ,  $\Delta_f H^\circ$ ,  $S^0$ ) for  $\text{Cu}_2\text{SnSe}_3$  compound are obtained. A comparative analysis of the obtained and published data is carried out. The results of this work confirm the possibility of use of the EMF method with a cation-conducting solid electrolyte to systems containing a more active metal (in our case, tin) than copper.

- [1] C. Coughlan, M. Ibáñez, O. Dobrozhan, A. Singh, A. Cabot, K.M. Ryan Compound Copper Chalcogenide Nanocrystals. Chemical Reviews, vol. 117, no. 9, pp. 5865-6109, 2017.
- [2] Applications of Chalcogenides: S, Se, and Te, ed. by Gurinder Kaur Ahluwalia, Springer, p.445, 2016.
- [3] A.V. Kolobov, J. Tominaga. Chalcogenides. Metastability and Phase Change Phenomena Springer, p. 284, 2012.
- [4] D.M. Rowe. Thermoelectrics Handbook: Macro to Nano. CRC Press, Taylor & Francis Group: Boca Raton, FL, USA, p. 1008, 2006.
- [5] M.B. Babanly, Y.A. Yusibov, V.T. Abishev. Ternary Chalcogenides Based on Copper and Silver, BSU Publisher, p. 341, 1993.
- [6] B.Jiang, P. Qiu, E. Eikeland, H.Chen, Q. Song, D. Ren, T.Zhang, J.Yang, B. Iversen, X. Shi, L.Chen. Cu<sub>8</sub>GeSe<sub>6</sub>-based thermoelectric materials with an argyrodite structure. J. Mater. Chem. C, 2017, v. 5, pp. 943-948.
- [7] X. Shen, C.C. Yang, Y. Liu, G. Wang, H. Tan, Y.H. Tung, G. Wang, X. Lu, J. He, X. Zhou. High-temperature Structural and Thermoelectric Study of Argyrodite Ag<sub>8</sub>GeSe<sub>6</sub>. ACS Appl Mater Interfaces. 2019, v. 11, no. 2, pp.2168-2176.
- [8] M.B. Babanly, Y.A Yusibov, N.B. Babanly. The EMF method with solid-state electrolyte in the thermodynamic investigation of ternary Copper and Silver Chalcogenides. Electromotive force and measurement in several systems. Ed. S.Kara. Intechweb.Org, 2011, pp. 57-78.
- [9] C.S. Sunandana. Introduction to Solid State Ionics: Phenomenology and Applications. CRC Press, 2015, p. 529.
- [10] L. Gao, M-H. Lee, J. Zhang. Metal-cation substitutions induced the enhancement of second harmonic generation in A<sub>8</sub>BS<sub>6</sub> (A =Cu, and Ag; B =Si, Ge, and Sn). New J. Chem., 2019, v. 43, pp. 3719-3724.
- [11] Y. Li, G. Liu, J. Li, K. Chen, G. He, Z. Yang, Y.Han. Ultrafast one-step combustion synthesis and thermoelectric properties of In-doped Cu<sub>2</sub>SnSe<sub>3</sub>. Materials Chemistry and Physics, 2016, v. 1, pp. 398- 404.
- [12] G. Liu, K. Chen, J. Li, Y. Li, M. Zhou, L. Li. Combustion synthesis of Cu<sub>2</sub>SnSe<sub>3</sub> thermoelectric materials. Journal of the European Ceramic Society, 2016, v.36, p.1407-1415.
- [13] A. Zhang, Q. Chen, W. Yao, D. Yang, G. Wang Large-Scale Colloidal Synthesis of Co-doped Cu<sub>2</sub>SnSe<sub>3</sub> Nanocrystals for Thermoelectric Applications. J. Elec. Mater., 2016, v. 45, pp. 19351-1940.
- [14] K.S.Prasad, A.Rao,N.S.Chauhan., R.Bhardwaj. Thermoelectric properties of p- type Sb- doped Cu<sub>2</sub>SnSe<sub>3</sub> near room and mid temperature applications. Appl. Phys. A, 2018, vol. 124, p. 98-102.
- [15] S. Prasad, A. Rao, B. Gahtori, S. Bathula, A.Dhar. Low-temperature thermoelectric properties of Pb doped Cu<sub>2</sub>SnSe<sub>3</sub>. Phys. B: Condensed Matter, 2017, vol. 520, pp.7-12.
- [16] D. Zhao, X. Wang, D. Wu. Enhanced Thermoelectric Properties of Graphene/Cu<sub>2</sub>SnSe<sub>3</sub> Composites. Crystals, 2017, v. 7, pp.71-74.
- [17] R. Ma, G. Liu, J. Li, Y. Li, K. Chen, Y. Han, M.Zhou. Effect of secondary phases on thermoelectric properties of Cu<sub>2</sub>SnSe<sub>3</sub>. Ceramics International, 2017, v. 43, no. 9, pp.7002-7010.
- [18] M.B. Babanly, Y.A. Yusibov. Electrochemical Methods in Thermodynamics of Inorganic Systems, BSU Publisher, Baku, 2011.
- [19] M.B. Babanly, Y.A Yusibov, N.B. Babanly. The EMF method with solid-state electrolyte in the thermodynamic investigation of ternary Copper and Silver Chalcogenides/Electromotive force and measurement in several systems. Ed. S. Kara. Intechweb.Org, 2011, pp. 57-78.
- [20] I.J. Alverdiyev., V.A. Abbasova, Y.A. Yusibov, D.B. Taghiyev, M.B. Babanly. Thermodynamic Study of Cu<sub>2</sub>GeS<sub>3</sub> and Cu<sub>2-x</sub>Ag<sub>x</sub>GeS<sub>3</sub> solid solutions by the EMF method with a Cu<sub>4</sub>RbCl<sub>3</sub>I<sub>2</sub> solid. Russ. J. Electrochem., 2018, v. 54, no. 2, pp. 153–158.
- [21] L.F. Mashadiyeva, Z.T. Gasanova, Yu.A. Yusibov, and M. B. Babanly. Phase Equilibria in the Cu<sub>2</sub>Se–Cu<sub>3</sub>AsSe<sub>4</sub>–Se System and Thermodynamic Properties of Cu<sub>3</sub>AsSe<sub>4</sub>. Inorg. Mater., 2018, v. 54, no. 1, pp. 8–16.
- [22] M.B. Babanly, Z.T.Gasanova, L.F.Mashadiyeva, V.P. Zlomanov and Yu.A. Yusibov. Thermodynamic Study of the Cu–As–S System by EMF Measurements with Cu<sub>4</sub>RbCl<sub>3</sub>I<sub>2</sub> As a Solid Electrolyte. Inorg. Mater., 2012, vol. 48, no. 3, pp. 225–228.
- [23] N.B. Babanly, Z.E. Salimov, M.M. Akhmedov, and M.B. Babanly. Thermodynamic Study of Cu–Tl–Te System Using EMF Technique with Cu<sub>4</sub>RbCl<sub>3</sub>I<sub>2</sub> Solid Electrolyte. Russ. J. Electrochem., 2012, vol. 48, no. 1, p. 68–73.
- [24] N. B. Babanly, Z. S. Aliev, Yu. A. Yusibov, and M. B. Babanly. A Thermodynamic Study of Cu–Tl–S System by EMF Method with Cu<sub>4</sub>RbCl<sub>3</sub>I<sub>2</sub> Solid Electrolyte. Russ. J. Electrochem., 2010, vol. 46, no. 3, p. 354– 358.
- [25] N.B. Babanly, M.B. Babanly, Yu.A. Yusibov Z.S.Aliyev. Phase equilibria in the system Cu–Bi–Se and thermodynamic properties of selenobismuthides of copper. Russian J. of Inorg. Chem., no. 9, vol. 55, 2010, p. 165-176.
- [26] I.J. Alverdiyev, Z.S. Aliev, S.M. Bagheri, L.F.Mashadiyeva, Y.A. Yusibov, M.B. Babanly Study of the 2Cu<sub>2</sub>S+GeSe<sub>2</sub>↔Cu<sub>2</sub>Se+GeS<sub>2</sub> reciprocal system and thermodynamic properties of the Cu<sub>8</sub>GeS<sub>6-x</sub>Se<sub>x</sub> solid solutions. J. Alloys Compd., 2017, vol. 691, pp. 255-262.
- [27] A.G.Morachevskii, G.F.Voronin, I.B. Kutsenok.



- Electrochemical research methods in thermodynamics of metallic systems, in: Akademkniga, Moscow, 2003.
- [28] Database “Thermal Constants of Substances” Yungman, V.S., Ed.: <http://www.chem.msu.su/cgi-bin/tkv>. Cited 2006.
- [29] *B.T. Melekh, N.B. Stepanova, T.A. Fomina.* Thermodynamic properties of compounds in the Sn–Se system, *Zh. Fiz. Khim.*, 1971, v. 45, p. 2018.
- [30] *O. Kubaschewski, C.B. Alcock and P.J. Spenser. Materials Thermochemistry*, Oxford: Pergamon, 1993.
- [31] *V.V. Lebed', S.A. Bondar, L.I. Berger.* Calorimetric study of some triple chalcogenides *Electronic Engineering. Ser. 6 “Materials”*, 1972, no. 1, p. 78-82.

*Received: 02.09.2019*

## OPTICAL AND UV-VIS LUMINESCENCE SPECTRA OF $\text{Ni}_{1-x}\text{Zn}_x\text{Fe}_2\text{O}_4$ FERRITE NANOPOWDERS

A.A. SADIGOVA, Sh.N. ALIYEVA, Sh.A. AHMADOVA,  
I.F. YUSIBOVA, T.G. NAGHIYEV, T.R. MEHDIYEV

*G.M. Abdullayev Institute of Physics of NASA,  
Azerbaijan AZ-1143, Baku, H. Javid ave., 131*

The optical and UV-VIS luminescent spectra of  $\text{Ni}_{1-x}\text{Zn}_x\text{Fe}_2\text{O}_4$  ferrite nanopowders with  $x = 0; 0,25; 0,4; 0,5; 0,6; 0,75; 1,0$  were investigated in  $4000\text{--}50\text{ cm}^{-1}$  and  $200\text{--}700\text{ nm}$  at room temperature. The features of the diffuse reflectance spectra of  $\text{Ni}_{1-x}\text{Zn}_x\text{Fe}_2\text{O}_4$  ferrites were analyzed by the Kramers- Kronig procedure. The agreement with the data of published studies of other authors allowed us to give a hypothetical interpretation of the results.

**Keywords:** ferrites, nanopowders, IR spectra.

**PACS:** 41.20 Gz; 42.72 Ai

### 1. INTRODUCTION

$\text{Ni}_{1-x}\text{Zn}_x\text{Fe}_2\text{O}_4$  is compositions of d-elements which allow to create new types elements for modern nanoelectronics. Well known the practical applications of their as magnetic cores, antennas, memory elements, microwave components, etc. The peculiarities of these ferrites is related their the crystal of structure with the formula  $(\text{Zn}^{2+}_x\text{Fe}^{3+}_{2-x})[\text{Ni}^{2+}_{1-x}\text{Fe}^{3+}_{2-x}]\text{O}_4$  ( $x$  is the degree of inversion) which allow us to define their as mixed spinels. From peculiarities building of crystal structure of these spinels follow the existence superexchange interaction investigation of which define our interest to these ferrites. Earlier in [1-4] were published the results investigations of EPR, Raman, IR and etc. spectra. In this publication we presented results of optical and luminescent investigations nanopowders  $\text{Ni}_{1-x}\text{Zn}_x\text{Fe}_2\text{O}_4$ . The luminescent spectra were excited by different wavelength from of xenon source and YAG Nd- laser.

### 2. SAMPLES PREPARATION

$\text{Ni}_{1-x}\text{Zn}_x\text{Fe}_2\text{O}_4$  synthesized by high-temperature method with high purity components and annealing 2 hours at  $960^\circ\text{C}$  [3,5]. The size of particles is from 20nm to 40 nm. The quality of nanopowders was monitored by X-ray diffractograms and optical methods. It is shown that lattice distortions resulting from deviation from stoichiometry have small effect on Raman spectra. Detailed X-ray studies of the formation of  $\text{Ni}_{1-x}\text{Zn}_x\text{Fe}_2\text{O}_4$  ferrite films have shown that the process of their formation, as pointed in [5], goes through three stages: at the first stage  $\text{ZnFe}_2\text{O}_4$  is obtained, while part of NiO and  $\text{Fe}_2\text{O}_3$  remain in the free state; in second stage the process of including  $\text{Ni}^{2+}$  ions in the  $\text{ZnFe}_2\text{O}_4$  lattice begins and compound with an excess of Ni is formed against stoichiometry; in the third stage the composition is finally formed. The observed changes were in good agreement with concentration of  $\text{Fe}^{3+}$  cations [5] in the  $\text{Ni}_{1-x}\text{Zn}_x\text{Fe}_2\text{O}_4$  films. We note that it was established in [6] that the most homogeneous composition of  $\text{ZnFe}_2\text{O}_4$  is achieved when using  $\alpha\text{-Fe}_2\text{O}_3$ . A significantly smaller

concentration of Fe is included into the ZnO in samples obtained when using FeO and  $\text{Fe}_3\text{O}_4$ . The spatial symmetry group of  $\text{Ni}_{1-x}\text{Zn}_x\text{Fe}_2\text{O}_4$ , corresponded to  $\text{Fd}\bar{3}\text{m}$ .

### 3. DETAILS OF EXPERIMENTS

Optical spectra of  $\text{Ni}_{1-x}\text{Zn}_x\text{Fe}_2\text{O}_4$  ( $x=0; 0,25; 0,4; 0,5; 0,6; 0,75; 1,0$ ) compositions are studied on infrared Fourier-spectrometer Vertex-70V (Bruker, Germany) with attachment of diffuse reflection in vacuum camera in spectral range from  $4000\text{cm}^{-1}$  up to  $50\text{cm}^{-1}$ , the standard spectral resolution is better than  $0,5\text{cm}^{-1}$  [2, 3]. The luminescence spectra of synthesized  $\text{Ni}_{1-x}\text{Zn}_x\text{Fe}_2\text{O}_4$  ferrite nanopowders were studied on LS-55 spectrometer with a Monk-Giddison monochromator at 300C in the 300-700nm range. The luminescent spectra excited with wavelengths: 280 nm, 290 nm, 300 nm, 325 nm, 350 nm, 375 nm, 400 nm, 425 nm from the xenon source. The luminescent spectra of  $\text{Ni}_{1-x}\text{Zn}_x\text{Fe}_2\text{O}_4$  compositions were also investigated on the Confocal Raman Spectrometer with of radiation 3D Confocal Laser Microspectroscopy System Nanofinder 30 (Tokyo Instruments, Japan). The YAG Nd- laser is generate radiation 53 nm) with power from 0.1 mW to 10 mW [1].

### 4. EXPERIMENTAL RESULTS AND THEIR DISCUSSION

#### 4.1 EXPERIMENTAL RESULTS OF OPTICAL INVESTIGATIONS

The infrared spectra of all studied ferrite  $\text{Ni}_{1-x}\text{Zn}_x\text{Fe}_2\text{O}_4$  compositions are shown in fig. 1-2. The absorption maxima and fine structures in the region from  $4000\text{cm}^{-1}$  to  $50\text{cm}^{-1}$  spectra were established as a result of repeated experiments and are shown in Table 1, which allows to identify the positions of genetically related spectral lines in different  $\text{Ni}_{1-x}\text{Zn}_x\text{Fe}_2\text{O}_4$  compositions, consistent with the results of [7,8]. When analyzing the obtained spectra, it was found that their profiles have a complex structure and when changing the composition of the composition (see table 1), not only a shift is noticeable, but also splitting into spectral components. The temperature in all the studies was equal to 300K.

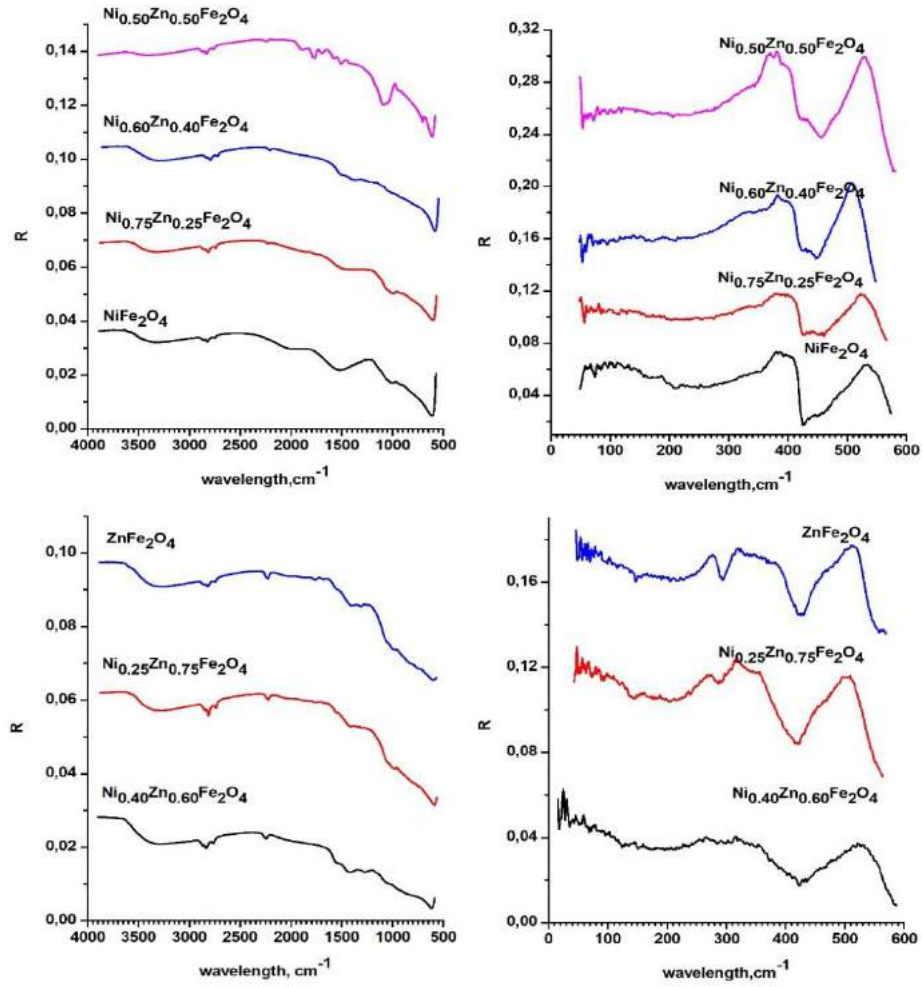


Fig. 1. Diffuse reflection IR spectra of  $\text{Ni}_{1-x}\text{Zn}_x\text{Fe}_2\text{O}_4$  ferrites in  $4000\text{--}700\text{cm}^{-1}$  and in  $600\text{--}50\text{cm}^{-1}$ .

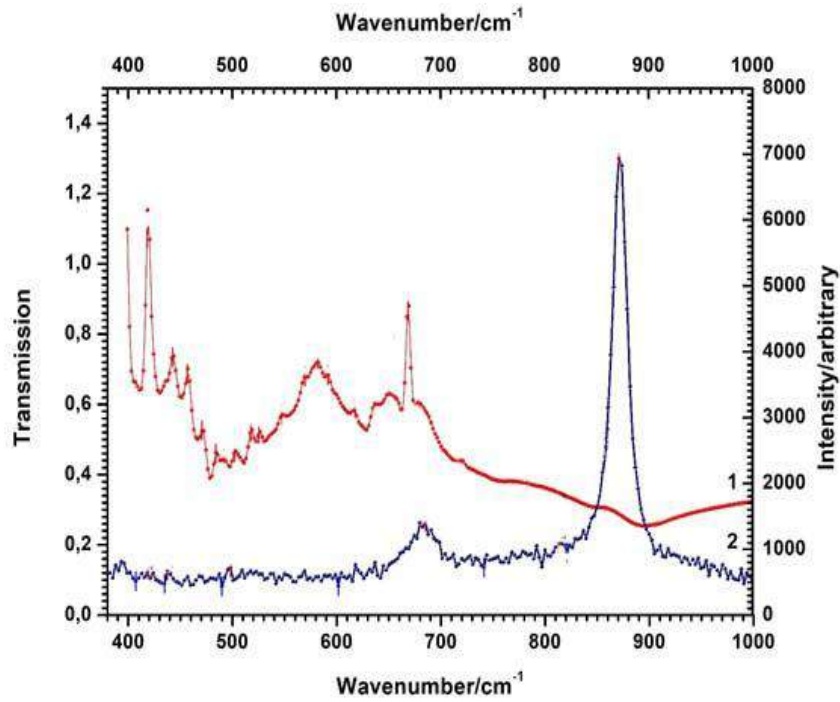


Fig. 2. The FTIR (1) transmission and Raman (2) spectra of  $\text{Ni}_{0.4}\text{Zn}_{0.6}\text{Fe}_2\text{O}_4$  thin film.

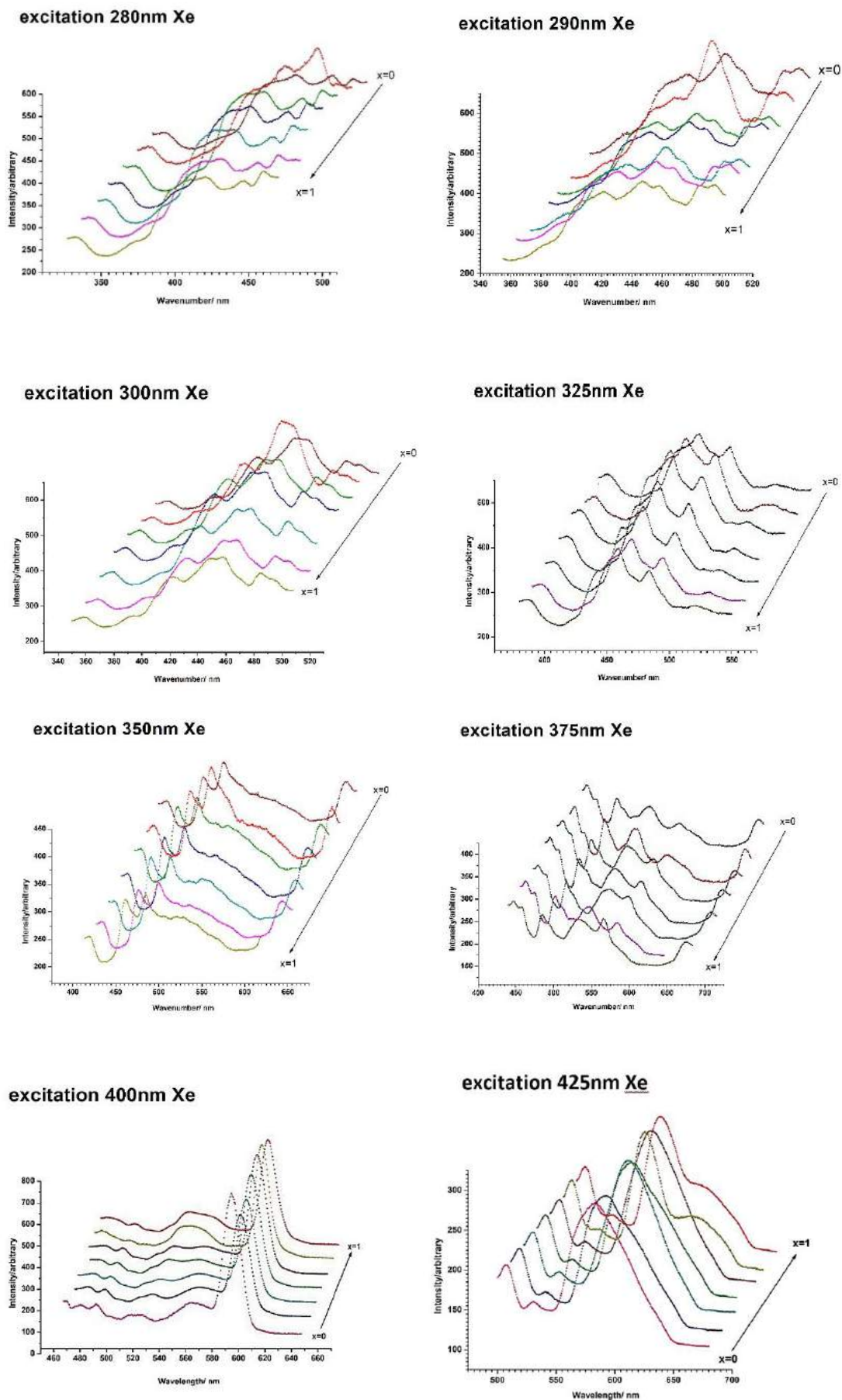


Fig. 3. Luminescent spectra of  $\text{Ni}_{1-x}\text{Zn}_x\text{Fe}_2\text{O}_4$  compositions.

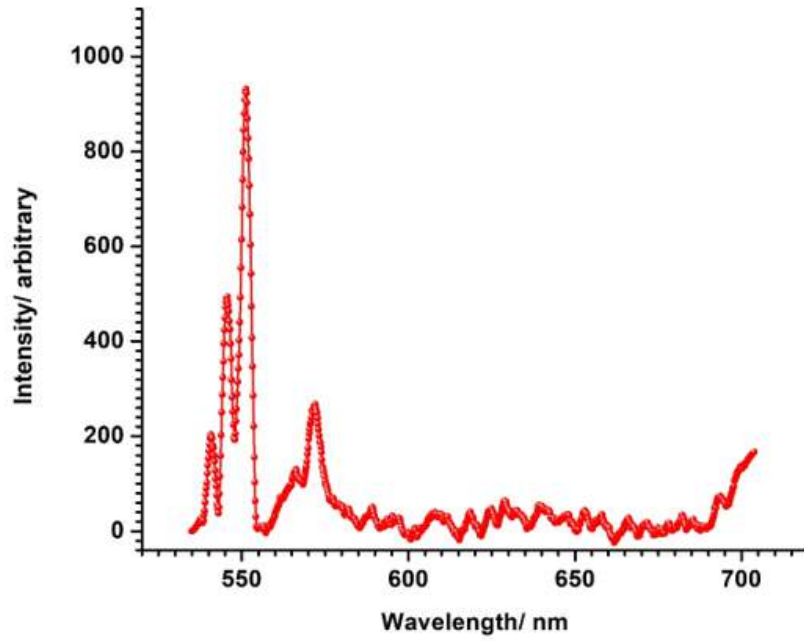


Fig. 4. The luminescent spectrum of  $Ni_{0.4}Zn_{0.6}Fe_2O_4$  (excitation by of YAG Nd laser,  $\lambda = 532nm$ ) with the radiation power of 5mW. The maxima correspond to: 540 nm, 545 nm, 551 nm, 566 nm, 572 nm.

Table 1.

The maxima of  $Ni_{1-x}Zn_xFe_2O_4$  infrared spectra

Frequencies of $Ni_{1-x}Zn_xFe_2O_4$ ferrites, $cm^{-1}$												
	[8]			[8]			[8]		[8],[15]			[8], [9]
symmetry \ x	0	0	0.25	0.3	0.4	0.5	0.5	0.6	0.7	0.75	1.0	1.0
$F_{1u}^1$	604	604	592	590	584	578	578	582	571[8] 582[15]	570	-	569 [9]-
		-	-		-	544		544		550	542	542 [8]
		533	538		522			535		-	-	
		529	528		512	529		525		516	519	
		-	524		508	-		518		506	507	
		-	456		497	454		-		500	471	463 [8]
		443	442		437	436		-		-	-	
		432	433			429		430		-	-	
$F_{1u}^2$	426	425	426	426	426	424	426	-	426[8]	421	426	420 [9]
		-	403		401	-		403	401[15]	394	398	
		392	391		389	389		388		391	388	
		-	367		363	356		-		330	332	
		349	345		346	343		324		-	-	
		306	306		304	300		299		308	313	
		273	275		270	266		284		287	294	
$F_{1u}^3$		249	247		-	248		236		-	247	
		-	204		204	206		195		206	206	206 [8]
		169	169		171	173		163		177	183	
		96	93		95	95		128		81	84	
		95	90		89	88		55		77	80	
		-	85		84	83		52		73	76	
		74	76		71	72		43		58	69	

This work, nm	Some scientific publications											
	Luminescence, nm						Optical absorption, nm					
	ZnFe <sub>2</sub> O <sub>4</sub> [9]	NiFe <sub>2</sub> O <sub>4</sub> [10,14]	Ni:ZnO[3*] Ni <sub>1-x</sub> Zn <sub>x</sub> Fe <sub>2</sub> O <sub>4</sub> [18]	NiO [4*]	Fe <sub>3</sub> O <sub>4</sub> [5*], Fe <sub>2</sub> O <sub>3</sub> Fe <sup>3+</sup> in maghemite (m) and hematite (h) [19]		Fe <sup>3+</sup> [15]		Fe <sup>2+</sup> and Fe <sup>3+</sup> [16]		Ni <sup>2+</sup> [17]	
332					315 (m) and 319 (h) [19]	<sup>6</sup> A <sub>1</sub> → <sup>4</sup> T <sub>1</sub>	330	<sup>6</sup> A <sub>1g</sub> → <sup>4</sup> E(G)			330	<sup>3</sup> A <sub>2g</sub> (F) → <sup>1</sup> T <sub>2g</sub> (G)
373	365	372 [10]		370	370 (m) [19]	<sup>6</sup> A <sub>1</sub> → <sup>4</sup> E			372	<sup>5</sup> E → <sup>3</sup> E of <sup>T</sup> Fe <sup>2+</sup>		
381				381	380 (h) [19]	<sup>6</sup> A <sub>1</sub> → <sup>4</sup> E	385	<sup>6</sup> A <sub>1g</sub> → <sup>4</sup> A <sub>1g</sub> (G)	385	<sup>5</sup> E → <sup>3</sup> T <sub>2g</sub> , <sup>3</sup> T <sub>1g</sub> of <sup>T</sup> Fe <sup>2+</sup>	385	<sup>3</sup> A <sub>2g</sub> (F) → <sup>1</sup> T <sub>1g</sub> (G)
396	401			396	400 [13]				402	<sup>6</sup> A <sub>1g</sub> → <sup>4</sup> E <sub>g</sub> of <sup>O</sup> Fe <sup>3+</sup>	400	<sup>3</sup> A <sub>2g</sub> (F) → <sup>3</sup> T <sub>1g</sub> (P)
406				410	403 (m) and 405 (h) [19]	<sup>6</sup> A <sub>1</sub> → <sup>4</sup> T <sub>2</sub>	410					
421	428	428 [14]										
448	454	441 [14]			434 (m) and 444 (h) [19]	<sup>6</sup> A <sub>1</sub> → <sup>4</sup> E, <sup>4</sup> A <sub>1</sub>	440	<sup>6</sup> A <sub>1g</sub> → <sup>4</sup> T <sub>2g</sub> (G)				
462	468	459, 465 [14]	460[18]						459	<sup>6</sup> A <sub>1g</sub> → <sup>4</sup> A <sub>1g</sub> , <sup>4</sup> E <sub>g</sub> of <sup>O</sup> Fe <sup>3+</sup>	464	<sup>3</sup> A <sub>2g</sub> (F) → <sup>1</sup> T <sub>1g</sub> (D)
486		486 [10]	484[18]	481					477	<sup>6</sup> A <sub>1g</sub> → <sup>4</sup> A <sub>1g</sub> , <sup>4</sup> E <sub>g</sub> of <sup>O</sup> Fe <sup>3+</sup>		
496	494	496 [14]		490								
507		502 [14]		507	510 (m) [19]	2 <sup>6</sup> A <sub>1</sub> → 2 <sup>4</sup> T <sub>1</sub>						
521		530 [10]	518[18]		529 (h) [19]	2 <sup>6</sup> A <sub>1</sub> → 2 <sup>4</sup> T <sub>1</sub>	525	<sup>6</sup> A <sub>1g</sub> → <sup>4</sup> T <sub>1g</sub> (G)				
541 (R)			541[18]									
545(R)	539	535 [14]										
551(R)									555	<sup>5</sup> E → <sup>3</sup> T <sub>2</sub> of <sup>T</sup> Fe <sup>2+</sup>		
559(R)												
566(R)			565 [11]		565 [3]							
571(R)												
597	593	594 [14]							588	<sup>5</sup> E → <sup>3</sup> T <sub>1</sub> of <sup>T</sup> Fe <sup>2+</sup>		
606												
627							650	<sup>6</sup> A <sub>1g</sub> → <sup>4</sup> T <sub>1g</sub> (G)				
636					649 (h) [19]	<sup>6</sup> A <sub>1</sub> → <sup>4</sup> T <sub>2</sub>			631	<sup>4</sup> A <sub>2</sub> (F) → <sup>4</sup> T <sub>1</sub> (P)		
673	665		660[18]		666 (m) [19]				670	<sup>O</sup> Fe <sup>2+</sup> ↔ <sup>O</sup> Fe <sup>3+</sup>		

Here: From [17]: 642nm, 662nm, 682nm – tetrahedral (split); 656nm Fe<sup>3+</sup> -tetrahedral; 682nm Fe<sup>2+</sup> tetrahedral; 950nm - Fe<sup>2+</sup> -octahedral and 2000nm - Fe<sup>2+</sup> -tetrahedral [17] don't include to table; <sup>O</sup>Fe -octahedral and <sup>T</sup>Fe – tetrahedral iron cations; (D), (F), (G), (P) – terms of free ions. Luminescence maxima 540 nm, 545 nm, 551 nm, 566 nm, 572 nm of Ni<sub>1-x</sub>Zn<sub>x</sub>Fe<sub>2</sub>O<sub>4</sub> ferrites are interpreted as a consequence of the Raman effect [1].

The analysis of optical spectra of investigated compositions of  $\text{Ni}_{1-x}\text{Zn}_x\text{Fe}_2\text{O}_4$  ferrites in  $4000\text{cm}^{-1}$ - $500\text{cm}^{-1}$  range shows that the information about spectra of ZnO, NiO and  $\text{Fe}_2\text{O}_3$  components is necessary for interpretation of spectral peculiarities. To identify the peculiarities of the optical reflection spectra of  $\text{Ni}_{1-x}\text{Zn}_x\text{Fe}_2\text{O}_4$  ferrites, the Kramers-Kronig procedure was used.

The transmission spectrum of  $\text{Ni}_{0.4}\text{Zn}_{0.6}\text{Fe}_2\text{O}_4$  ferrite (fig. 2) was obtained on a thin film 40 nm thick in vacuum and is consistent with the diffuse reflectance spectrum of the nanopowder of this ferrite. The strong maximum observed in this composition of ferrite from the Raman spectrum is confirmed by the presence in the spectrum of its transmission of a very weak structure, which is explained by the prohibition by the rules of symmetry. Note that the following maxima were observed in this luminescence spectrum: 540 nm, 545 nm, 551 nm, 566 nm, 572 nm.

#### 4.2 EXPERIMENTAL RESULTS OF LUMINESCENT INVESTIGATIONS

The luminescent spectra (Fig. 3-4) of synthesized  $\text{Ni}_{1-x}\text{Zn}_x\text{Fe}_2\text{O}_4$  compositions were studied at 300C from 300nm to 700nm and excited: 280 nm (4.427eV), 290 nm (4.275eV), 300 nm (4.132eV), 325 nm (3.814eV), 350 nm (3.542eV), 375 nm (3.306eV), 400nm (3.099eV), 425 nm (2.917eV) from the Xe-source and 532 nm (2.33eV) from the YAG Nd laser. The results are presented in Table 2. For the analysis of spectra, the procedure of decomposing into Gaussian components was used. Table 2 presents the comparison the positions of the luminescent maxima of  $\text{ZnFe}_2\text{O}_4$  [9],  $\text{NiFe}_2\text{O}_4$  [10,14],  $\text{Ni:ZnO}$  [11],  $\text{Ni}_{1-x}\text{Zn}_x\text{Fe}_2\text{O}_4$  [18], NiO [12] and  $\text{Fe}_3\text{O}_4$  [13] compounds and maxima of optic absorption spectra [15-17].

#### 4.3 DISCUSSION OF OPTICAL AND LUMINESCENT INVESTIGATIONS RESULTS

As follows from the group-theoretical representations, the infrared reflection spectra of  $\text{Ni}_{1-x}\text{Zn}_x\text{Fe}_2\text{O}_4$  three-fold degenerate symmetry modes  $F_{1u}$  should be observed. These oscillations are asymmetric with respect to the center of inversion and symmetric with respect to a second-order axis or vertical reflection planes ( $\sigma_v$ ). Note that the masses of Fe, Ni and Zn elements, which are part of the studied ferrites, are much higher than the mass of the oxygen ion and, therefore, the oscillations of oxygen ions will have almost no effect on the positions of heavy ions, while, naturally, will affect the vibrations of the oxygen ion. The shift of the oxygen atom can occur either along the axis of the third order  $C_3$ , or perpendicular to it [20]. In the first case, the  $F_{1u}^1$  bond is observed in  $\text{Me}^{2+} - \text{O} - 3\text{Me}^{3+}$  (where  $\text{Me}^{2+}$  is octahedral cation,  $3\text{Me}^{3+}$ -three tetrahedral cations). This oscillation corresponds to the high-frequency band of the spectrum. When oxygen is displaced perpendicular to the  $C_3$  axis,  $F_{1u}^2$  bonds  $\text{Me}^{3+} - \text{O} -$

$2\text{Me}^{3+}$  bonds are observed. This oscillation corresponds to the low-frequency band of the spectrum. The oscillations of cations relative to each other  $F_{1u}^3$  (the bond  $\text{Me}^{3+} - \text{Me}^{3+}$ ) of symmetry type occur at lower frequencies and have weak intensities. Note that during the processes of cation substitutions, the parameter "a" of the unit cell also changes. First of all, we note that the weakly intense, broad absorption band ( $3627\text{--}3500\text{cm}^{-1}$ ) corresponds to the contribution from the  $(\text{OH})^-$  ions to the spectrum, the appearance of which indicates a high surface activity of ferrite microparticles due to the presence of dangling bonds and, as a result, to a high probability of adsorption by ions  $(\text{OH})^-$  and  $\text{H}^+$  of active  $\text{OH}^-$  groups [21]. As was shown in [22], the presence of OH-groups allows magnetite nanoparticles, an analogue of  $\text{Ni}_{1-x}\text{Zn}_x\text{Fe}_2\text{O}_4$  ferrites, to easily bind with polymeric compounds. The absorption band at  $1630\text{cm}^{-1}$  was interpreted as deformation vibrations HOH, and at  $823\text{cm}^{-1}$  and  $1045\text{cm}^{-1}$  as deformation vibrations of the Zn-O-H and Fe-O-H bonds. The absorption bands in the frequency range with maxima around  $430\text{cm}^{-1}$  and  $542\text{cm}^{-1}$ , which are combined vibration bands of Fe-O valence bonds in octahedral positions with  $\text{Zn}^{2+}$  ions in the nearest coordination environment: Fe-O-Zn, are primarily, on the formation of a spinel structure. They can also be observed, for example, in  $\text{ZnFe}_2\text{O}_4$ .

As is well known,  $\text{Ni}_{1-x}\text{Zn}_x\text{Fe}_2\text{O}_4$  ferrites do not dissolve excessive amounts of NiO and ZnO. On the other hand, an excessive amount of  $\text{Fe}_2\text{O}_3$  leads to the formation of a solid solution containing a mixture of  $\text{Ni}_{1-x}\text{Zn}_x\text{Fe}_2\text{O}_4$  and magnetite  $\text{Fe}_3\text{O}_4$ . Note also that in order to achieve a steady state, various forms of disorder in the form of point defects and vacancies always appear in spinel structures, the stability and concentration of which practically do not change until the thermodynamic equilibrium is violated. In the spectra of  $\text{Fe}_2\text{O}_3$ , the Fe-O bonds are represented by the characteristic doublet of the bands  $545\text{cm}^{-1}$  and  $470\text{cm}^{-1}$ , respectively  $F_{1u}^1$  and  $F_{1u}^2$  types of symmetry. In magnetite and nanomagnetite, similar doublets observed in ( $595\text{ cm}^{-1}$  and  $415\text{ cm}^{-1}$ ) and ( $590\text{ cm}^{-1}$  and  $415\text{ cm}^{-1}$ ) ranges. The doublet structure ( $590\text{ cm}^{-1}$  and  $413\text{ cm}^{-1}$ ) is also observed in ZnO micropowders. In the spectral band ( $530\text{ cm}^{-1}$ – $430\text{ cm}^{-1}$ ) there is a structure corresponding to the Ni-O bond in NiO. Comparison of the IR spectra of ZnO, NiO and  $\text{Fe}_2\text{O}_3$  with the spectrum of  $\text{NiFe}_2\text{O}_4$  makes it possible to interpret the doublet ( $604\text{ cm}^{-1}$  and  $425\text{ cm}^{-1}$ ) as oscillations of Ni-O and Fe-O bonds, respectively. As follows from Table 1, with an increase in "x" in the  $\text{Ni}_{1-x}\text{Zn}_x\text{Fe}_2\text{O}_4$  compositions, the line shifts to  $604\text{cm}^{-1}$  towards  $570\text{ cm}^{-1}$ ; and in  $\text{ZnFe}_2\text{O}_4$  it is recorded as a line of  $542\text{ cm}^{-1}$  [23] or  $569\text{ cm}^{-1}$  [24]. As is known, for the composition of magnetite  $\text{Fe}_3\text{O}_4$ , the positions of the IR spectrum lines are  $624\text{ cm}^{-1}$ ,  $591\text{ cm}^{-1}$  and  $425\text{ cm}^{-1}$  [25]. Note that the position of the  $425\text{ cm}^{-1}$  line, interpreted as oscillations of the  $F_{1u}^2$  type of symmetry, is practically independent of the change in "x" in  $\text{Ni}_{1-x}\text{Zn}_x\text{Fe}_2\text{O}_4$ , which allows interpreting it as oscillations of Fe-O bonds, that is ( $\text{Fe}^{3+} - \text{O} - 2\text{Fe}^{3+}$ ).



The dependences of the intensities of the obtained IR spectra of the  $\text{Ni}_{1-x}\text{Zn}_x\text{Fe}_2\text{O}_4$  compositions under study were interpreted within the framework of a model that takes into account changes in the concentrations of  $\text{Fe}^{2+}$  [26] and  $\text{Fe}^{3+}$  cations [27] in ferrite compositions. As follows from the results obtained, a change in the concentrations of these cations with a change in "x" leads to changes in the intensity of the reflection spectra, the maximum of which is located near the composition  $x = 0.6$ . Near this composition, the difference in the concentration of  $\text{Fe}^{2+}$  cations decrease sharply and at  $x = 0.7$  it becomes equal to the concentration of  $\text{Fe}^{3+}$  cations. A change in the concentrations of  $\text{Fe}^{2+}$  and  $\text{Fe}^{3+}$  cations in ferrite compositions indicates a change in the number of "jump" electrons in the superexchange interaction and, since these electrons, according to the model [28], form their "own" magnetic field, the change in their concentrations should affect the overall magnetic distribution fields in ferrite. This conclusion is confirmed by the EPR studies of the  $\text{Ni}_{1-x}\text{Zn}_x\text{Fe}_2\text{O}_4$  ferrites [4]. Correspondingly, the frequencies of the vibrational spectrum of the magnetic "subcoil" "jumping" electrons can to observe in the IR spectra of the ferrite compositions under study. This fact was also confirmed by studies of antiferromagnetic resonance in  $\text{NiO}$ :  $\text{Fe}^{2+}$  [29], in which the presence in the IR absorption spectrum at a temperature of 300K of the structure at  $1600\text{cm}^{-1}$ , which coincides with the position of the two-magnetic zone previously detected in the Raman scattering spectra, was established. According to the authors of the publication, this structure has an impurity character. In our studies, in different  $\text{Ni}_{1-x}\text{Zn}_x\text{Fe}_2\text{O}_4$  compositions, the position of such a structure is found in the spectral band  $(1550-400)\text{cm}^{-1}$ , practically without changing its position. However, changes in the intensity of this spectral band are consistent with a model that takes into account changes in the concentrations of  $\text{Fe}^{2+}$  and  $\text{Fe}^{3+}$  cations in different  $\text{Ni}_{1-x}\text{Zn}_x\text{Fe}_2\text{O}_4$  compositions.

As shown in table 1, oscillations of the  $F_{1u}^3$  type, occurring between like cations, are observed in the region of the far IR spectrum from  $300\text{cm}^{-1}$  to  $50\text{cm}^{-1}$ . They correspond to the spectral lines  $249\text{cm}^{-1}$  ( $\text{NiFe}_2\text{O}_4$ ), and  $206\text{cm}^{-1}$  ( $\text{ZnFe}_2\text{O}_4$ ). The presence of a line at about  $249\text{cm}^{-1}$  in all compositions of  $\text{Ni}_{1-x}\text{Zn}_x\text{Fe}_2\text{O}_4$  indicates its belonging to vibrations  $\text{Fe}^{3+} - \text{Fe}^{3+}$  bonds. Accordingly, the line  $206\text{cm}^{-1}$  is observed only in compositions in which Zn is present. An absorption maximum of  $206\text{cm}^{-1}$  was observed in  $\text{ZnFe}_2\text{O}_4$ , also, for example, in [30]. The lines of antiferromagnetic resonance in  $\text{NiO}$  ( $36\text{cm}^{-1}$ ) [31] and  $\text{Fe}_2\text{O}_3$  ( $10\text{cm}^{-1}$ ) [32] are also located in this region. As follows from the results of [4], the presence of a magnetic field of "jumping" electrons [28] can lead to the appearance of antiferromagnetic resonance in  $\text{Ni}_{1-x}\text{Zn}_x\text{Fe}_2\text{O}_4$  ferrites, which is estimated to be in the region of  $\sim 2-3\text{THz}$  ( $70\text{cm}^{-1}-100\text{cm}^{-1}$ ).

Note that the detected dependence of the intensity of the IR spectrum in different compositions  $\text{Ni}_{1-x}\text{Zn}_x\text{Fe}_2\text{O}_4$ , consistent with the model of changes in cation concentrations, in particular,  $\text{Fe}^{2+}$  and  $\text{Fe}^{3+}$  (as well as  $\text{Ni}^{2+}$ ,  $\text{Ni}^{3+}$ ,  $\text{Zn}^{2+}$ ), implicitly implies the

presence of noticeable electron-phonon interaction and the effect impurity atoms in the formation of the IR spectrum of all compositions of ferrites, and, as mentioned above, point defects and vacancies always appear in order to achieve a steady state in spinel structures. Note that the shape of the spectrum of an impurity is related to the intensity of a set of electronic-vibrational transitions of the corresponding electronic transition of an impurity, and the shape of the vibronic satellite of a phononless line is determined by the states of the system in the initial and final states. In particular, theoretical studies [33] of the  $\text{Ni}^{3+}$  impurity charged with respect to the  $\text{ZnO}$  crystal lattice showed that the interaction of the impurity with the ions of the nearest environment leads to the appearance of a large number of additional maxima, among which resonant and gap oscillations were detected at frequencies of  $8.2\text{THz}$  ( $273\text{cm}^{-1}$ ) and  $11.2\text{THz}$  ( $373\text{cm}^{-1}$ ).

Photoluminescence spectroscopy is an important tool for the study of electronic and optical properties, in this case,  $\text{Ni}_{1-x}\text{Zn}_x\text{Fe}_2\text{O}_4$  ferrites, providing information on the structure of their forbidden zones, in the positions and states of defects and impurities. For completeness of information, the luminescence spectra were obtained at different excitation energies. Table 2 presents the comparison the positions of the luminescent [9-14, 18] and optic absorption spectra maxima [15-17]. Note that the photoluminescence maxima  $540\text{nm}$ ,  $545\text{nm}$ ,  $551\text{nm}$ ,  $566\text{nm}$ ,  $572\text{nm}$  of  $\text{Ni}_{1-x}\text{Zn}_x\text{Fe}_2\text{O}_4$  ferrites (fig. 3-4), observed upon excitation with the  $532\text{nm}$  line from the YAG Nd laser, are interpreted as a consequence of the Raman effect, the study of which can be found in [1].

Characteristic, as indicated in [34] for the tetrahedral oxygen environment of the  $\text{Fe}^{3+}$  cation is the presence of absorption bands of about  $435\text{nm}$  and the absence of bands of  $909\text{nm}$ . In this case, the  $448\text{nm}$  luminescence band observed in our experiments in  $\text{Ni}_{1-x}\text{Zn}_x\text{Fe}_2\text{O}_4$  can be assigned to the  ${}^6\text{A}_{1g} \leftarrow {}^4\text{T}_{2g}$  transition, the  $407\text{nm}$  band to the  ${}^6\text{A}_{1g} \leftarrow {}^4\text{T}_{2g}$  transition, and  $373\text{nm}$  to the degenerate transitions:  ${}^6\text{A}_{1g} \leftarrow {}^4\text{A}_{1g}$  и  ${}^6\text{A}_{1g} \leftarrow {}^4\text{E}$ .

The UV- V is photoluminescence spectra of  $\text{NiFe}_2\text{O}_4$  were obtained upon excitation by the  $325\text{nm}$  line. It can be noted that the observed violet maxima at  $372\text{nm}$ ,  $420\text{nm}$ , the blue band at  $486\text{nm}$  and the green band at  $530\text{nm}$  are quite consistent and interpreted with the published absorption and luminescence spectra (see table 2).

Radiation from the violet region, as indicated in [35], arises due to transitions of electrons from the shallow donor level to the valence band. Blue radiation was attributed to free and bound excitons at the band boundary [36]. In addition, it is generated by electronic transitions from the near conduction band to acceptors of deep levels and transitions from deep donor levels to the valence band [37]. The green  $530\text{nm}$  band of radiation refers to an oxygen vacancy with other defects associated with the vacancy [38].

Physically, the basis of the  $\text{Ni}_{1-x}\text{Zn}_x\text{Fe}_2\text{O}_4$  photoluminescent spectra interpretation was the conclusions of the crystal field theory [39-41] and



other]. In crystalline fields of tetrahedral and octahedral symmetries, the fivefold degenerate 6S level of the 3d5 electrons of the  $\text{Fe}^{3+}$  cation is split into two energy levels, separated by an energy gap of  $10Dq$  (fig.5). The type of splitting is determined by

the symmetry of the environment with  $\text{O}^{2-}$  anions. The splitting of the transition metal ion levels in an octahedrally coordinated crystal field is opposite to the tetrahedral field, that is, with a higher doublet eg and lower triplet  $t_{2g}$ .

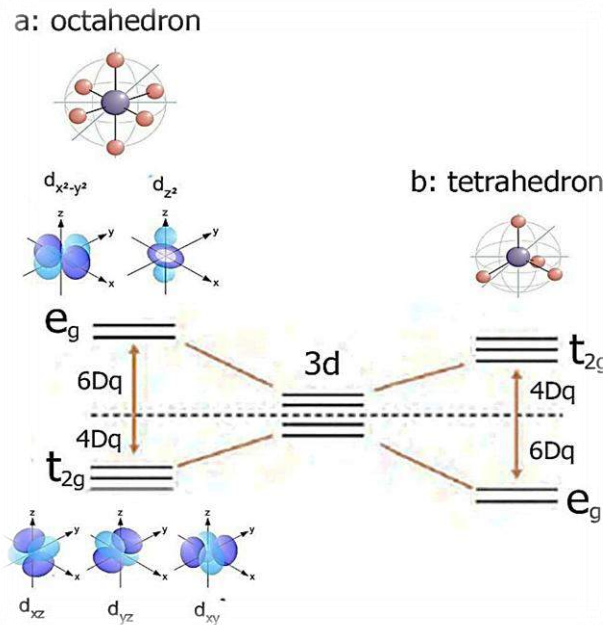


Fig. 5. (a) octahedral and (b) tetrahedral symmetry. In the crystal field, the 3d5 orbital splits into doublet  $e_g$  and triplet  $t_{2g}$  levels. The amount of splitting between levels is  $10 Dq$ .

- a. octahedral symmetries: the doubly degenerate  $e_g$  level and the triple degenerate  $t_{2g}$  level form a high-spin electron configuration  $(t_{2g})^3(\uparrow)(e_g)^2(\uparrow)$  with an effective spin of  $5/2$ . Crystal field stabilization energy (CFSE) for electrons  $t_{2g}$  and  $e_g$ :

$$(\text{CFSE}) = 3 \times (-0.4\Delta_{\text{oct}}) + 2 \times (0.6\Delta_{\text{oct}}) = 0$$

- b. The (CFSE) for low-spin electron configuration  $(t_{2g})^5(\uparrow)(e_g)^0(\uparrow): 5 \times (-0.4\Delta_{\text{oct}}) + 2P = -2\Delta_{\text{oct}} + 2P$ , where  $2P$  is pairing energy term
- c. For  $\text{Fe}^{2+}$  cation ( $d^6$  ion) in a spherical crystal field, one d orbital contains spin-paired electrons and four orbitals is singly occupied. The high-spin electron configuration in octahedral field is  $(t_{2g})^4(\uparrow)(e_g)^2(\uparrow)$  and  $(\text{CFSE}) = -0.4\Delta_{\text{oct}}$ . For a low-spin  $d^6$  electron configuration  $(t_{2g})^6(\uparrow)(e_g)^0(\uparrow)$   $(\text{CFSE}) = -2.4\Delta_{\text{oct}} + 2P$
- d. For  $\text{Ni}^{2+}$  cation ( $d^8$  ion) in a spherical crystal field, d orbital contains three spin-paired electrons and two orbitals is singly occupied. The high-spin electron configuration in octahedral field is  $(t_{2g})^6(\uparrow)(e_g)^2(\uparrow)$  and  $(\text{CFSE}) = -1.2\Delta_{\text{oct}}$
- e. For  $\text{Zn}^{2+}$  cation ( $d^{10}$  ion) in a spherical crystal field, d orbital is full and  $(\text{CFSE}) = 0$

Additional splitting of the  $e_g$  and  $t_{2g}$  levels can occur as a result of tetragonal, trigonal, or orthorhombic distortions of tetrahedrons and octahedra [42], and these levels are filled with electrons in accordance with the Hund rule. According

to the Jahn – Teller theorem (JT), in the ground state only spin degeneracy is allowed, and all other degeneracy is removed with small distortions of the octahedra or tetrahedra, which reduce the symmetry of the crystal [43]. Then: for  $d^5$ , a weak low-spin JT is observed; for  $d^6$  - weak high-spin JT; for  $d^8$  - not JT effect expected.

For a regular tetrahedron, the splitting of the d orbitals is inverted compared with that for a regular octahedral structure, and the energy difference  $\Delta_{\text{tet}}$  is smaller. The relative splittings:  $\Delta_{\text{tet}} = 4/9\Delta_{\text{oct}}$ . As well known, tetrahedral complexes are almost invariably high-spin. Only a strong field ligand which lowers the symmetry of the complex can lead to a low-spin ‘distorted tetrahedral’ system.

## CONCLUSION

The optical and luminescent spectra of  $\text{Ni}_{1-x}\text{Zn}_x\text{Fe}_2\text{O}_4$  ferrite nanopowders with  $x=0; 0.25; 0.4; 0.5; 0.6; 0.75; 1.0$  were investigated in  $4000\text{-}50\text{ cm}^{-1}$  and  $200\text{-}700\text{ nm}$  at room temperature. The agreement with the data of published studies of other authors allowed us to give a hypothetical interpretation of the results.

## ACKNOWLEDGEMENTS

The present work is supported by Science Development Foundation under the President of the Republic of Azerbaijan (grant № EIF-BGM-3-BRFTF- 2+/ 2017-15/04/1 and grant № EIF-2013-9(15)-46/05/1).

- [1] S. Aliyeva, S. Babayev, T. Mehdiyev. Raman spectra of  $\text{Ni}_{1-x}\text{Zn}_x\text{Fe}_2\text{O}_4$  nanopowders, *JRS* 2018; 49 (2), 271.
- [2] Sh.N. Aliyeva, A.M. Kerimova, R.B. Abdullayev, T.R. Mehdiyev. IR spectra of  $\text{Ni}_{1-x}\text{Zn}_x\text{Fe}_2\text{O}_4$  ferrite micropowders, *PhSS*, 2017, v. 59, no. 3, pp. 528 – 533.
- [3] Sh.N. Aliyeva. Magnetic properties of  $\text{Ni}_{1-x}\text{Zn}_x\text{Fe}_2\text{O}_4$  micropowders and thin films, Baku, 2017, p. 199.
- [4] Sh.N. Aliyeva, Y.N. Aliyeva, A.I. Nadjafov, I.S. Hasanov, E.K. Huseynov T.R. Mehdiyev. EPR and SPM studies of Zn-Ni ferrites, *Phys. Status Sol. (c)*, 615, 2015/DOI 10.1002/pssc.201400273.
- [5] N.N. Scholtz, K.A. Piskarev. Ferrimagnetic materials for radio-frequencies, Publishing House Energy, Moscow, 2013.
- [6] U.V. Kasyuk, L.A. Bliznyuk, N.A. Basov, A.K. Fedotov, A.S. Fedotov, I.A. Svito. Structure and electro-physical properties of doped ceramics on the base of zinc oxide. The theses of International conference, Minsk, November 22 – 25, 2016, vol. 2, pp. 84-86.
- [7] J. Nishitani, K. Kozuki, T. Nagashima, M. Hangyo. *Appl. Phys. Lett.* 2010, 96, 221906-1.
- [8] F.Sh. Tehrani, V. Daadmehr, A.T. Rezakhani, R.H. Akbarnejad, S. Gholipour. *J. Supercond. Novel Magnetism*, 2012, 25, 2443.
- [9] R.C. Sripriya, Ezhil Arasi S. Madhavan. J. Victor Antony Raj M. Synthesis and Characterization studies of  $\text{ZnFe}_2\text{O}_4$  nanoparticles, *MMSE Journal* vol.9, iss.1, 2017, p.13-18.
- [10] K. Kombaiyah, J. Judith Vijaya\*, L. John Kennedy, K. Kaviyarasu. Catalytic studies of  $\text{NiFe}_2\text{O}_4$  nanoparticles prepared by conventional and microwave combustion method, *Materials Chemistry and Physics* 221, 2019, 11–28.
- [11] Jamil K. Salem, Talaat M. Hammad, Roger R. Harrison. Synthesis, structural and optical properties of Ni-doped ZnO microspheres, *J Mater Sci: Mater Electron*, 2012, DOI 10.1007/s10854-012-0994-0.
- [12] P.A. Sheena, K.P. Priyanka, N. Aloysius Sabu, Bobby Sabu, Thomas Varghese. Effect of calcination temperature on the structural and optical properties of nickel oxide nanoparticles, *Nanosystems: Physics, Chemistry, Mathematics*, 2014, 5 (3), p.441-449.
- [13] M.E. Sadat, Masoud Kaveh Baghbador, Andrew W. Dunn, H.P. Wagner, Rodney C. Ewing, Jiaming Zhang, Hong Xu, Giovanni M. Pauletti, David B. Mast and Donglu Shi. Photoluminescence and photothermal effect of  $\text{Fe}_3\text{O}_4$  nanoparticles for medical imaging and therapy, *Applied Physics Letter*, 105, 0919031-091903-5, 2014.
- [14] Walmir E. Pottker, Rodrigo Ono, Miguel Angel Cobos, Antonio Hernando, Jefferson F.D.F. Araujo, Antonio C.O. Bruno, Sidney A. Lourenço, Elson Longo, Felipe A. La Porta. Influence of order-disorder effects on the magnetic and optical properties of  $\text{NiFe}_2\text{O}_4$  nanoparticles, 44, 2018, 17290–17297.
- [15] S. Lakshmi Reddy, Tamio Endo and G. Siva Reddy. Electronic (Absorption) Spectra of 3d Transition Metal Complexes, in book IntechOpen: Advanced Aspects of Spectroscopy, chapter 1, 2012.
- [16] Veronica D'Ippolito, Giovanni Battista Andreozzi, Ulf Hålenius, Henrik Skogby, Kathrin Hametner, Detlef Günther. Color mechanisms in spinel: cobalt and iron interplay for the blue color, *Phys Chem Minerals*, 2015, 42:431–439.
- [17] H.K. Mao and P.M. Bell. Crystal-field effects in spinel: oxidation states of iron and chromium, *Geochimica et Cosmochimica Acta*, 1975, vol. 39, pp. 869 to 871.
- [18] F. Shahbaz Tehrani, V. Daadmehr, A.T. Rezakhani, R. Hosseini Akbarnejad, S. Gholipour. Structural, magnetic, and optical properties of zinc- and copper- substituted nickel ferrite nanocrystals *Journal of Superconductivity and Novel Magnetism*, 2012, vol. 25, issue 7, pp 2443-2455, DOI:10.1007/s10948-012-1655-5.
- [19] David M. Sherman and T. David Waite. Electronic spectra of  $\text{Fe}^{3+}$  oxides and oxide hydroxides in the near IR to near UV, *American Mineralogist*, vol. 70, p. 1262-1269, 1985.
- [20] The Infrared Spectra of Minerals, 539 pp., Mineral.Soc., London, 1974.
- [21] J.T. Keiser, C.W. Brown, R.H. Heidersbach. Infrared spectra of magnetite nanoparticles, *J. Electrochem. Soc.* 1982, vol. 129, p. 2686.
- [22] Ma M., Zhang Yu., Wei Yu. et. al. Preparation and characterization of magnetite nanoparticles coated by amino silane, *Colloids and Surfaces: Physicochem. Eng. Aspects*. 2003, vol.212, p.219-226.
- [23] F. Shahbaz Tehrani, V. Daadmehr, A.T. Rezakhani, R. Hosseini Akbarnejad, S. Gholipour. Structural, magnetic, and optical properties of zinc- and copper- substituted nickel ferrite nanocrystals *Journal of Superconductivity and Novel Magnetism*, 2012, vol. 25, issue 7, pp 2443-2455, DOI:10.1007/s10948-012-1655-5.
- [24] Jiaqi Wan, Xuehui Jiang, Hui Li and Kezheng Chen. Facile synthesis of zinc ferrite nanoparticles as non-lanthanide T1 MRI contrast agents, *Journal of Material Chemistry*, 2012, 22, 13500-13505.
- [25] Zahra Rezay Marand, Mitra Helmi Rashid Farimani, Nasser Shahtahmasebi. Study of magnetic and structural and optical properties of Zn doped  $\text{Fe}_3\text{O}_4$  nanoparticles synthesized by co-precipitation method for biomedical

- application, *Nanomedicine Journal*, v. 1, no. 4, 2014, p. 238-247.
- [26] Santosh S. Jadhav, Sagar E. Shirsath, B.G. Toksha, S. J. Shukla, K. M. Jadhav. Effect of Cation Proportion on the Structural and Magnetic Properties of Ni-Zn Ferrites Nano-Size Particles Prepared By Co-Precipitation Technique, *Chinese Journal of Chemical Physics*, vol.21, N4, 2008, p.381-386.
- [27] F. Shahbaz Tehrani, V. Daadmehr, A.T. Rezakhani, R. Hosseini Akbarnejad, S. Gholipour. Structural, magnetic, and optical properties of zinc- and copper- substituted nickel ferrite nanocrystals *Journal of Superconductivity and Novel Magnetism*, 2012, vol. 25, issue 7, pp 2443-2455, DOI:10.1007/s10948-012-1655-5.
- [28] K.P.Belov. Ferrimagnets with “weak” magnetic sublattice, *UFN*, 1996, June, vol. 166, no. 6, pp. 669 – 681.
- [29] C.R. Becker, Ph. LAU, R.Geick and V. Wagner. Antiferromagnetic Resonance in  $\text{NiO}:\text{Co}^{2+}$  and  $\text{NiO}:\text{Fe}^{2+}$ , *Phys.Stat.Sol. (b)* 67, 653-663 1975.
- [30] Vidales J.L. M., A.L. Delgado, E. Vila and F.A. Lopez. The effect of the starting solution on the physico-chemical properties of zinc ferrite synthesized at low temperature, *J. Alloys Comp.*, 1999, 287, 276.
- [31] Junichi Nishitani, Kohei Kozuki, Takeshi Nagashima and Masanori Hangyo. Terahertz radiation from coherent antiferromagnetic magnons excited by femtosecond laser pulses, *Appl. Phys. Lett.*, 96, p. 221906-1-221906-3, 2010.
- [32] Shin G. Chou, Paul E. Stutzman, Shuangzhen Wang, Edward J. Garboczi, William F. Egelhoff, and David F. Plusquellic. High-Resolution Terahertz Optical Absorption Study of the Antiferromagnetic Resonance Transition in Hematite ( $\alpha\text{-Fe}_2\text{O}_3$ ), *J. Phys. Chem. C*, 2012, 116 (30), p.16161–16166.
- [33] A.N. Kislov, V.G. Mazurenko, A.N. Varaksin. Analysis of vibronic structure of optical spectra in  $\text{ZnO}:\text{Ni}^{+3}$  crystals on the base of localized oscillation modelling, *Phys. Stat. Sol.*, 1999, vol. 4, pp. 618 – 622.
- [34] A.B.P. Lever. *Inorganic Electronic Spectroscopy*. Amsterdam: Elsevier, 1968; D.M. Sherman, T.D. Waite. Electronic spectra of  $\text{Fe}^{3+}$  oxides and oxide hydroxides in the near IR to near UV, *Amer. Mineralogist*. 1985, 70, p. 1262.
- [35] A.V.Dijken, E.A.Meulenkaamp, D.Vanmaelbergh, A. Meijerink. The Kinetics of the radiative and nonradiative processes in nanocrystalline ZnO particles upon photoexcitation, *J. Phys. Chem. B* 104, 2000, 1715-1723.
- [36] L.Jing, Y. Qu, B. Wang, S. Li, B. Jiang, L. Yang, W.Fu, H.Fu. Review of photoluminescence performance of nano-sized semiconductor materials and its relationships with photocatalytic activity, *J. Sun, Sol. Energy Mater. Sol. Cells* 90, 2006, 1773-1787.
- [37] R.K. Sendi, S. Mahmudm, Quantum size effect on ZnO nanoparticle-based discs synthesized by mechanical milling, *Appl. Surf Sci.* 258, 2012, 8026–803.1.
- [38] J. Becker, K.R. Raghupathi, J. St Pierre, D. Zhao, R.T. Koodal. Tuning of the crystallite and particle sizes of ZnO nanocrystalline materials in solvothermal synthesis and their photocatalytic activity for dye degradation, *J. Phys. Chem. C* 115, 2011, 13844-13850
- [39] D.I. Khomskii. *Transition metal oxides*. Cambridge University Press, Cambridge, 2014. ISBN: 978-1-107-02017-7.
- [40] Burns, Roger G. *Mineralogical. Applications of Crystal Field Theory*, ISBN 10: 0521076102/ISBN 13: 9780521076104, Published by Cambridge University Press, Cambridge, 1970.
- [41] E. Pavarini, E.Koch, F.Anders. *Correlated Electrons: From Models to Materials*, *Crystal-field Theory, Tight-binding Method, and Jahn-Teller Effect* Julich 2012, ISBN 978-3-89336-796-2.
- [42] D.I. Khomskii. *Transition metal oxides*. Cambridge University Press, Cambridge, 2014. ISBN: 978-1-107-02017-7.
- [43] I.B. Bersuker. *The Jahn-Teller Effect*. Cambridge University Press, Cambridge, 2006. ISBN 139780521822121.

Received: 06.09.2019

SCANNING PROBE MICROSCOPY STUDIES OF FULLERENE C<sub>60</sub>/POROUS SILICON MULTILAYER STRUCTURES

YEGANA ALIYEVA

*G.M. Abdullayev Institute of Physics of Azerbaijan NAS**131, H. Javid ave., Baku, AZ 1143*

The C<sub>60</sub>/glass, C<sub>60</sub>/porous Si/Si (C<sub>60</sub>/PS/Si) thin film structures were prepared and studied by scanning probe microscopy at room temperature. AFM image of the fullerene C<sub>60</sub> film deposited on glass substrate at room temperature, obtained in non-contact mode shows the dense and regular character of the clusters. Carbon and silicon distributions in the porous part of the C<sub>60</sub>/PS/Si structure were determined. It was shown that the C<sub>60</sub> molecules penetrate deep into PS closely to single part of the silicon. Moreover, the EDS analysis shows the presence of oxygen in PS along with the C<sub>60</sub> molecules.

**Keywords:** fullerene, porous silicon, scanning probe microscopy.**PACS:** 535.399

## 1. INTRODUCTION

C<sub>60</sub> thin films deposited on different substrates have been prepared and extensively studied for a long time since the discovery [1] of C<sub>60</sub> bucky ball molecules. Today, room temperature solid phase of C<sub>60</sub> is known as phase centered cubic (fcc) pristine C<sub>60</sub> [2] or, shortly, fullerite C<sub>60</sub>. The available vast experimental data on optical and electronic properties of fullerite C<sub>60</sub> witness that along with emerged band properties, solid state manifestation of C<sub>60</sub> retain clear-cut molecular fingerprints, such as vibronic transitions and Frenkel excitons [3].

Interpretation of the available numerous experimental data on optical transitions at, below and above band gap remain rather controversial up to now. According to optical absorption and luminescence measurements [4-6], the distance between the occupied (HOMO) and unoccupied (LUMO) states is between 1.5 and 2.7 eV. Such a big uncertainty is largely associated with the overlapping of the spectral features of the molecular and purely band transitions at small values of absorption coefficient.

In the present work scanning probe microscopy (AFM, SEM, EDS) studies of C<sub>60</sub> thin films on soda lime glass (SLG) substrate and C<sub>60</sub>/PS/Si multilayer structures, for which the molecular radiative transitions strongly dominate over interband radiative transitions, are studied. X-ray diffraction and Raman spectroscopy analyses are also done for the sake of completeness. The results of the studies can be useful for the interpretation of the available numerous experimental data on optical transitions in these structures.

## 2. EXPERIMENTAL DETAILS

High purity (99.99%) fullerene powder (C<sub>60</sub>) was deposited on soda lime glass substrate (C<sub>60</sub>/SLG) by sublimation technique in a vacuum of 10<sup>-6</sup> Torr. For comparison, the same fullerene powder was also deposited directly on silicon (C<sub>60</sub>/Si) and porous silicon (C<sub>60</sub>/PS/Si) preliminarily fabricated on silicon substrate by anodic etching. The thicknesses of C<sub>60</sub> films were measured during evaporation by using a

deposition controller (Inficon, Leybold) and were in the range of 100-200 nm. PS layers with thickness of 10-20 μm were prepared on p-type Si substrate (with resistivity ρ≈10 Ω.cm) by anodic etching in HF: H<sub>2</sub>O solution under the white illumination [7]. The average porosity, i.e. the void fraction in the porous layer was measured by gravimetric technique, using the equation  $P = \{(m_1 - m_2) / (m_1 - m_3)\} 100 \%$  [8]. Here  $m_1$  is Si sample mass before the etching,  $m_2$  after etching and  $m_3$  after the removal of the porous layer by rapid dissolution of the completely porous layer in a 3% KOH solution. The porous silicon thickness ( $d$ ) was determined using the equation  $d = (m_1 - m_2) / \rho S$ , where  $\rho$  is the Si density (2.33 g/cm<sup>3</sup>) and  $S$  is the etched surface. The average porosity for PS layers and density of pores were found to be 70-75% and 3.4 10<sup>10</sup> cm<sup>-2</sup>, respectively.

X-ray diffraction (XRD) analyses of the films were carried out using Bruker D2 Phaser (Germany) diffractometer in  $\theta$ -2 $\theta$  scan mode with Ni-filtered CuK $\alpha$  radiation ( $\lambda=1.54060$  Å) source.

Topography analysis of the films were performed in Smart SPM 1000 AIST NT (Tokyo Instruments, Japan). Cross-section and elemental analyses of the multi-layer structures carried out using Scanning Electron Microscopy SEM S-4800 with EDS system (Hitachi Ltd., Japan).

Raman spectra were measured by Confocal PL/Raman microscope Nanofinder 30-NM01 (Tokyo Instruments, Inc.). All of the measurements were performed at room temperature.

## 3. RESULTS AND DISCUSSIONS

XRD patterns of the films did not reveal any noticeable reflexes. A weak reflex around 2  $\theta$ ~11° (most intensive line of C<sub>60</sub> with high degree of crystallinity [9]) appears after relatively long time exposure of the samples to X-rays. This is caused, in the first place, by low thicknesses of the obtained films. Of course, incomplete crystallization of the films obtained at room temperature contributes as well. However, the results of the detailed Raman studies on the films show that the last factor is not decisive.

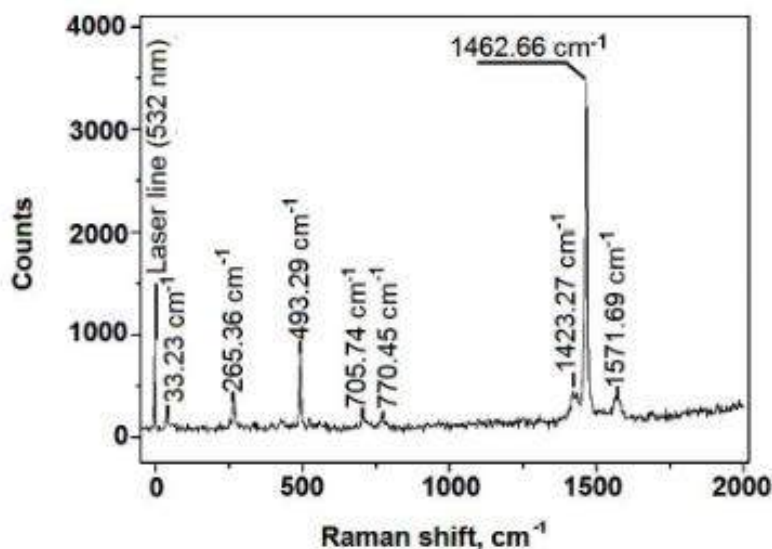


Fig. 1. Raman shift of C<sub>60</sub> film on SLG substrate.

The Raman spectrum of a C<sub>60</sub> film excited with 532 nm laser is shown in Figure 1. Close inspection of the obtained spectrum shows that the last reproduces practically all Raman active modes observed so far on the perfect examples of C<sub>60</sub> solids [4,8]. These modes lie above 260 cm<sup>-1</sup> and are intra-molecular in nature. The mode with frequency 33 cm<sup>-1</sup> is external (inter-

molecular) mode and corresponds to librational motions [4].

Figure 2 shows the 3D AFM image of the fullerene C<sub>60</sub> films deposited on soda lime glass (SLG) substrates at room temperature. The image is obtained in non-contact mode taken over a scale of 4 × 4 μm<sup>2</sup>.

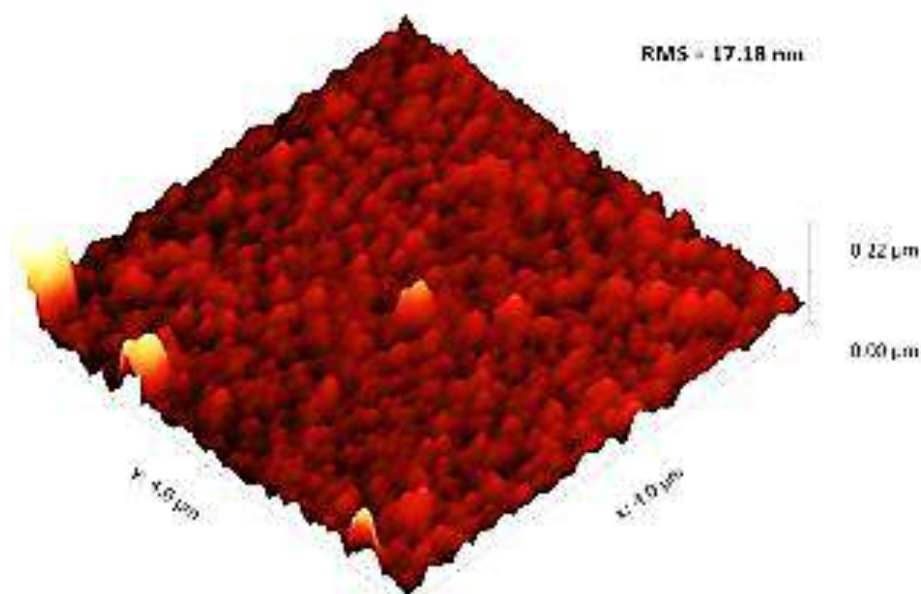


Fig. 2. AFM image of C<sub>60</sub> film on glass substrate.

Common surface roughness indices, such as root mean square (RMS) roughness and mean roughness (Ra), are 17.8 nm and 17.3 nm, respectively. It is seen that the prepared C<sub>60</sub> film is dense and characterized by regularity of the clusters.

In fig. 3, 2D (upper, left hand) and cross-section (upper, right-hand) Scanning Electron Microscopy (SEM) and Energy Dispersive Spectroscopy (EDS) (lower, left - hand) images of C<sub>60</sub>/PS/Si multilayer

structure is displayed.

Lower right-hand picture shows carbon, silicon and oxygen distributions in the porous part of the structure. As it is clearly seen, the C<sub>60</sub> molecules penetrate deep into PS closely to single part of the silicon.

Moreover, the EDS analysis shows the presence of oxygen in PS along with the C<sub>60</sub> molecules.



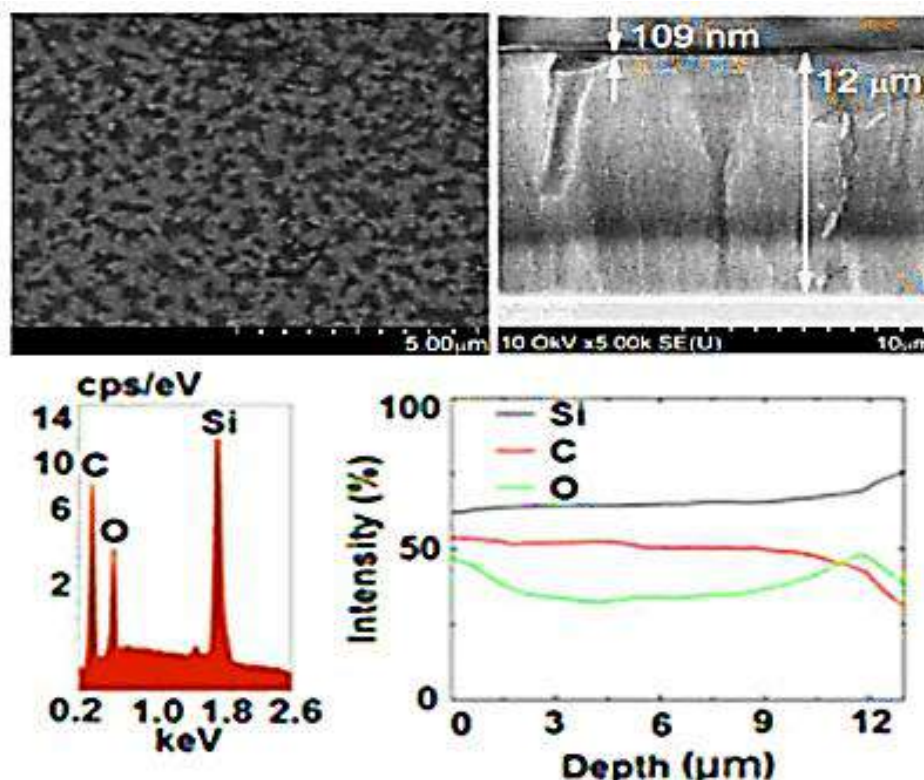


Fig. 3. 2D (upper row, left hand) and cross-section (upper row, right-hand) SEM and EDS (lower row, left hand) and Si, C, O distribution (lower row, right hand) images of  $C_{60}$ /PS/Si structure.

#### 4. CONCLUSION

Fullerene  $C_{60}$  film on glass is dense and characterized by regularity of the clusters. The Raman spectrum of the film shows that the last reproduces practically all Raman active modes observed so far on

the perfect examples of  $C_{60}$  solids.  $C_{60}$  molecules in the  $C_{60}$ /PS/Si multilayer structures penetrate deep into PS closely to single part of the silicon. The EDS analysis shows the presence of oxygen in PS along with the  $C_{60}$  molecules.

- [1] A. Rohlfing, D.M. Cox, A.J. Kaldor. Production and characterization of supersonic carbon cluster beams, J. Chem. Phys. 81(7), 1984, 3322-3330.
- [2] W.I. David, R.M. Ibberson, J.C. Matthewman, K.Prassides, T.J.Dennis, J.P. Hare, H.W. Kroto,
- [3] R. Taylor, D.R. Walton. Crystal Structure and Bonding of Ordered  $C_{60}$ , Nature 353, 1991, 147-149.
- [4] J. Feldmann, R. Fischer, W. Guss, E.O. Gobel, S. Schmitt-Rink, W. Kratschmer. White Luminescence from Solid  $C_{60}$ , Europhys. Lett. 20, 1992, 553-558.
- [5] M.S. Dresselhaus, G. Dresselhaus, P.C. Eklund. Science of Fullerenes and Carbon Nanotubes, Academic Press, 1995.
- [6] E.L. Shirley, S.G. Louie. Electron Excitations in Solid  $C_{60}$ . Energy Gap, Band Dispersions, and Effects of Orientational Disorder, Phys. Rev. Lett. 71, 1993, 133-136.
- [7] P. Sibley, S.M. Argentine, A.H. Francis. A photoluminescence study of  $C_{60}$  and  $C_{70}$ , Chem. Phys. Lett. 188, 1992, 187-193.
- [8] D. Faiman, S. Goren, E.A. Katz, M. Koltun, N. Melnik, A. Shames, S. Shtutina. Structure and optical properties of  $C_{60}$  thin films, Thin Solid Films 295, 1997, 283-286.
- [9] T.D. Dzhaifarov, C. Oruc, S. Aydin. Humidity-voltaic characteristics of Au-porous silicon interfaces, J. Phys. D: Appl. Phys. 37, 2004, pp.404-409.
- [10] H. Kuzmany, R. Pfeiffer, M. Hulman, C. Kramberger. Raman spectroscopy of fullerenes and fullerene-nanotube composites, Phil. Trans. Roy. Soc. London A362, 2004, 2375-2406.

Received: 09.09.2019

## SmS THIN FILMS WITH NANOSIZE SURFACE ARCHITECTURE

YEGANA ALIYEVA

*G.M. Abdullayev Institute of Physics of Azerbaijan NAS**131, H. Javid ave., Baku, AZ 1143**e-mail: yeganaaliyeva85@gmail.com*

Samarium sulfide thin films with thickness in the range from 40 to 100 nm were deposited on vacuum annealed sapphire plates that received ion beam treatment after annealing to reduce surface roughness. The deposited thin films were then subjected to vacuum annealing and ion beam treatment again and films surfaces good enough to use scribing to create nanosize surface elements were obtained. Diffraction grating was then prepared with the aid of a diamond coated cantilever and examined using electric force (EF) and magnetic force (MF) modes of atomic force microscope (AFM). The prepared grating was shown to have semiconducting channels between the metallic grooves separated from one another by 100 nm distance. The disclosed distinct properties of the grating are discussed in terms of variable valence of Sm ions. It is figured out that SmS thin films are very promising as materials to scribe on and obtain desirable surface architecture.

**Keywords:** Atomic Force Microscopy, SmS polycrystalline film, nanoscale structures, diffraction grating, Magnetic Force Microscopy, Electric Force Microscopy.

**PACS:** 535.399

## 1. INTRODUCTION

Phase-change materials revolutionized media industry by providing inexpensive, high-speed, portable and reliable platform for vast volume data storage. Such a great application became possible due to semiconductor-to-metal phase transition that dramatically changes all their physical properties, allowing eventually to controllable switching between two stable states. This work is addressed to feasibility of using the rare-earth based phase-change material such as SmS to obtain multifunctional elements at the nanoscale. The idea underlying the work originates from variable valence of Sm, that leads to semiconductor-to-metal phase transition in SmS under mechanical deformation.

SmS advantageously differ from other semiconductors in that metallic state is reached in this material under quite low external pressure. It has recently become clear [1] that SmS polycrystalline films exhibit cluster structure. The cluster sizes in SmS films vary within 5 -100 nm, depending on film growth conditions and after-growth treatment. A semiconductor-type conductivity is observed for cluster larger than 20 nm. On the other hand, conductivity is metallic when cluster size is below 20 nm [1]. SmS is known as n-type cubic semiconductor with lattice parameter  $a = 5.97 \text{ \AA}$  at room temperature [1]. SmS shows semiconductor-to-metal phase transition under pressure due to the change of the valence of Sm ions from  $\text{Sm}^{2+}$  to  $\text{Sm}^{3+} + e$  [2]. Normally, 4f-levels of  $\text{Sm}^{2+}$  ions positioned in the knots of the crystal lattice of SmS are 0.23 eV below the conduction band bottom. However, they move at a rate of 0.16 meV/MPa towards conduction band bottom under compression and enter conduction band.

According to model calculations [3], the pressure of phase transition into metallic state is more than 1000 MPa and 650 MPa for thin film and bulk material, respectively. Heating of the polished (and, hence, partly metallic) SmS samples up to 500 -600 K

leads, as observed [4], to reversible change back to completely semiconducting phase. Note that voltage emerging during such heating performed in the absence of temperature gradients [5] is indicative of concentration gradients caused by Sm excess against its stoichiometric concentration.

## 2. PREPARATION DETAILS

### 2.1 THIN FILM AND DIFFRACTION GRATING PREPARATION

We used thermo-vacuum deposition technique [2] to obtain SmS submicron thin films. In our case substrate temperature was 600 C while deposition from target occurred at 2500- 2700 C. Film thickness was monitored during deposition using well-known piezo-plate method [6].

It is straightforward that substrate selection is very important for obtaining homogeneous thin films of such a "gentle" material like SmS. The main criterion for selection is possibly small lattice mismatch between substrate and samarium sulfide. Besides, surface roughness of the used substrate shall be negligible. As our observations have shown, unfulfilling of either of the above two conditions results in inhomogeneous SmS thin films due to local mechanic deformation.

We used sapphire substrates which were preliminary annealed at 1500°C during 4 hours.

After annealing, substrates received ion treatment for 2 hours in addition. Above annealing and ion cleaning were repeatedly performed unless surface roughness of the substrates was down to 6 nm.

Thickness of the SmS thin films obtained on sapphire substrates was within 40 -100 nm. Annealing at 600°C followed SmS thin film deposition. Perfection of the annealed films was examined using X-ray diffraction technique by means of a XRD D2 PHASER (Bruker, Germany). Surface topography of the films was studied using atomic force microscopy

system AFM SmartSPM™ with measuring head AIST-NT. Resonance frequency of diamond cantilever was 305.6 kHz.

Fig. 1 (a) and 1 (b) show topographic images of sapphire substrate and SmS film deposited on this substrate, respectively. Surface roughness of the substrate is below 6 nm while that of SmS film is below 3 nm. We used scribing method [7] to prepare diffraction grating on the surface of SmS thin films. The parameters such as scribing rate, depth etc. were

varied in accordance with preliminary estimations done with allowance for relevant properties of thin film and cantilever materials.

3D images of the diffraction grating obtained on the surface of the synthesized SmS films are shown in fig. 2. The images belong to the same grating.

The total area of the obtained grating is up to  $10 \times 10 \mu\text{m}^2$ . The groove frequency is  $10 \mu\text{m}^{-1}$ , the scribing depth is from 10 to 20 nm (by about 15 nm).

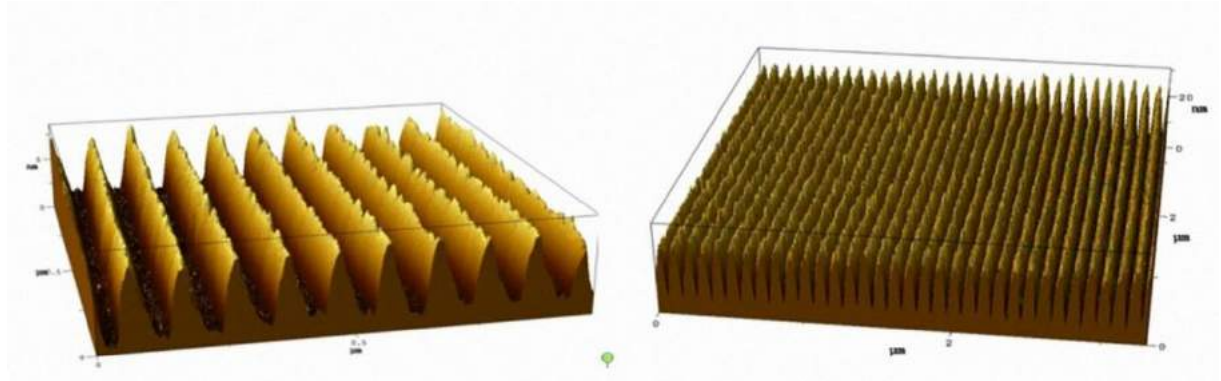


Fig. 1. "Diffraction lattice" type nanoelements on the surface of nanothickness SmS.

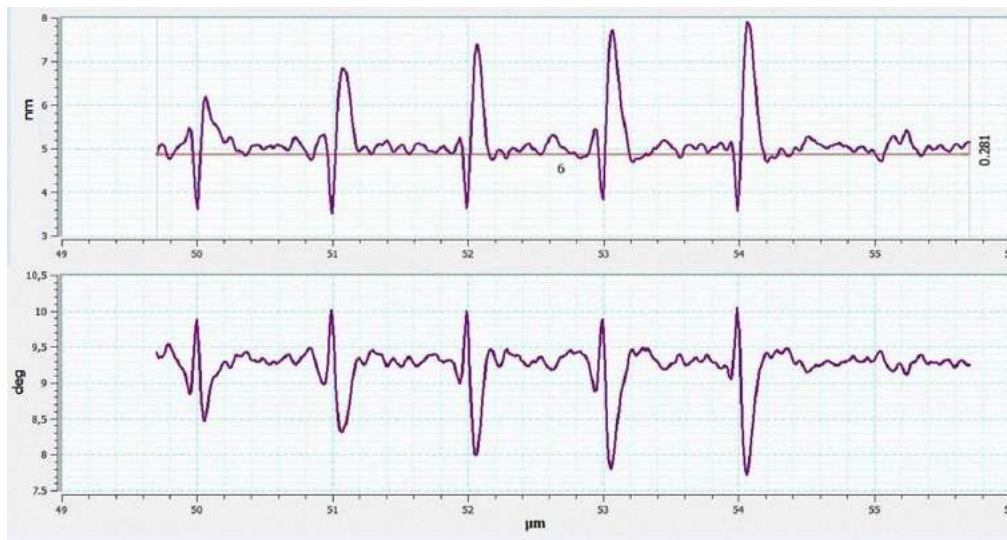


Fig. 2. The topographies of the profiles of SmS sample surface received by the two-pass technique. The profile of topography of the surface with the applied grooves is given in the top chart. In the bottom chart is given the amplitude-phase contrast of the resonant fluctuations of the probe.

### 3. ELECTROSTATIC FORCE AND MAGNETIC FORCE MICROSCOPES

Electrostatic Force Microscopy (EFM) and Magnetic Force Microscopy (MFM) we applied in this work were based on two-pass contactless measurements. Surface topography was taken in the first pass and second pass in which vibrating cantilever remained at constant height while moving above the surface allowed to obtaining a map of electrostatic or magnetic interaction between cantilever tip and surface under consideration.

#### 3.1 ELECTROSTATIC FORCE MICROSCOPY PROFILE

Fig. 3 (top part) displays topographic profile of the grating with grooves separated from one another by 400 nm distance. This grating with low groove frequency was specially prepared for EFM studies to avoid possible electrostatic influence of the grooves on each other. Fig. 4 (bottom part) shows the amplitude-phase contrast for resonance vibrations of the cantilever tip. It is clearly seen that inter-groove regions show no change in signal. Note that any change in signal's amplitude or phase is determined in



this case by the first derivative of the electrostatic interaction between surface and cantilever (8).

The obtained profile of the amplitude phase-contract witnesses that scribing with resultant grating creation leads to the ordered electrostatic field distribution that reflects ordered concentration gradient of the charged particles. This gradient is supposed to emerge due to partial metallization of the

SmS surface after scribing. More exactly, the surface edges of the grooves are metallic while regions between the grooves remain semiconducting. Shown in fig. 5 and supports above assumption regarding partial metallization of SmS. According to our estimations, the concentration of Sm ions that raised their valence to 3+ is approximately  $90 \text{ cm}^{-3}$  per 1 nm groove length.

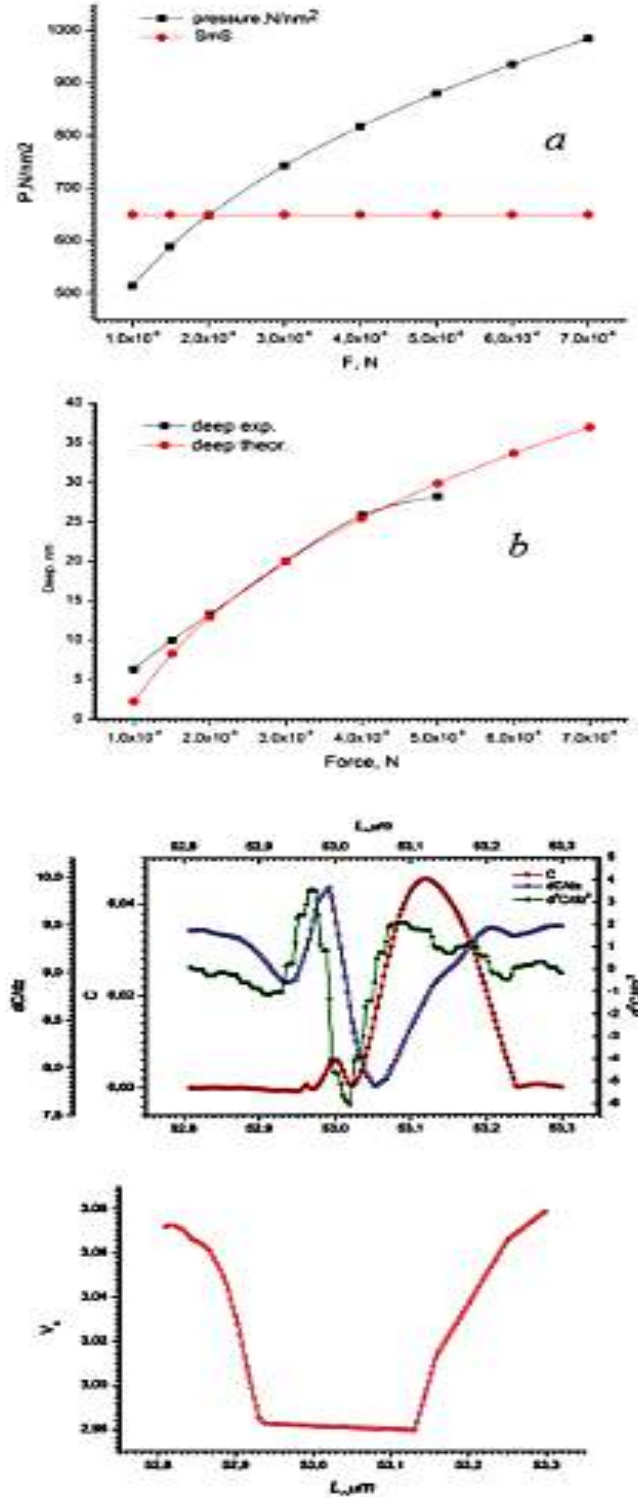


Fig. 3. a - dependence of electrostatic force on "z" distance of the tip provision to SmS film surface; b - determination of the activation energy magnitude at the set mode of dicing; c - three components of force of interaction cantilever- SmS film; d -the established  $E_c$  profile after groove dicing Using calculations data (fig. 2, and 4 a), and also experimental data (fig. 6, b) of activation energy changes for thin polycrystalline SmS films, the optimum mode (fig. 4 is established, b) of grooves dicing of the diffraction lattice (fig. 3) was set.

### 3.2 MAGNETIC FORCE MICROSCOPY PROFILE

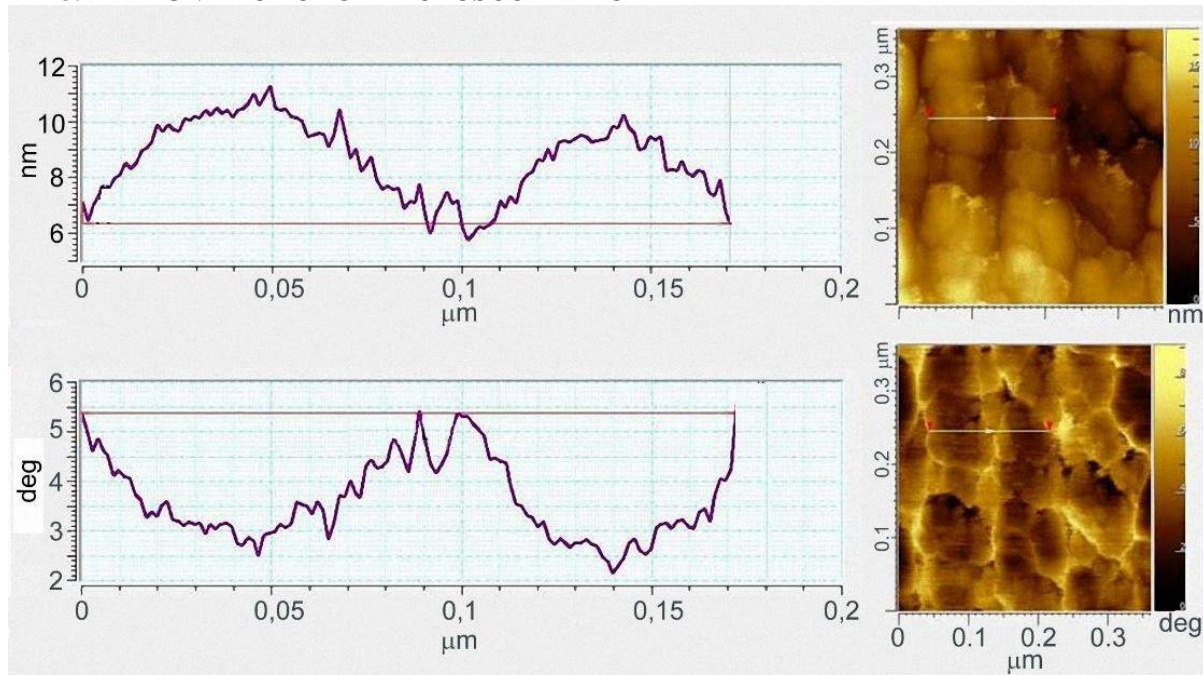


Fig. 4. 2D profiles of the sample surface of samarium sulfide: a – surface topography; b – the MFM profile of the surface.

It is known that magnetic susceptibility of semiconducting SmS is practically independent of temperature [9], which is typical for paramagnetic materials [10]. Magnetic susceptibility of metallic SmS is lower in comparison with semiconducting phase [4], which is caused by transition of Sm<sup>2+</sup> ions into Sm<sup>3+</sup> state [9]. AFM and MFM data for the grating shown in fig. 3 are given in fig. 6. The data were obtained using Pt coated Co-Cr cantilever with resonance frequency 160 kHz. It is well known that any contrast in MFM images reflects change in sample magnetization [11]. Comparison of periodic oscillations in topographic 2D profile (fig. 6, top part) with those in MFM 2D profile (fig. 5, bottom part) just witnesses that groove's edge is interacting with the tip of Co-Cr cantilever weaker than groove's depth. This is completely consistent with the fact that magnetic susceptibility of the metallic SmS is smaller than that of the semiconducting SmS. To overall, MFM data, along with previous EFM data are unambiguous regarding the co-existence of semiconducting and metallic phases in gratings prepared by scribing the surface of SmS thin films.

### 4. CONCLUSION

We have managed to prepare nano-dimensional diffraction grating on the surface of SmS thin film, thus showing that this material can be used for creation of desirable surface architecture by scribing. Besides AFM, we have also performed EFM and MFM characterization of the obtained gratings that have been shown to be two-phase structures with metallic edges separated by semiconducting channels. In fact, the distinct feature of the obtained structure is simultaneous presence of purely geometric modulation and spatial modulation of electric and magnetic properties. This might be useful for development of multifunctional logic elements at the nanoscale.

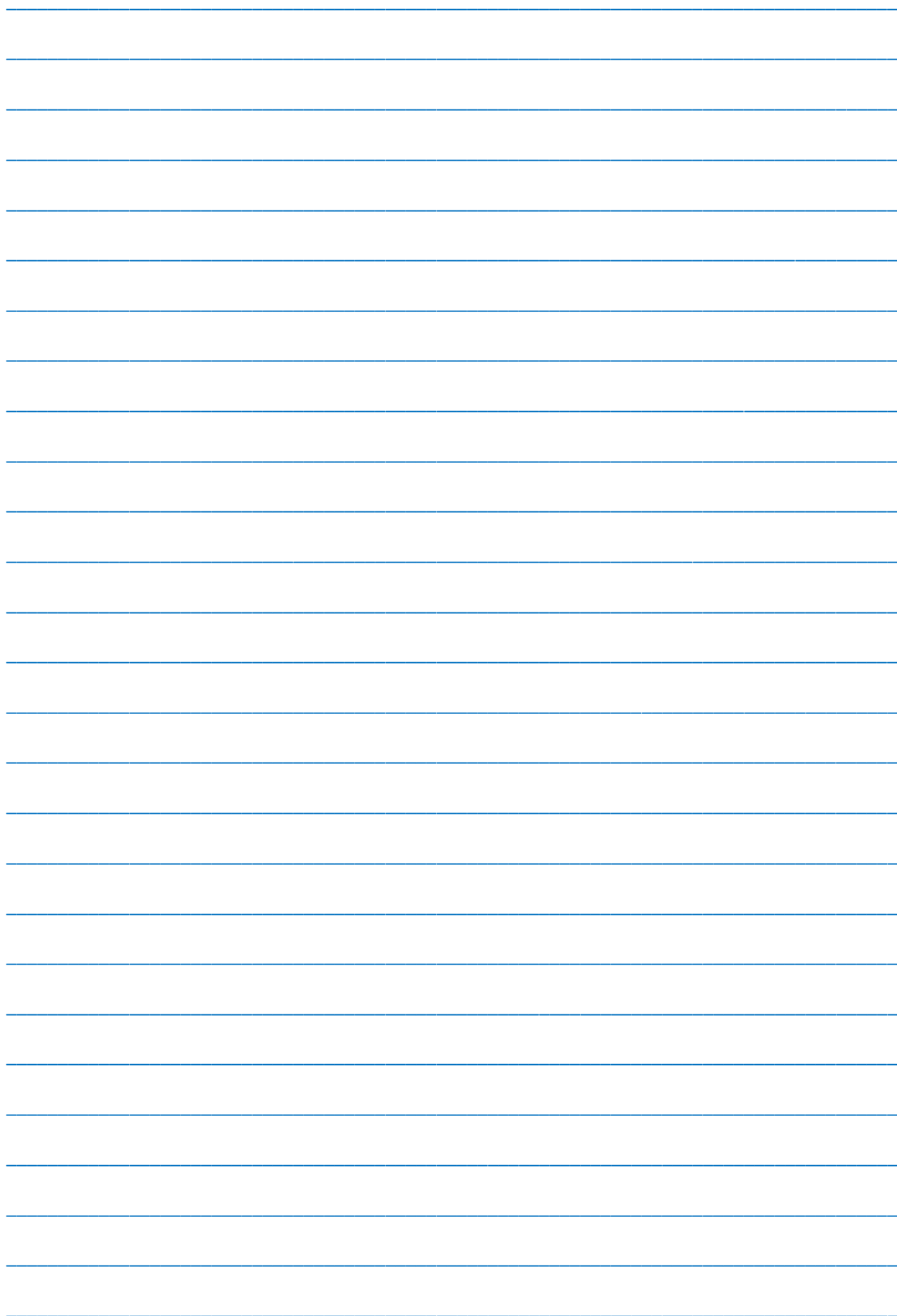
### ACKNOWLEDGEMENTS

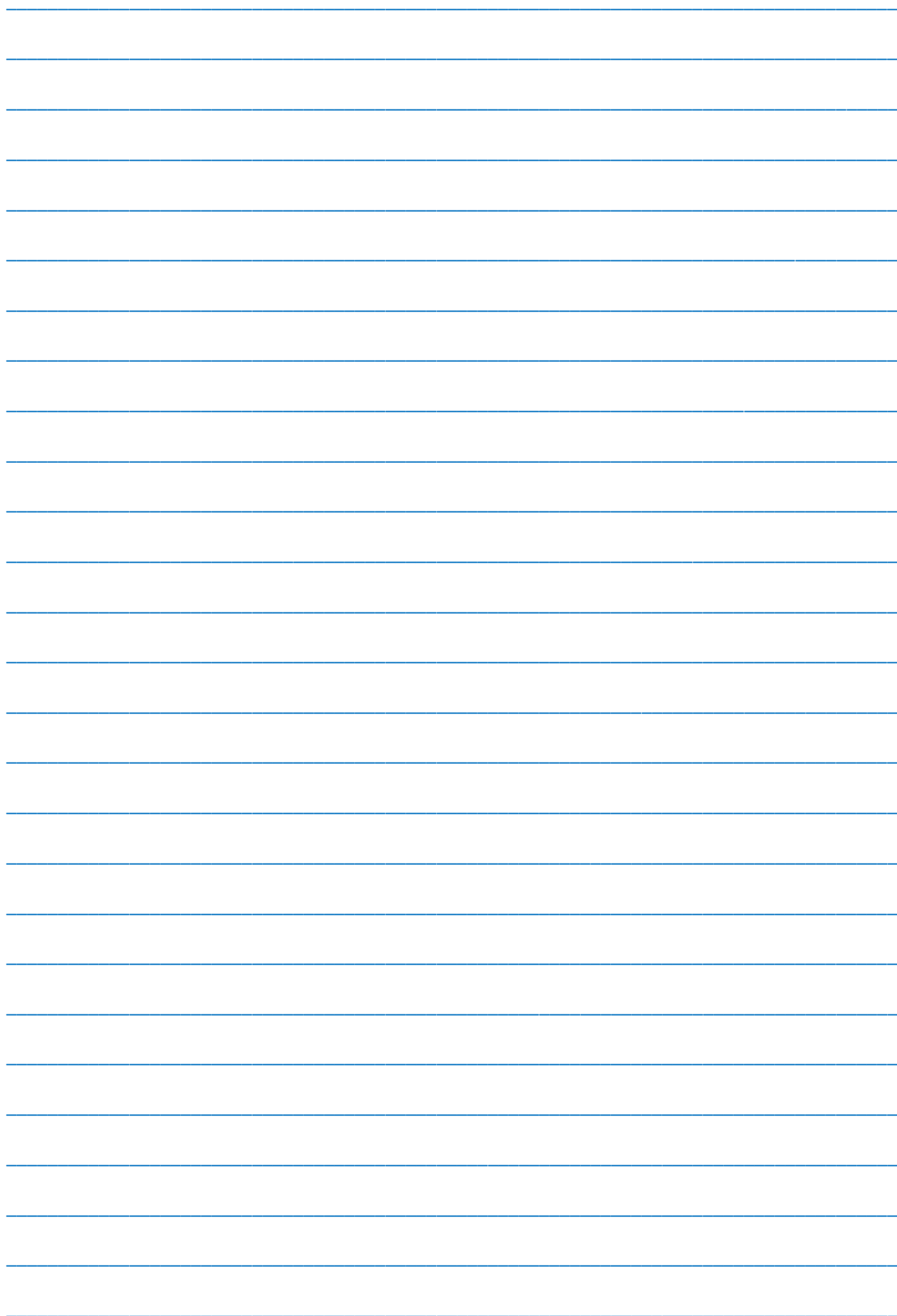
This work was supported by the Science Development Foundation under the President of the Republic of Azerbaijan - grants No. EIF-2013-9(15)-46/05/1.

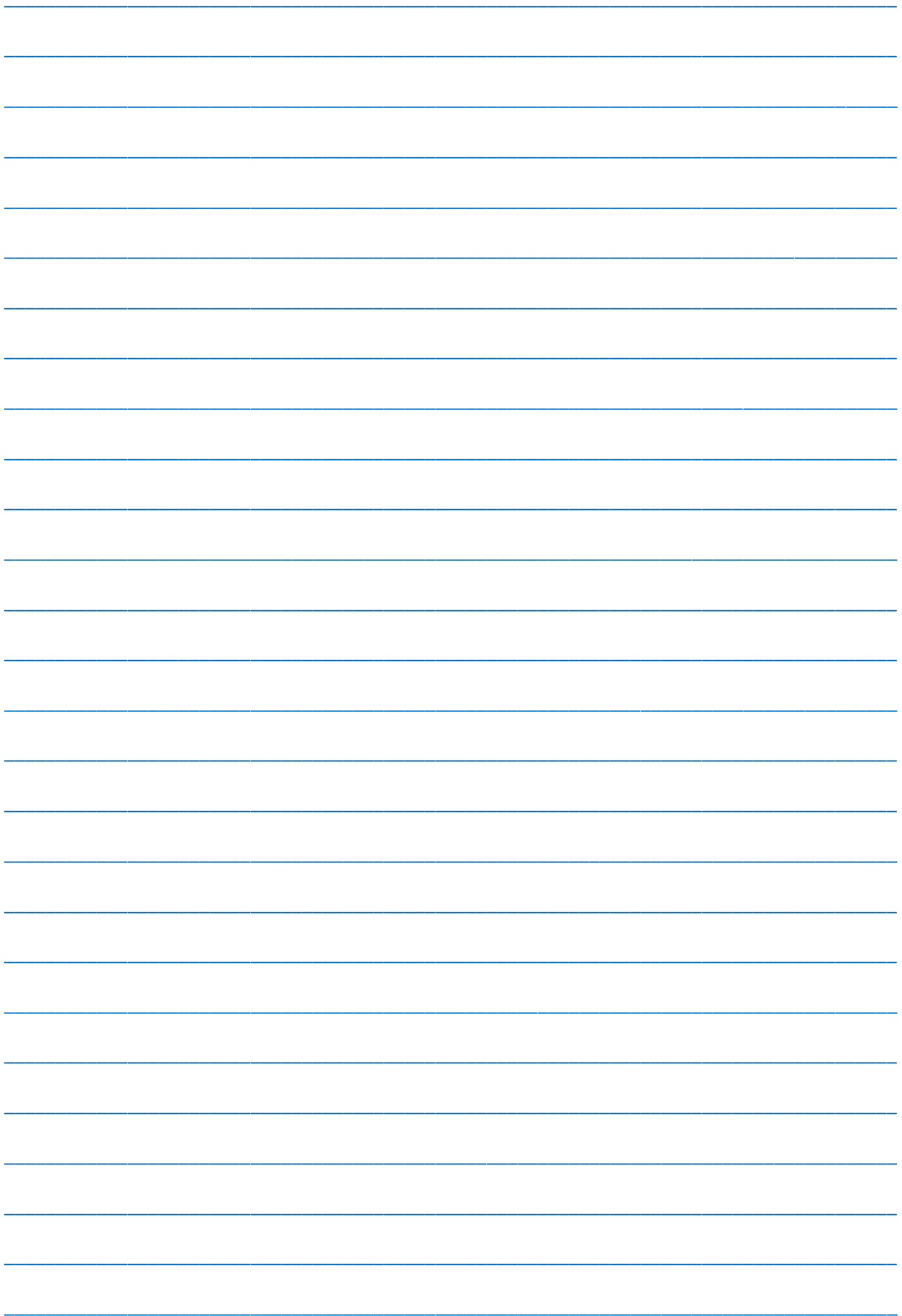
- [1] V.V.Kaminskii, Shinji Hirai, Toshihiro Kuzuya, S.M.Solovyev, N.N.Stepanov, N.V. Sharenkova. Obtaining of SmS based semiconducting material and investigation of its electrical properties, *Physics of the Solid State*, 47, 2013, 1310-1313.
- [2] V.N. Antonov, A.P. Shpak, A.N. Yaresko. Electronic structure of mixed valent systems, *Condensed Matter Physics* 7, 2004, 211–246.
- [3] V.A.Sidorov, N.N.Stepanov, L.G. Khvostantsev, O.B. Tsiok, A. V. Golubkov, V.S. Oskotski and I.A. Smirnov. Intermediate valency state of samarium chalcogenides under high pressure, *Semicond. Sci. Technol.* 4, 1989, 286.
- [4] E.Rogers, P.F. Smet, P. Dorenbos, D. Poelman and E. van der Kolk. The thermally induced metal-semiconducting phase transition of samarium monosulfide (SmS) thin films, *J.Phys. Condens Matter* 22(1), 2010, 015005.
- [5] V.V. Kaminski and M.M. Kazanin. Thermo-voltaic Effect in Thin-Film Samarium- Sulfide-Based Structures, *Technical Physics Letters* 34, 2008, 361–362.
- [6] A. Monniera and M. Schnieper, R. Jaaniso, H.Bill. Samarium-doped thin films of the Matlockite structure: Design, luminescence and

- hole-burning experiments, J. Appl. Phys. 82 (2), 1997, 536-547.
- [7] X.N. Xie, H.J. Chung, C.H. Sow, A.T.S. Wee. Nanoscale materials patterning and engineering by atomic force microscopy nanolithography, Materials Science and Engineering, R 54, 2006, 1–48.
- [8] Jung Yup Yang, Joo Hyung Kim, Jun Seok Lee, Seung Ki Min, Hyun Jung Kim, Kang L. Wang JinPyo Hong. Electrostatic force microscopy measurements of charge trapping behavior of Au nanoparticles embedded in metal– insulator –semiconductor structure, Ultramicroscopy 108, 2008, 1215– 1219.
- [9] P.P. Deen, D. Braithwaite, N. Kernavanois, L. Paolasini, S.Raymond, A.Barla, G. Lapertot, and J. P. Sanchez. Structural and electronic transitions in the low-temperature, high-pressure phase of SmS, Phys. Rev. B, 71 245118, 2005, pp. 55-58.
- [10] Eric Beaurepaire. Magnetism: A Synchrotron Radiation Approach, Springer Science & Business Media, 2006, 468 [11] U. Hartmann, Magnetic force microscopy, Annu. Rev. Mater. Sci. 29, 1999, 53-87.

*Received: 11.09.2019*







## *CONTENTS*

---

1.	Dielectric relaxation in the colloid fullerenes- liquid crystal 5 CB <b>G.F. Ganizade</b>	3
2.	Structural features in systems water- polyethylene glycol -KCl, KBr, KI <b>B.G. Pashayev</b>	7
3.	Investigation of silicon photomultiplier at low temperature <b>F.I. Ahmadov</b>	15
4.	Boundary effects in polymer composites - powered ceramics <b>Z.A. Dadashov</b>	20
5.	Majorana fermions in one- and quasi-one dimensional insulator with charge-density wave <b>S.O. Mammadova</b>	22
6.	Thermodynamic properties of erbium monotelluride <b>I.F. Mekhdiyeva</b>	25
7.	Thermodynamic study of $\text{Cu}_2\text{SnSe}_3$ by EMF method with solid electrolyte $\text{Cu}_4\text{RbCl}_3\text{I}_2$ <b>I.J. Alverdiyev</b>	29
8.	Optical and UV-VIS luminescence spectra of $\text{Ni}_{1-x}\text{Zn}_x\text{Fe}_2\text{O}_4$ ferrite nanopowders <b>A.A. Sadıgova, Sh.N. Aliyeva, Sh.A. Ahmadova, I.F. Yusibova, T.G. Naghiyev, T.R. Mehdiyev</b>	34
9.	Scanning probe microscopy studies of fullerene $\text{C}_{60}$ /porous silicon multilayer structures <b>Yegana Aliyeva</b>	44
10.	SmS thin films with nanosize surface architecture <b>Yegana Aliyeva</b>	47



[www.physics.gov.az](http://www.physics.gov.az)